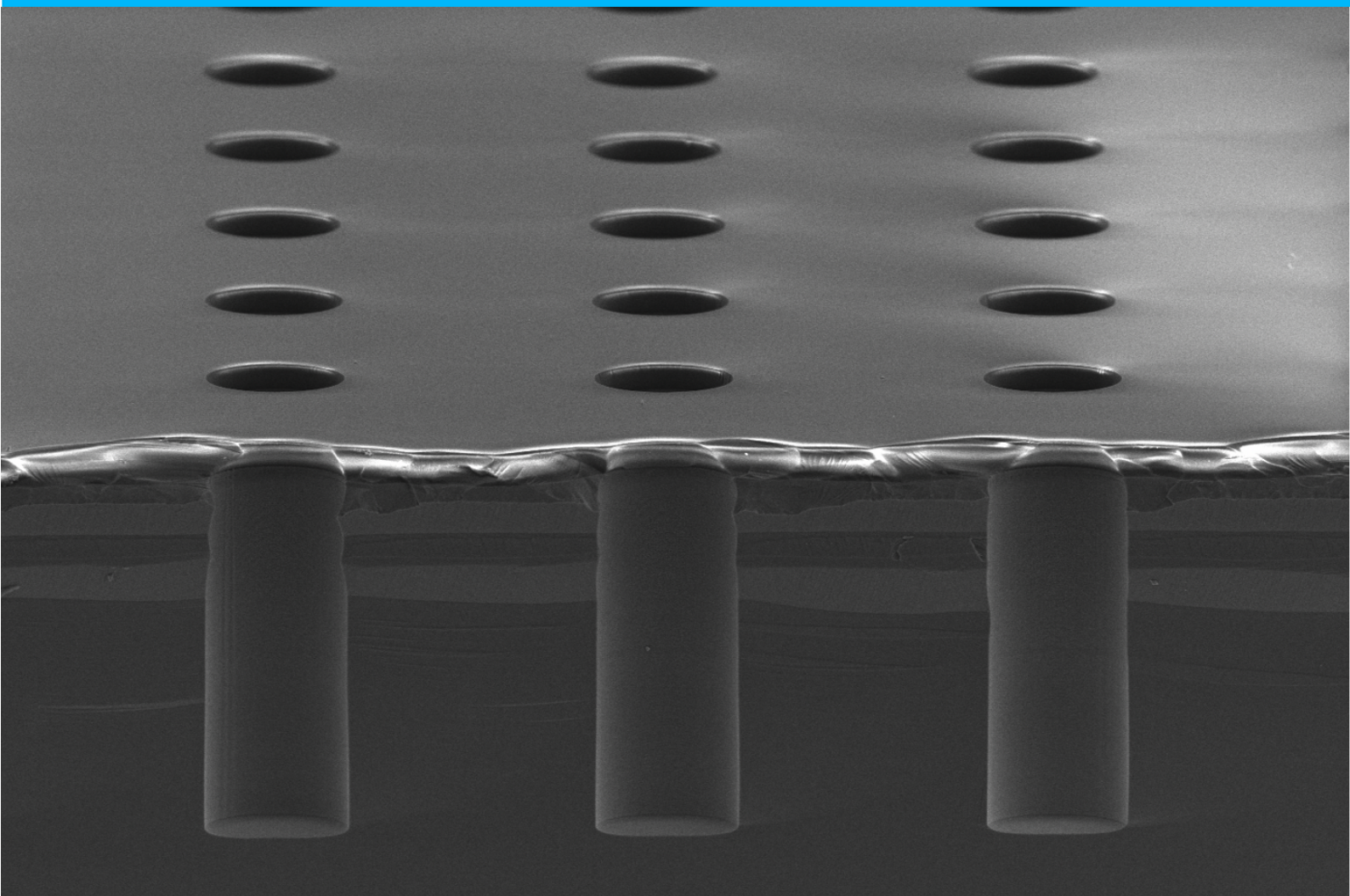


Effect of Pore Size and Distribution on the PEC Properties of Si-Based Porous Monolithic Water-Splitting Devices

M. El Makkaoui

Photovoltaics Materials and Devices Group,
ESE, EEMCS, TU Delft



Effect of Pore Size and Distribution on the PEC Properties of Si-Based Porous Monolithic Water-Splitting Devices

By

Mohammed El Makkaoui

to obtain the degree of Master of Science
at the Delft University of Technology,
to be defended publicly on Thursday August 27, 2020 at 10:00 AM.

Student Number: 4886712
Project Description: December 6th, 2019 – August 27th, 2020
Thesis Committee: Prof. dr. A. H. M. Smets, TU Delft, ESE – PVMD, Supervisor
Dr. Ir. Rudi Santbergen, TU Delft, ESE – PVMD, Assistant Professor
Dr. Ir. Nils van der Blij, TU Delft, ESE – PVMD, Assistant Professor
Ir. Thierry de Vrijer, TU Delft, ESE – PVMD, Daily Supervisor

An electronic version of this thesis is available at <http://repository.tudelft.nl/>.



Preface

My solar energy journey started almost 10 years ago. Right after my BSc in Chemistry I knew for a fact that PV research would be my career path. After having to step away from PV for a few years, I got a looming fear that I would not be able to get back into the field again. The day I decided to take the Solar Energy MicroMasters edX course series, provided by the PVMD group at TU Delft was the day I found myself again. I was extremely impressed with the course and the knowledge it had to offer, so I applied for a MSc degree at TU Delft as soon as I possibly can, for which I was thankfully accepted. It has been such an amazing experience studying and working at TU Delft, I continued to learn so much and got the chance to make many memorable friendships along the way.

First off, I would like to thank my daily supervisor, Thierry de Vrijer, who, even when supervising an army of MSc students, still managed to provide me with all the guidance and assistance I needed during this work. His mentorship was not limited to PV knowledge, his ability to juggle so many things at once and effective prioritization were truly inspiring, I really do feel lucky for having him for my supervisor. I would also like to greatly thank Professor Arno Smets for granting me the opportunity to work with his group. He is, essentially, the main reason I am in TU Delft in the first place. Since taking the online courses, I grew to admire Arno's energy and passion for advancing Photovoltaics and would consider it a privilege to work with him again. Thank you to Martijn Thijssen for all his efforts in keeping our equipment running, as well as the staff members and users of the EKL cleanroom, who were always there to address my question and aiding me in my experiments. I would also like to thank additional members of the PVMD group who helped me throughout my thesis, Gianluca, Can Han, and Yifeng, as well as my fellow MSc students who were my brothers and sisters in arms in our pursuit to get our MSc degrees, especially my office mates, Patrycja, Abdullah, Martijn, Parsa, Lyndon, Saravana, and Shaowei.

I would like to thank my family and friends who have always given me great love and support. Thank you for always being there for me and for your unconditional love. I cannot wait to reunite with so many of you after the Covid-19 situation is more under control.

Lastly, I would like to thank my wife, Amélie. You have been my rock and my pillar. Thank you for putting up with all my late nights of studying. Thank you for being there with me every step of the way. When things got hard, you always knew what to do and what to say. When I felt hopeless, you knew exactly how to lift me up. I love you with all my heart and could never have imagined having such a perfect life partner.

Mohammed El Makkaoui
Delft, August 2020

Abstract

A potential approach to minimizing cabling losses in Photoelectrochemical (PEC) water splitting devices is adapting a wireless stand-alone configuration. With all components integrated into a single device, this configuration also helps in reducing system cost, size, and complexity. The issue with this structure, however, is that the proton transport distance between the electrodes is quite large, as ions need to travel around the cell to reach the opposite electrode. This leads to a pH gradient between the electrodes, resulting in high ohmic losses and risking cross-over between the product gases, which is a safety hazard. This problem can be eliminated by integrating pores into the device that serve as ionic shortcuts between the electrodes, resulting in a Porous Monolithic Photoelectrochemical (PMP) cell.

In this thesis, the effect of pore size and distribution on the performance of PMP cells was analyzed in pursuit of finding a range of optimal pore patterns for this application. A theoretical method involving 2D COMSOL simulations of PMP cells is devised to evaluate losses associated with proton transport (Electrochemical) and the active area available for light absorption (Photovoltaic). It was found that optimal pore size and distribution for proton transport trends towards smaller pore dimensions (diameter and pitch). It was also found that for pore diameters between 20 – 80 μm , the PMP cell can retain up to 70% of the ideal (lossless) photocurrent, if the pH gradient can be suppressed to < 0.36 pH units.

Moreover, two pore-processing techniques were compared, namely Deep Reactive Ion Etching (DRIE) and Pulsed Laser Drilling (PLD), to determine their suitability for this application. DRIE processed holes can be near perfectly cylindrical compared to PLD processed pores, which have rougher sidewalls and exhibit significantly more tapering, in comparison. However, DRIE requires lithographic patterning, which is an expensive process that adds several steps to the fabrication process. For thinner devices $< 100 \mu\text{m}$, mainly thin film technologies, the taper in PLD may be largely suppressed. Resorting to PLD could also reduce investment costs, as it can be implemented through the laser scribing setup, typically used for isolating single cells within a module.

Table of Contents

1. INTRODUCTION	1
1.1. THE ENERGY PROBLEM	1
1.2. SOLAR ENERGY	1
1.3. THE PHOTOVOLTAIC EFFECT	2
1.3.1. <i>Step 1: Generation of Charge Carriers</i>	3
1.3.2. <i>Step 2: Separation of Charge Carriers</i>	5
1.3.3. <i>Step 3: Collection of Charge Carriers</i>	6
1.4. SILICON HETERO-JUNCTION (SHJ)	6
1.5. DRAWBACKS OF C-SI	7
1.6. THIN FILM PV TECHNOLOGIES	7
1.6.1. <i>Cadmium Telluride</i>	8
1.6.2. <i>Copper Indium Gallium Selenide/Sulfide</i>	8
1.6.3. <i>Perovskites</i>	8
1.6.4. <i>Thin Film (TF) Si</i>	8
1.7. MULTI-JUNCTION SOLAR CELLS.....	9
1.8. PHOTOELECTROCHEMICAL (PEC) SOLAR TO FUEL CONVERSION	10
1.8.1. <i>PEC Water-splitting Principles</i>	11
1.8.2. <i>PEC Systems</i>	11
1.8.3. <i>PV-EC Systems</i>	12
1.8.4. <i>Wired vs Wireless</i>	13
1.8.5. <i>Pore Forming Methods</i>	14
1.9. PREVIOUS WORK	15
1.10. THESIS PROJECT GOALS AND OUTLINE	15
2. THEORETICAL BACKGROUND	18
2.1. PV PERFORMANCE	18
2.1.1. <i>Ohm's Law</i>	18
2.1.2. <i>J-V Characteristic of a Solar Cell</i>	18
2.1.3. <i>External Quantum Efficiency (EQE)</i>	21
2.1.4. <i>PV Losses</i>	22
2.2. PEC PERFORMANCE	25
2.2.1. <i>Chemical Definition of STH Efficiency</i>	25
2.2.2. <i>Electrical Definition of STH Efficiency</i>	25
2.3. OVERALL PV-EC PERFORMANCE	30
2.4. OVERALL PERFORMANCE OF PMP CELLS	31
2.4.1. <i>PMP Cell Configuration</i>	31
3. THEORETICAL METHODS.....	38
3.1. MODELLING PH GRADIENTS IN PMP CELLS	38
3.1.1. <i>Geometry</i>	38
3.1.2. <i>Model Setup</i>	39
4. EXPERIMENTAL METHODS	43
4.1. SILICON HETERO-JUNCTION (SHJ) PROCESSING	43
4.1.1. <i>Si Wafer Cleaning and Preparation</i>	43
4.1.2. <i>Plasma Enhanced Chemical Vapor Deposition (PECVD)</i>	43
4.1.3. <i>Transparent Conductive Oxide (TCO) Deposition</i>	44
4.1.4. <i>Si Stacks Used in PMP Cell Experiments</i>	45
4.2. ELECTRODE DEPOSITION	46

4.2.1.	<i>Electron Beam Evaporation</i>	46
4.2.2.	<i>Photolithography</i>	47
4.3.	PORE PROCESSING METHODS	49
4.3.1.	<i>Deep Reactive Ion Etching (DRIE)</i>	49
4.3.2.	<i>Pulsed Laser Drilling (PLD)</i>	51
4.4.	NAFION® PEM IN-FILLING.....	53
4.5.	PV PERFORMANCE CHARACTERIZATION.....	53
4.5.1.	<i>J-V Measurements</i>	53
4.5.2.	<i>External Quantum Efficiency (EQE)</i>	53
4.6.	EC PERFORMANCE CHARACTERIZATION	54
5.	PORE SIZE & DISTRIBUTION OPTIMIZATION	57
5.1.	THEORETICAL RESULTS	57
5.1.1.	<i>Porosity (J_{θ}):</i>	57
5.1.2.	<i>pH Gradient (J_{pH}):</i>	57
5.1.3.	<i>Porosity + pH Gradient ($J_{overall}$):</i>	58
5.1.4.	<i>Defining the Optimum Pore Size and Distribution</i>	59
5.1.5.	<i>Generalizing the Influence of Pore Size & Distribution</i>	60
6.	EXPERIMENTAL RESULTS.....	63
6.1.	ANODE MICRODOT CHALLENGES.....	63
6.2.	DEEP REACTIVE ION ETCHING	64
6.3.	PULSED LASER DRILLING	67
7.	CONCLUSION AND RECOMMENDATIONS.....	73
7.1.	CONCLUSION	73
7.2.	RECOMMENDATIONS	73
8.	BIBLIOGRAPHY.....	76
	APPENDIX A: PROCESSING PARAMETERS	84
	APPENDIX B: PH GRADIENT SIMULATIONS (WITH VS WITHOUT PEM)	85
	APPENDIX C: J-V AND EQE PLOTS OF SILICON HETERO-JUNCTIONS.....	86

List of Figures

Figure 1.1: Solar spectrum of (a) blackbody with a surface temperature of 6000 K; (b) AM0 solar spectrum; and (c) AM1.5 solar spectrum [18].	2
Figure 1.2: Conventional crystalline Silicon solar cell configuration [18].	3
Figure 1.3: Silicon Bohr model (atomic structure) [22]. Silicon has the electron configuration of Neon (Ne) in addition to four valence electrons.	3
Figure 1.4: Energy levels and bands of a Silicon atom splitting into energy bands as more Silicon atoms bond to form a bulk [23].	4
Figure 1.5: Energy band diagrams from left to right: Metal; Insulator; and Semiconductor [24].	4
Figure 1.6: Fermi level position for: (a) intrinsic; (b) n-type; and (c) p-type semiconductors [18].	5
Figure 1.7: The energy band diagram of a PN-junction [25].	6
Figure 2.1: J-V Characteristic of a solar cell in the dark and under illumination [18].	20
Figure 2.2: Current voltage plot of a solar cell showing the influence of R_s and R_p [84].	21
Figure 2.3: EQE plot for a high performing c-Si based solar cell [18].	22
Figure 2.4: Tapering illustrated in 2D.	24
Figure 2.5: Examples of pores with modulated diameters [86].	24
Figure 2.6: Thermodynamics plot of the Gibbs free energy versus time. A positive ΔG indicates a barrier for the reaction to proceed, whereas a negative ΔG represents a spontaneous reaction [87].	25
Figure 2.7: Plot of the water splitting electrode potentials versus the pH [91].	26
Figure 2.8: J- η characteristic of a PEC cell, demonstrating the influence of the exchange current density and overpotential on PEC performance [92].	29
Figure 2.9: Overlap of PV and PEC current voltage characteristics for determining the operational point of the PV-PEC system [9].	31
Figure 2.10: 2D COMSOL model of (A) a dense PV-EC cell and (B) a porous PV-EC cell [70].	32
Figure 2.11: Hydrogen cross-over for PMP cell with and without Nafion® [70].	32
Figure 2.12: J-V characteristic for PMP cell: bare; with pores; with pores and anode microdot coverage of 2.5%, 5%, and 10%, respectively [70].	34
Figure 2.13: Effect of pore geometry on the current voltage characteristic of PMP cells [68].	34
Figure 2.14: A PMP unit cell consisting of four pores. The red dot is farthest H^+ generation point to the nearest hole.	35
Figure 3.1: Geometry for $D_p/P_p = 40\mu m/150\mu m$ (a) full view; (b) close up.	38
Figure 3.2: pH gradient simulation for $D_p/P_p = 50\mu m/200\mu m$ (a) full view; (b) close up. The blue and red dots correspond to the anode and cathode pH values, respectively.	41
Figure 4.1: Plasma Enhance Chemical Vapor Deposition (PECVD) setup illustration [18].	44
Figure 4.2: RF Magnetron Sputtering process [97].	45
Figure 4.3: Electron Beam Evaporator illustration [98].	46

Figure 4.4: Photolithography process: (a) → (b) Coating; (b) → (d) Exposure; (d) → (e) Development [99].	47
Figure 4.5: Photomask pattern designs: (Left) Anode microdot mask; (Right) Cathode hole mask.	48
Figure 4.6: Photoresist patterning of 20 μ m holes with a pitch of 80 μ m on the cathode side.	49
Figure 4.7: 60 μ m holes after Pt deposition: (Left) Before lift-off; (Right) After lift-off.	49
Figure 4.8: Illustration of the (a) Bosch "Pulsed" DRIE process [100]; (b) Cryogenic DRIE process [101].	50
Figure 4.9: Pulsed laser drilling setup [102].	52
Figure 4.10: SEM's of PLD processed pores before and after treatment with 15:9:2 40%HF:69.5%HNO ₃ :H ₂ O etchant solution [103].	53
Figure 4.11: J-E measurement setup for a PMP cell in the photocathode configuration. The cathode is exposed to the electrolyte, while the anode is at the illuminated side outside the solution and connected as the working electrode. A counter electrode and reference electrode are included to complete the 3-electrode configuration [70].	54
Figure 5.1: Contour plot of the normalized current density: (a) $J_{\theta, norm}$ when only porosity is accounted for; (b) $J_{pH, norm}$ when only pH gradient losses are considered.	58
Figure 5.2: Contour plot of the normalized current density $J_{overall, norm}$ when both porosity and pH gradient losses are considered.	59
Figure 5.3: Plot of the normalized overall current density as a function of pore diameter, considering optimal pore spacing.	59
Figure 5.4: Plot of the normalized overall current density as a function of pore diameter, considering optimal pore spacing, for different pH gradient values: (1) $\frac{1}{2}\Delta pH_{sim}$; (2) ΔpH_{sim} ; (3) $2\Delta pH_{sim}$; (4) $3\Delta pH_{sim}$; (5) $4\Delta pH_{sim}$.	60
Figure 6.1: 60 μ m pores etched 150.9 μ m deep via DRIE following the recipe from [90].	65
Figure 6.2: Complete penetration achieved for: (a) All pore diameters, except 20 μ m, after 4 hours and 15 minutes; (b) All pore diameters (20 μ m – 80 μ m) after 6 hours 30 minutes of DRIE.	65
Figure 6.3: 20 μ m diameter pores with an etch depth of 235.1 μ m after 4 hours and 15 minutes of DRIE using the recipe from [90].	66
Figure 6.4: 20 μ m diameter pores: (a) Anode side; (b) Cathode side.	66
Figure 6.5: 60 μ m diameter pores: (a) Anode side; (b) Cathode side.	67
Figure 6.6: (from left to right) Pores drilled at $E_{Pulse} = 20\%$, 5% , and 1% , respectively.	68
Figure 6.7: SEM images of: (a) Pt entrance hole; (b) ITO entrance hole; (c) ITO exit hole; (d) Pt exit hole.	68
Figure 6.8: (a) Illustration of the triangular pore matrix for the parameter optimization experiments; (b) Photograph of the substrate holder used to stabilize the wafer.	69
Figure 6.9: Wafer surface before and after removal of the protective photoresist layer.	69
Figure 6.10: Reproducible PLD processed pores at $E_{Pulse} = 0.58 - 0.6\%$ and $N_{Pulse} = 80 - 90$. (a) and (c) show the cathode side (entrance holes), while (b) and (d) show the anode side (exit holes).	70
Figure 6.11: Cross-section of PLD processed pore, indicating clear sidewall roughness.	70

Table 3-1: Electrolyte parameters for 0.1 M H ₂ SO ₄ solution at T = 25 °C.....	39
Table 3-2: Electrode kinetics input parameters.....	40

1. Introduction

1.1. The Energy Problem

The annual global energy consumption reached 22,315 TWh in 2018 [1] & [2] which, with the ever-increasing global population, is projected to rise by 50 % between now and the year 2050 [1] & [2]. This demand is predominantly supplied by fossil fuels, which comprise around 80 % of the global energy market [1] & [2]. Fossil fuels are detrimental to our environment, the burning of which has so far led to over 35 Gigatons of carbon dioxide (CO₂) emissions, globally, and is projected to continue to rise at our current rate of consumption [3].

It is thus imperative to invest in renewable energy sources, such as solar, wind and geothermal energy, to name a few, as a range of viable, environmentally friendly alternatives to fossil fuels [1] – [6]. Solar energy is particularly promising, owing to the massive and practically infinite solar irradiation available to our planet. The annual solar energy potential is around 23,000 TW, which is almost 1000 times larger than the annual global consumption [7]. It is worth noting that the reserves for all other renewable energy sources, combined, amounts to around 7.6% of the potential solar energy [7]. The overall global installed PV capacity has grown significantly from 40 GW in 2010 to 629 GW by the end of 2019 and is projected to continue to rise [8]. However, solar cells are, as are other renewable energy sources, majorly hindered by their intermittency, as PV power is only generated when the Sun is out [1] – [6]. Thus, for grids of the future to realize their renewable potential, they require the integration of energy storage technologies [9] – [12]. An alternative form of solar energy utilization presents a solution to this issue, namely, Photoelectrochemical (PEC) water-splitting, wherein solar radiation drives the electrolysis of water into oxygen (O₂) and hydrogen (H₂), the latter of which is a promising green fuel [9], [11] & [13] – [15]. H₂ fuel is used in renewable energy storage technologies, namely with Hydrogen Fuel Cells (HFC) [16] & [17]. HFC's work inversely to PEC devices, where hydrogen combines with oxygen to supply energy, with the only by-products being water and heat [16].

1.2. Solar Energy

Radiation from the Sun comes in the form of Electromagnetic (EM) waves that consist of discrete or quantized packets of energy known as photons. This particle/wave duality that light exhibits allows for relating the energy a photon carries E_{ph} to the EM wave frequency ν or wavelength λ :

$$E_{ph} = h\nu = \frac{hc}{\lambda} \quad (1.1)$$

Where $h = 6.626 \times 10^{-34}$ J.s is Planck's constant, while $c = 2.998 \times 10^8$ m/s is the speed of light in vacuum [18].

The Sun can be described as a blackbody, having a surface temperature of around 6000 K that emits a wide range of photon energies, otherwise known as a solar spectrum. A blackbody with a surface temperature of 6000 K is shown (black line) in Figure 1.1 [18]. As the radiation travels through space, some photons get attenuated, as the light grows more disperse, and get scattered with particles in their trajectory. The AMO spectrum in Figure 1.1 (blue line) corresponds to the extra-terrestrial

spectrum just outside the Earth's atmosphere [18]. The total irradiance in the AM0 spectrum amounts to 1361 W/m^2 . As light travels through the atmosphere it gets scattered and absorbed by particles and molecules like water and carbon dioxide before reaching the surface. AM stands for air mass, which is the ratio of the optical path light needs to travel through the atmosphere to the shortest path, defined by the zenith angle, when the Sun is exactly overhead. The expression for AM is [18]:

$$AM = \frac{1}{\cos\theta} \quad (1.2)$$

Where θ is the angle between the position of the Sun and zenith [18].

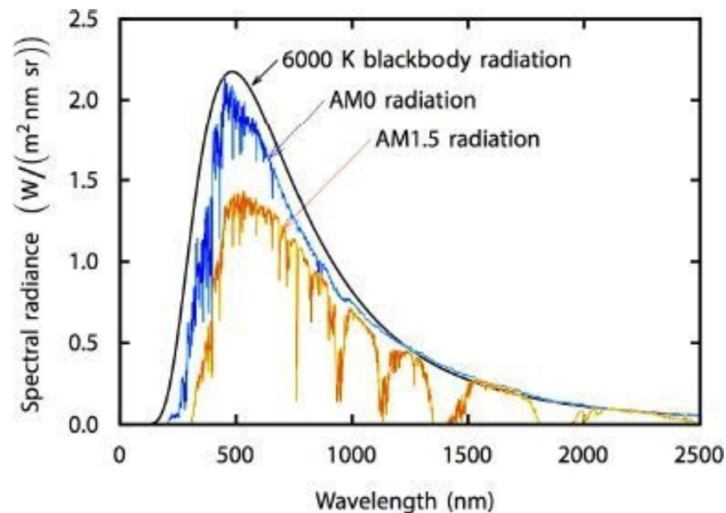


Figure 1.1: Solar spectrum of (a) blackbody with a surface temperature of 6000 K; (b) AM0 solar spectrum; and (c) AM1.5 solar spectrum [18].

According to the IEC international standard 60904-3, PV and PEC performances are tested using the AM1.5 solar spectrum shown in Figure 1.1 (yellow line), which corresponds to a surface tilt angle of 37° or an angle of incidence of 48.2° [18] – [20], as well as a spectral irradiance of 1000 W/m^2 and temperature of 25°C . The dips in spectral irradiance correspond to light absorption from molecules in the atmosphere.

1.3. The Photovoltaic Effect

Since the devices in this study are based on Silicon (Si) PV, which also happens to be a mature technology from which a large portion of PV knowledge is derived, the conventional crystalline Si (c-Si) PV configuration, highlighted in Figure 1.2 [18], will be considered in this section.

The photovoltaic effect is the process of converting solar energy into electrical energy and can be sequenced into 3 steps:

1. Generation of charge carriers (electrons and holes) upon light absorption
2. Separation of charge carriers at the PN junction
3. Collection of charge carriers at their respective terminals

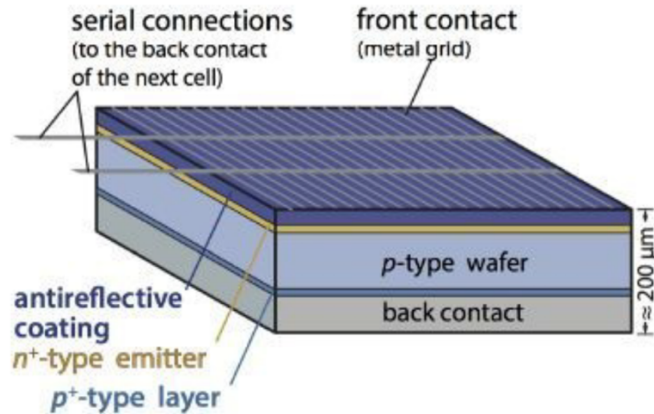


Figure 1.2: Conventional crystalline Silicon solar cell configuration [18].

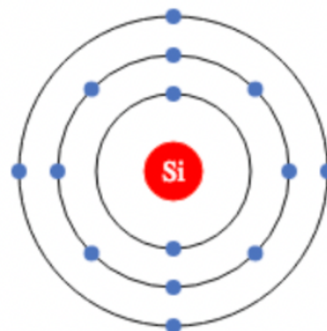
1.3.1. Step 1: Generation of Charge Carriers

Arguably the most important component in PV or PEC devices is the light absorber. It is thus crucial to understand how this component operates and what type of materials it can be fabricated from. The first step in converting solar energy into electricity involves the absorption of a photon with sufficient energy, which results in the excitation of an electron in the Valence Band (VB), into the Conduction Band (CB), leaving behind a positively charged hole. These energy bands are characteristic of the bonding between atomic or molecular orbitals of the elements or molecules comprising the material.

From Energy Levels to Energy Bands

Consider the atomic structure of Si. It has 14 electrons, each occupying a unique energy state, as per the Pauli Exclusion Principle. The Si Bohr model, shown in Figure 1.3 [22] indicates that Si has 4 electrons in its valence or outermost shell, which requires 4 more electrons to complete the octet. The valence shell consists of one 3s and three 3p orbitals. These atomic orbitals hybridize to form a set of four equivalent sp³ orbitals, through which four bonds can be made to neighbouring atoms.

14: Silicon



[Ne] 3s² 3p²

Figure 1.3: Silicon Bohr model (atomic structure) [22]. Silicon has the electron configuration of Neon (Ne) in addition to four valence electrons.

As more Si atoms bond together, each energy level splits into multiple discrete energy states. As more Si atoms are added to form a bulk, the energy levels continue to split, resulting in a continuous band. The VB extends to the Valence Band Edge (VBE), where the highest occupied molecular orbital HOMO resides (bonding), while the CB begins at the Conduction Band Edge

(CBE), the location of the lowest unoccupied molecular orbital LUMO (anti-bonding), as illustrated in Figure 1.4 [23].

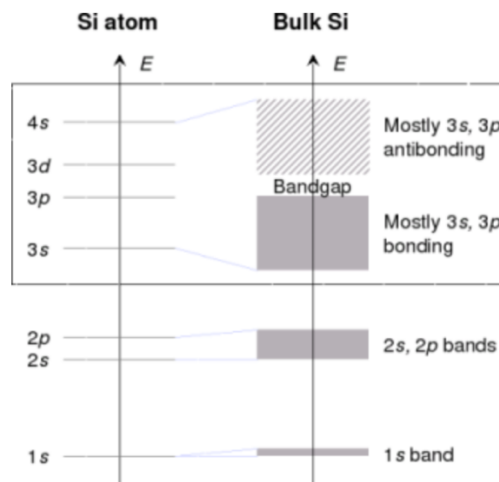


Figure 1.4: Energy levels and bands of a Silicon atom splitting into energy bands as more Silicon atoms bond to form a bulk [23].

The Band Gap

The space between the bands is known as the band gap, which represents the forbidden energy states [11] – [13]. The band gap energy E_G is defined as the difference between the CBE and VBE energy levels, E_c and E_v , respectively. E_{ph} must be $\geq E_G$ in order to generate an electron-hole pair.

Semiconductor vs Insulator vs Conductor

The photo-absorber is typically chosen to be a semiconductor. The band diagrams shown in Figure 1.5 provide reasoning for this choice [24]. Insulators have relatively large band gaps, which makes it improbable to excite charge carrier upon solar illumination. Metals do not possess a band gap, as the bands overlap, and the CB is partially filled. Therefore, minimal energy is needed to generate and conduct charge carriers. Semiconductors have a band gap, but it is smaller than that of insulators, such that absorption takes place mainly in the Ultraviolet-Visible-Near Infrared (UV-VIS-NIR) range [18] – [20], which matches well with the Sun’s solar spectrum.

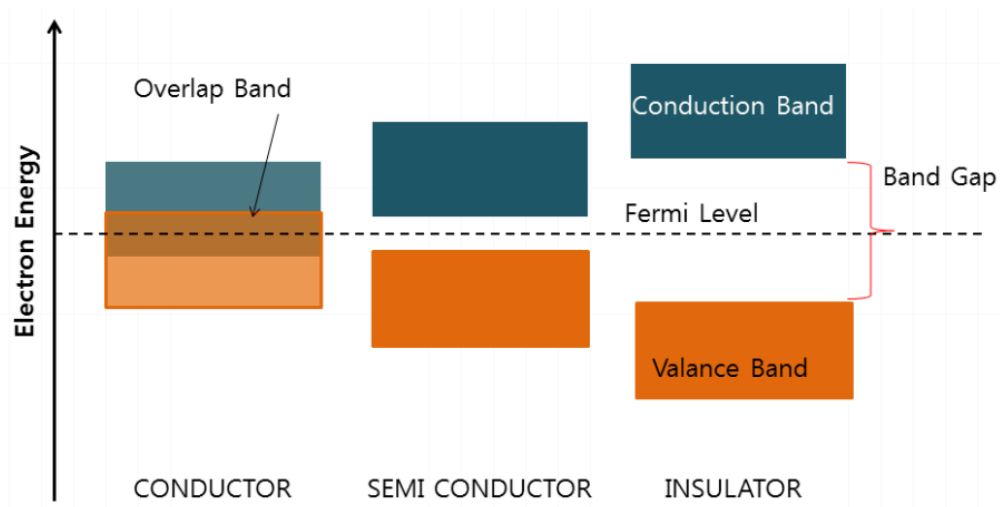


Figure 1.5: Energy band diagrams from left to right: Metal; Insulator; and Semiconductor [24].

1.3.2. Step 2: Separation of Charge Carriers

Once the electron-hole pair is generated, the charge carriers become mobile as they are less bounded to their atoms; however, they are also prone to recombining with each other and falling back to the ground state. With an isolated intrinsic absorber, recombination will dominate, as there is no electric field or concentration gradient present to drive the electrons and holes away from each other.

Doping

The average energy in a material depends on the concentration of free electrons “ n ” and holes “ p ” and is referred to as the Fermi energy level E_F [18] – [20]. For an intrinsic material, the Fermi level is close to the middle of the band gap, as $n \approx p$. A material is considered n-type when $n > p$, pushing E_F closer to the CBE, whereas for a p-type material, $p > n$ and E_F draws closer to the VBE, as shown in Figure 1.6. Pure Si is naturally intrinsic but can be made p- or n-type by the process of doping, wherein small amounts of elemental impurities are added to adjust the position of the Fermi level [18]. Group 5 elements, such as Boron (B), have 3 electrons in their valence shell, which is one less than Si. The p-type (acceptor) dopant introduces an energy level E_A close to the VBE. Their inclusion into the Si lattice results in an excess of holes (p-type), while including Group 7 elements, like Phosphorous (P) leads to an excess of electrons (n-type), since they possess 5 electrons in their valence shell. E_D is the n-type (donor) energy level introduced due to Phosphorous doping [18].

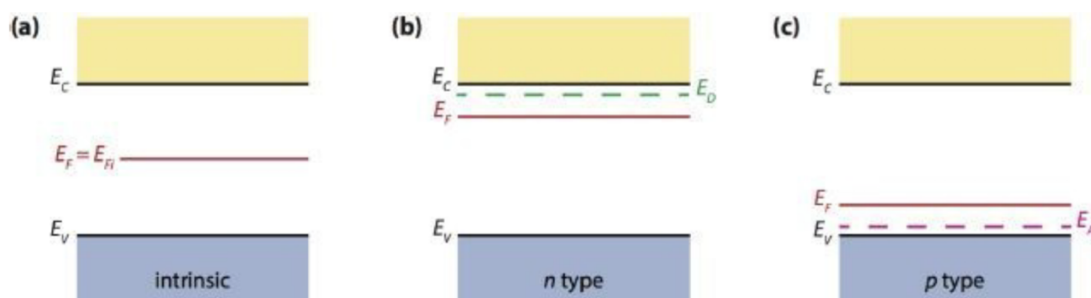


Figure 1.6: Fermi level position for: (a) intrinsic; (b) n-type; and (c) p-type semiconductors [18].

The PN-Junction

An electric field is generated by bringing in contact an n-type and a p-type material, as shown in Figure 1.7 [25]. The average energy is the same throughout the device, so the Fermi levels align, resulting in band-bending in what is called the Space Charge Region (SCR) or depletion width, the centre of which is the PN-junction. Charge carriers generated in the SCR are directly swept out by the built-in potential, leaving the dopant atoms in the SCR ionized. This built-in potential of the ionized dopants forms a barrier to diffusion currents driven by concentration gradients across the junction (electrons from right to left / holes from left to right), while favouring drift currents that are driven by the electric field generated in the SCR (electrons from left to right / holes from right to left).

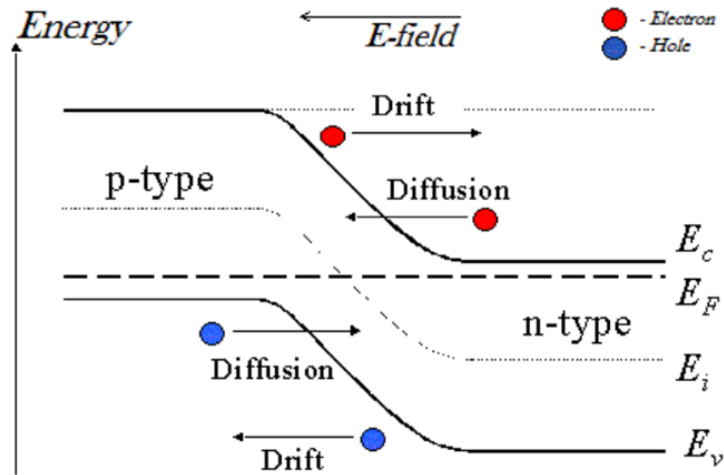


Figure 1.7: The energy band diagram of a PN-junction [25].

1.3.3. Step 3: Collection of Charge Carriers

Figure 1.2 shows an example of a c-Si solar cell that has a p-type absorber. The n-type layer, with which it forms the junction, is referred to as the emitter layer [18]. Each of these layers is contacted with conductors, which serve as terminals for connecting the solar cell to a circuit. The electrons flow into the circuit through the contact at the n-side and recombine with the holes at the p-side contact.

1.4. Silicon Hetero-Junction (SHJ)

Though c-Si is a mature PV technology, it is a weak absorber owing to its indirect band gap. The energy dispersion diagrams in Figure 1.8 illustrate the difference between a direct and indirect band gap material, which is defined by the position of the valence and conduction band edges in momentum k space [18].

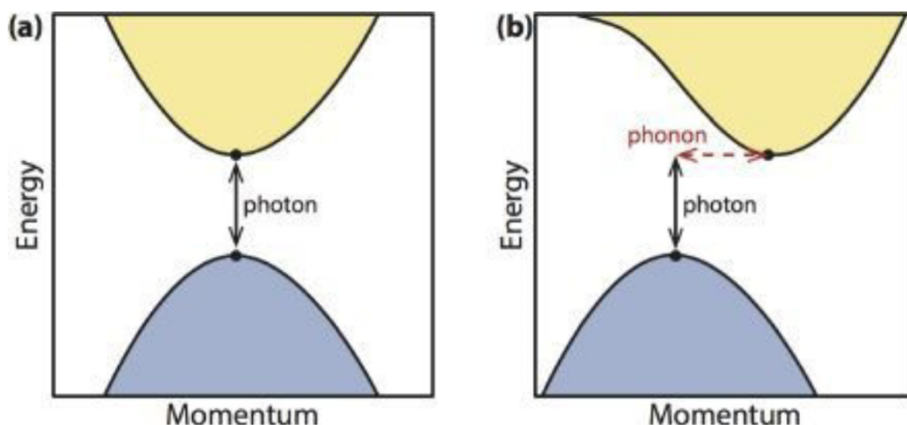


Figure 1.8: Energy Dispersion diagrams for: (a) Direct band gap semiconductor; (b) Indirect band gap semiconductor [18].

For an electron to reach the conduction band edge, it requires enough energy to, first, overcome the band gap, and then to reach the momentum of the conduction band edge, which is achieved through phononic vibrations [20]. Silicon requires relatively thick absorber layers for sufficient light absorption [18] – [20]. The absorber thickness is currently limited to 180 μm , with research proceeding towards 100 μm , whereas thin film-based technologies require far less in comparison < 5 μm [26]. Another issue for large thickness is that charge carriers generated in the quasi-neutral region, farther away

from the junction, are more likely to recombine before reaching the SCR, which limits the built-in potential of the cell.

An alternative configuration to the conventional c-Si solar cell is the Silicon Hetero-Junction (SHJ), which operates based on drift rather than diffusion, wherein charge carriers are generated inside an electric field and are more efficiently collected. The absorber is moderately doped and thick enough to absorb sufficiently. Figure 1.9 shows a typical SHJ configuration with an n-type absorber [27]. The wafer is first passivated on both sides with an intrinsic amorphous Si thin film then sandwiched between two very thin, conductive, and heavily doped p and n-type layers, based on amorphous or nanocrystalline Si. The doped layers serve as selective contacts for enhancing minority charge carrier collection [27]. Additionally, a transparent conductive oxide (TCO) is included between the semiconductor and the metal to enhance lateral conduction at the surface and reduce ohmic losses. Si PV technologies have achieved their highest record efficiency of 26.7% based on this SHJ configuration, which also happens to be higher than that of other PV technologies that are being researched as viable cost-effective alternatives [27].

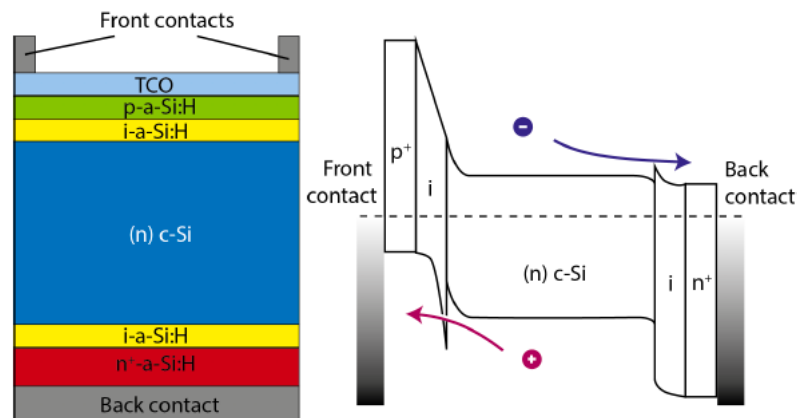


Figure 1.9: Solar cell configuration and band diagram of a Si heterojunction (SHJ) based on n-type c-Si absorber [12].

1.5. Drawbacks of c-Si

Crystalline Si has come a long way in terms of efficiency, optimization, and reliability, with module prices having dropped dramatically since 1954 [18] – [20], when the first successful PV device was produced. Back then, the efficiency was 6%, whereas now, panel efficiencies in the market range from 15 – 22% [28]. Having reached module efficiencies > 20 % and cost per Watt-peak (W_p) > 0.2 Eurocents/ W_p , c-Si solar cells have been and remain dominant in the PV market, holding around 90 % of the share [13]. However, single junction c-Si PV is approaching its efficiency plateau, while PV still lags behind in the energy market [29]. Moreover, as earlier discussed, c-Si is a weak absorber and requires high crystalline purity and large thicknesses, relative to other PV technologies, for sufficient absorption, which limits further significant reductions in production costs.

1.6. Thin Film PV Technologies

Thin film (TF) solar cells present the advantage of reduced material requirement and cheaper, more efficient processing (solution and vapor based methods) [26] & [30] – [33]. The absorbers possess superior opto-electronic properties, generally having high absorption coefficients and direct band gaps, which reduces the required thickness needed for sufficient absorption to < 5 μ m [26]. The versatility of thin film processing allows for depositing devices on a multitude of substrates, such as glass, Aluminium (Al) or thin crystalline Si foil, or even c-Si wafers [30] – [35]. Moreover, thin film

modules can be made lightweight and/or flexible and have an aesthetic appeal, which widens their applicability in building integrated PV (BIPV) and floating PV farms [36] & [37]. There are several thin film solar cell technologies being investigated, but perhaps the most notable are Chalcogenide based thin films like Cadmium Telluride (CdTe) and Copper Indium Gallium Selenide/Sulfide (CIGS), organic based solar cells, such as perovskites, as well as thin film amorphous or nanocrystalline Silicon.

1.6.1. Cadmium Telluride

CdTe is a II-VI semiconductor with a close to optimal band gap of 1.45 eV and has already reached a record cell efficiency of 22.1% [39], currently holding the second highest share in the market after c-Si [29]. The main drawback of CdTe is the toxicity and relative rarity of its constituent elements, Cadmium (Cd) and Tellurium (Te), which limits the potential for further up-scaling this technology and poses environmental concerns.

1.6.2. Copper Indium Gallium Selenide/Sulfide

CIGS is a chalcopyrite compound semiconductor that has also made its way to the market and has attained a high record cell efficiency of 23.35% [40]. The band gap of CIGS can be modified by adjusting the Indium/Gallium ratio (Band gap for CIS = 1.04 eV; for CGS = 1.68 eV) and the Sulphur/Selenide ratio, widening the band gap with larger Sulphur content, which allows for processing multi-junction CIGS based solar cells [42]. The Indium in CIGS is a rare element that is already used heavily in industry as transparent conductive oxides (TCO). Moreover, CIGS PV processing is still practically expensive, making them less competitive than c-Si and CdTe [29].

1.6.3. Perovskites

Perovskites are a promising and fairly young technology that has made great progress in a short span of time, already achieving a record lab-scale initial single junction cell efficiency of 25.2% since major research efforts began in 2009 [42]. The opto-electronic properties of this material are outstanding, achieving open circuit voltages as high as 1.5 V, diffusion lengths on the order of microns, while only requiring about 300 nm of absorber thickness [43] Furthermore, the band gap can be tuned by adjusting the absorber composition [44] – [46]. Unfortunately, the stability of perovskite solar cells remains very poor compared to other technologies. This makes commercial viability a challenge [47] – [48]. Additionally, the leading perovskite solar cell technology is based on Lead (Pb), though there has been progress with non-toxic alternatives, based on Tin (Sn) and other cations [49].

1.6.4. Thin Film (TF) Si

As was alluded to earlier, Si can also be processed into thin film Si solar cells; however, the resulting material exhibits markedly different opto-electronic properties compared to its single crystalline counterpart. Unlike the other thin film technologies, all the materials comprising the device are non-toxic and earth-abundant [50] – [55]. Thin film Si layers are generally deposited via Plasma Enhanced Chemical Vapor Deposition (PECVD), a process in which gases are ionized in a radio frequency RF plasma then are deposited onto the substrate to form a thin film]. The advantage of this technique is that an entire Si PV device can be deposited using a single machine, where the layer composition, thickness, and crystallinity can be controlled by adjusting deposition parameters, like gas composition and flow rates, deposition temperature, deposition time, and source power. The crystallinity of thin film Si influences its band gap, going from 1.12 eV for a single crystal to 1.8 eV for a fully amorphous film [18] & [50] – [55].

A major issue with thin film Si solar cells is their large defect densities, which result in small diffusion lengths, necessitating the use of a configuration similar to the SHJ, known as the P-I-N configuration. The main difference is that the absorber is typically intrinsic. Thinner layers are desired for this technology to minimize defect related Shockley-Read-Hall (SRH) recombination in the solar cell [18].

These defects are represented by dangling bonds in the material, which can be passivated by incorporating hydrogen during processing. That is why, amorphous and nanocrystalline Si are denoted as, a-Si:H and nc-Si:H, respectively. As the material becomes more amorphous, the defect density increases, which further reduces the diffusion length, as well as the thickness limit for sufficient carrier collection [27].

The current stabilized single junction record efficiency of a-Si:H is 10.1% [56]. This low efficiency can be attributed to the Staebler-Wronski effect, wherein the initial efficiency drops by a relative 10 – 15% before stabilizing, due to light induced degradation [26]. Nanocrystalline nc-Si:H consists of nanocrystals embedded in an amorphous matrix and tend to have lower band gaps than a-Si:H. Furthermore, nc-Si:H does not suffer from light induced degradation [18]. The current record efficiency for nc-Si:H is 11.9% [57]. However, given the simplicity and cost-effectiveness of fabricating these materials, they are typically implemented in tandem or multi-junction configurations. The current record for a tandem a-Si:H/nc-Si:H is 12.7% [58], while the triple junction record of 14.8% goes to an a-Si:H/nc-Si:H/nc-Si:H solar cell [55].

Si alloys can also be implemented, such as Silicon Germanium (SiGe), Silicon Carbide (SiC), and Silicon Oxide (SiOx), by including appropriate precursor gases during PECVD, which would allow for further tuning the band gap and maximize spectral utilization in multi-junction solar cell configurations [60].

1.7. Multi-Junction Solar Cells

A major limitation to single junction solar cells is poor spectral utilization. As long as there is only one absorber, the solar cell will be optimized to only a particular part of the spectrum. Moreover, as earlier discussed, photon energies below the band gap will not get absorbed, while energies greatly exceeding the band gap, a significant portion of their energy is thermally lost. The Shockley-Quiesser (SQ) limit is defined as the theoretical efficiency limit for a single junction solar cell, accounting for optical mismatch losses and electrical losses associated with radiative recombination [61]. As can be seen in Figure 1.10, the ideal band gap for obtaining the highest SQ limited efficiency is around 1.34 eV [18].

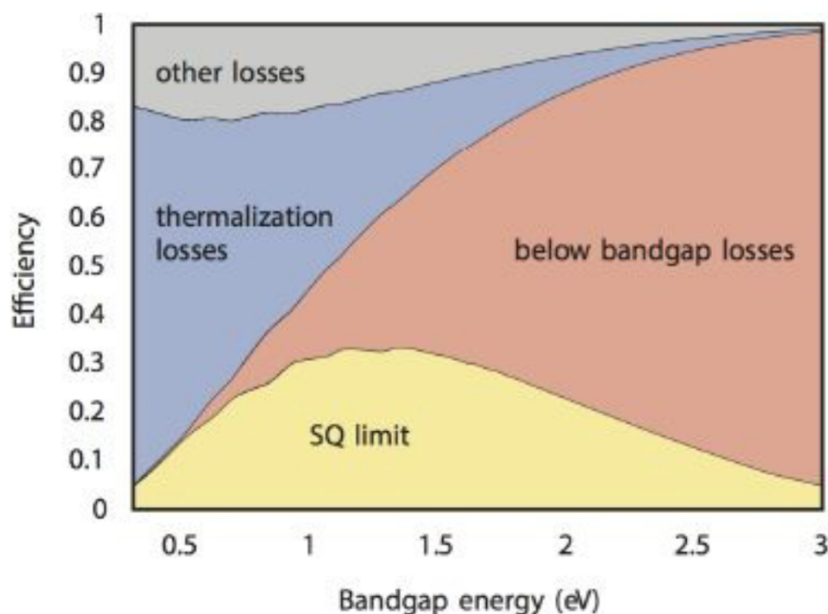


Figure 1.10: Major loss mechanisms in the Shockley-Quiesser limit under AM1.5 spectrum [18].

This issue can be remedied by stacking multiple solar cells, each optimized to absorb in a certain part of the spectrum, as shown in Figure 1.11 [62]. This will also reduce thermalization losses, as high energy photons are absorbed and better utilized in the high band gap cell, while non-absorption losses are diminished, as the lower band gap cells take care of low energy photons. The solar cells are ordered from lowest to highest band gap going from the bottom to the top, so that high energy photons get absorbed in the top layers, while longer wavelengths get absorbed in the bottom cells [54] - [60]. The thicknesses of the layers need to be optimized to ensure sufficient current matching between the cells, particularly in monolithic or 2-terminal configurations. Another attractive feature of these devices is their ability to generate large voltages, particularly when the cells are monolithically stacked in series, which is a crucial requirement for PEC applications [54].

Si PV is a very promising candidate for such devices, as the materials and fabrication process are highly cost-effective, since all solar cell layers can be deposited by PECVD all through the same instrument. But more notable is the fact that very large open circuit voltages (V_{oc}), up to 2.9 V have been achieved by integrating multiple Si thin film-based solar cells into a single device [54]. Another promising approach is processing thin film Si PV on top of an SHJ as wafer-based multi-junction solar cells, with c-Si serving as a high-performance bottom cell, while a tandem or triple junction Si thin film PV cell is stacked on top [63] & [64]. Wafer-based Si multi-junction solar cells have already reached $V_{oc} > 2$ V [63]

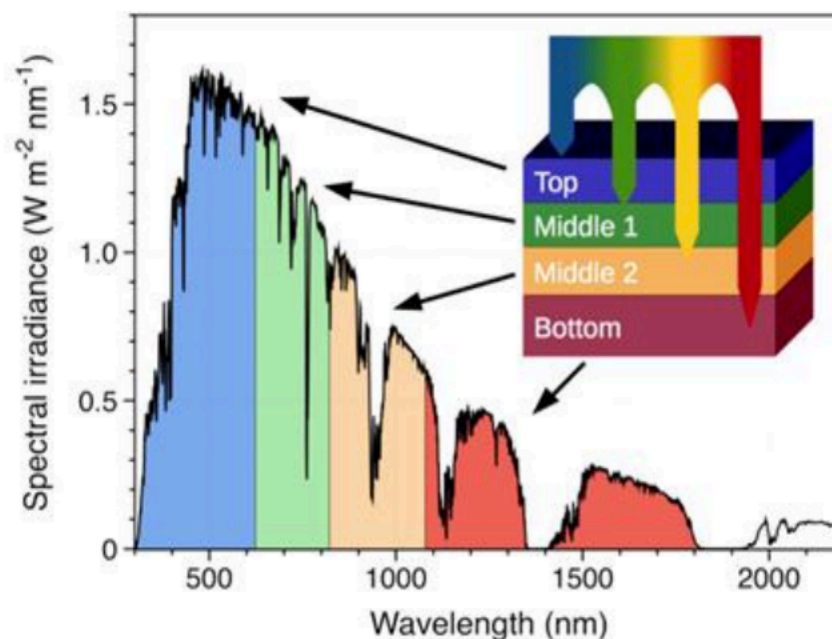


Figure 1.11: Spectral irradiance plot demonstrating the advantage of spectral utilization in multi-junction solar cells [62].

1.8. Photoelectrochemical (PEC) Solar to Fuel Conversion

As was earlier mentioned, the photovoltaic effect is not limited to photovoltaic applications, it can also be applied to systems like Photoelectrochemical (PEC) cells that generate fuels from the solar electrolysis of molecules, like the photoinduced electrolysis of water to generate hydrogen, or reduction of carbon dioxide to generate carbon monoxide (CO) and heavier fuels, such as methane, methanol, or formic acid [9] & [11]. While Solar-to-Hydrogen (STH) efficiencies have made progress over the years, with a record efficiency of 19.3% [65], PEC CO₂ reduction, or solar conversion to carbon-based fuels, has experienced much slower progress, owing to the larger voltage requirements

and complex reaction pathways involved in this process [9]. Therefore, the discussion will be limited to water-splitting or solar to hydrogen PEC cells.

1.8.1. PEC Water-splitting Principles

Figure 1.12 illustrates a typical PEC water-splitting cell in a photoanode configuration, meaning that the anode is the photoactive electrode [66]. It consists of:

- **Electrocatalysts:** an anode and a cathode that catalyze the Electrochemical EC half reactions and are electrically connected through a circuit.
- **Electrolytes:** which are the ionic charge carriers that travel in solution between the electrodes.
- **Photo-absorber:** which is responsible for generating the required photovoltage to drive the EC process upon illumination.

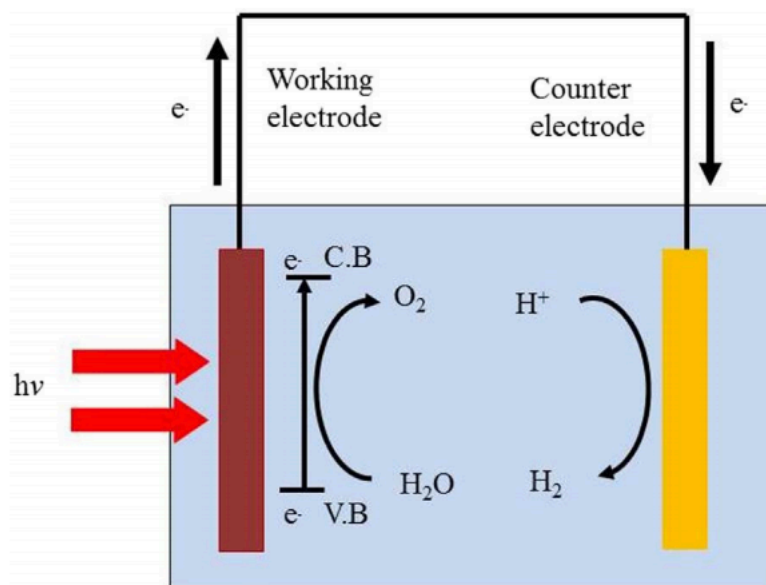


Figure 1.12: Illustration of a basic Photoelectrochemical (PEC) water splitting cell [66]. The red electrode is the anode, where water oxidizes into oxygen and protons. The yellow electrode is the cathode, where protons are reduced into hydrogen. The working electrode is the one that undergoes light absorption, in this case the anode.

The Oxygen Evolution Reaction (OER) takes place at the anode, where water is oxidized at the anode into protons (H^+) and O_2 gas. At the cathode, the Hydrogen Evolution Reaction (HER) occurs. Protons travel through the electrolyte solution towards the cathode, where they recombine with electrons flowing through the circuit to generate H_2 gas. At the anode side, electrons are injected from the electrolyte into the semiconductor, and from the semiconductor into the electrolyte at the cathode.

1.8.2. PEC Systems

In the simplest case, the photo-absorber could potentially be either one of the electrocatalysts and is denoted the working electrode. Though the standard potential for water splitting is around 1.23 V, the voltage requirement for a PEC cell to produce H_2 is actually higher (1.6 – 2 V) when losses are accounted for [9], [11] & [27]. The large voltage requirement results in poor spectral utilization if only one absorber is utilized [27]. This issue can be mended by having both electrocatalysts serve as photo-absorbers in tandem, to attain higher voltages with reasonable band gaps. Figure 1.13 highlights the band edge potentials at pH = 0 for different semiconductors versus a Normal Hydrogen Electrode (NHE) that can be used as photoelectrodes in this system [27]. A major drawback to using the

electrocatalysts as the absorbers is that the PN-junction is at the semiconductor/electrolyte interface, which is a lot more resistive and sluggish than a solid junction [9], [11] & [27]. Moreover, the potential difference between the electrolyte and the semiconductor influences the photogenerated voltage, as the band bending at the interface leads to Fermi level pinning [27].

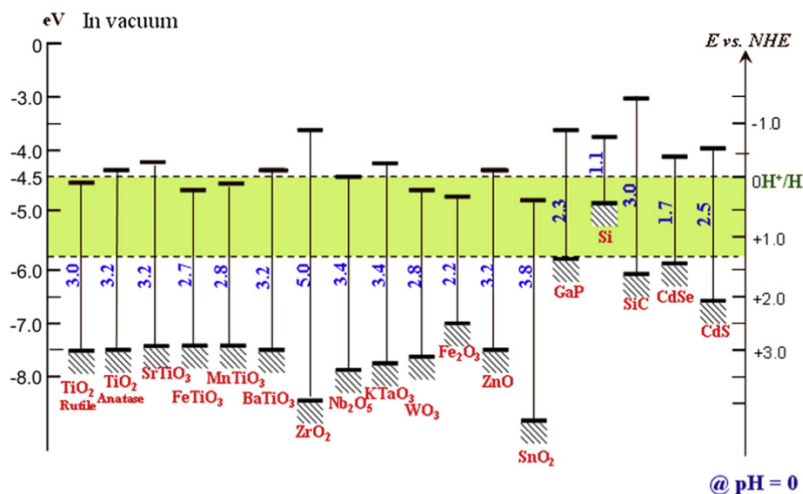


Figure 1.13: Band diagram showing the band edge potentials for semiconductors used in PEC water splitting at pH = 0 [27].

1.8.3. PV-EC Systems

In order to address the issues relating to a semiconductor/electrolyte photoactive junction, PV technologies can be implemented as the photovoltage source of the system [9], [11], [27] & [63]. The goal is to shield the PN-junction from the electrolyte, so as not to influence the photovoltage. This can be achieved in multiple configurations, as highlighted in Figure 1.14 [27]. The PV system can be externally connected to the PEC cell, where a converter can be included to further decouple the two systems and allow them to operate at their own optima. Though this type of system is more efficient in practice, it has relatively high system costs and complexity. The number of modules can be decreased by using multi-junction solar cells, since they can achieve higher photovoltage, which would reduce the area and amount of cabling required. The system can be further simplified by integrating the PV stack into the PEC system, which further reduces system size and cabling requirements.

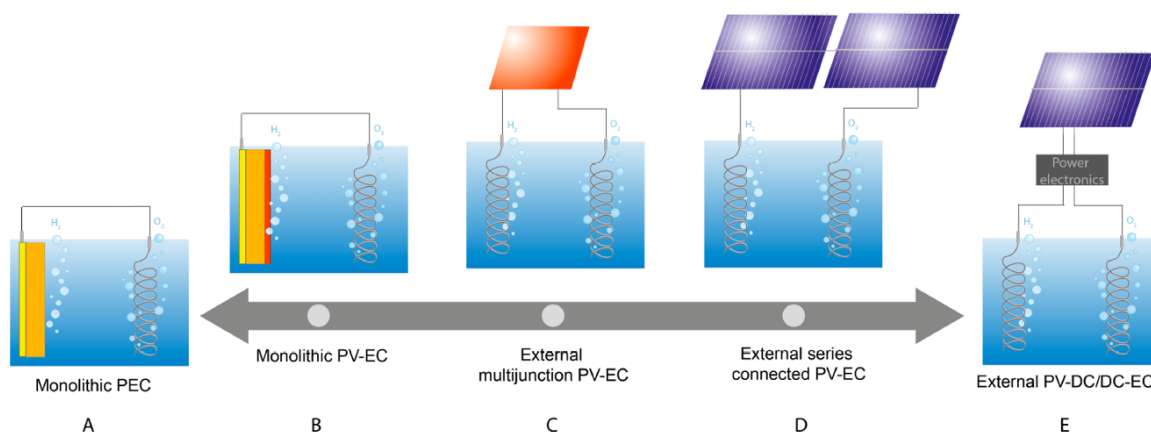


Figure 1.14: Different PEC configurations for water splitting from (A) Basic PEC cell without PV; (B) Monolithic (integrated) PV-EC cell; (C) External PV-EC cell using multijunction solar cell; (D) External PV-EC cell using array of single junction solar cells (E) fully decoupled PV-EC system via converter [27].

1.8.4. Wired vs Wireless

The device can be simplified even more, to the point of eliminating the wiring requirement altogether, by sandwiching the buried PV junction between the two electrocatalysts, which would dual as contacts for the solar cell, as shown in Figure 1.15(b) [67]. Instead of flowing through wires, electrons flow through the device stack from the anode to the cathode. As can be seen from Figure 1.16 [27], the highest STH efficiencies are achieved for PV-PEC based devices, with a monolithic III-V based PV-PEC cell holding the record of 19.3%.

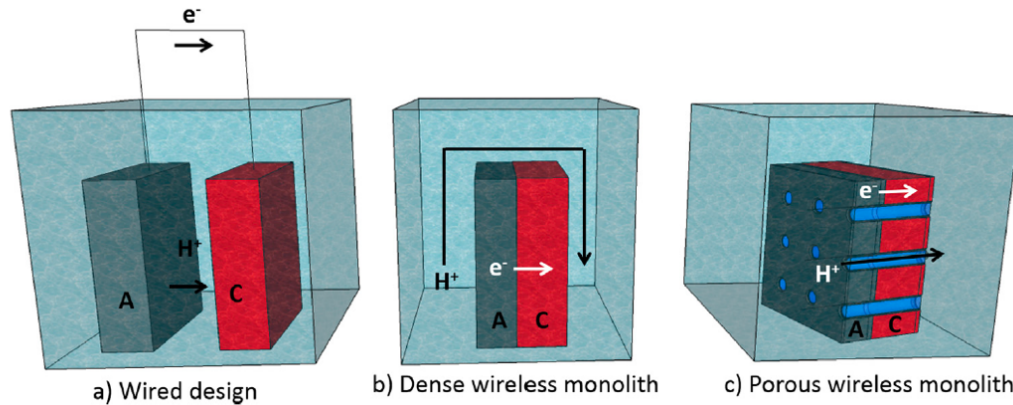


Figure 1.15: (a) Conventional wired configuration; (b) Dense configuration; and (c) Porous configuration [67].

Unfortunately, PEC cells based on cost-effective technologies have demonstrated poor performance in this dense wireless configuration relative to the wired system. The issue is that protons have to travel around the cell, encountering large distances to reach the cathode, which results in high ohmic losses, especially for technologies having low operational currents [67] – [69]. The problem gets worse with upscaling, as the wider and taller modules will further increase proton transport distances. This issue can be remedied by processing pores into the device that act as channels or shortcuts for ionic diffusion, making these losses independent from module size. However, it is important to note that pores form a bottleneck to proton flow, which limits their diffusion and develops a concentration gradient [67] – [70]. This gradient produces overpotentials that limit the device current, and ultimately the device efficiency [70]. Therefore, it is crucial that pore dimensions are optimized to limit obstruction to proton flow. Moreover, the pores result in loss of active area for light absorption, which limits the photo-generated current.

In a fully monolithic configuration, referred to here as a Porous-Monolithic-Photovoltaic-Electrochemical (PMP) cell, the electrode coverage at the illuminated side needs to be optimized in order to maximize light penetration into the solar cell. On the one hand, more electrode coverage means there is less active area available for light absorption. However, the electrocatalysts are also required to catalyze the Electrochemical (EC) half reactions. Thus, sufficient coverage is necessary.

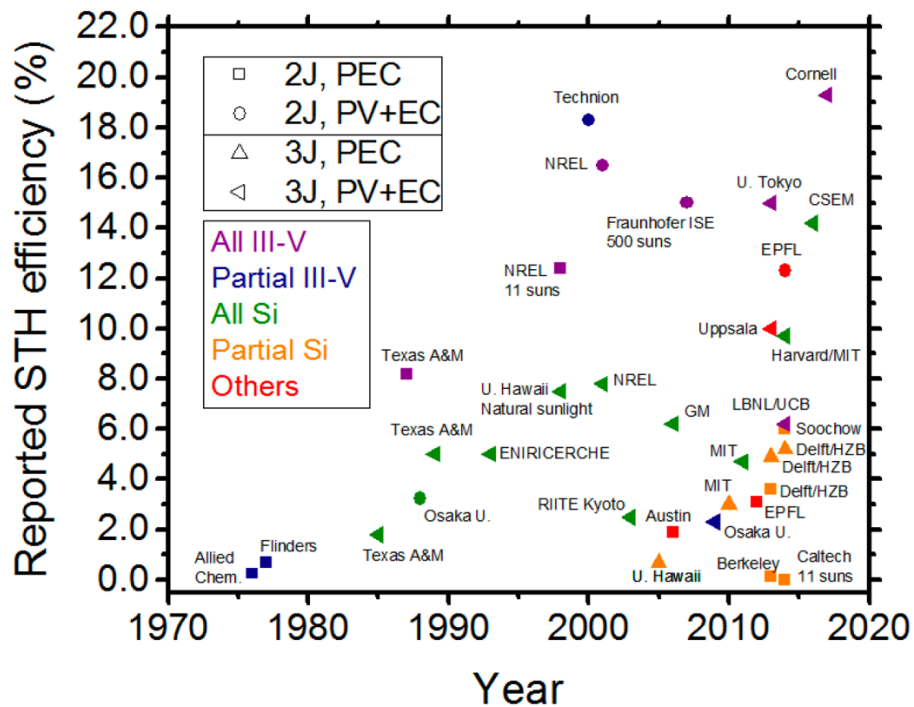


Figure 1.16: Reported Solar-to-Hydrogen efficiencies for different PEC and PV-EC technologies [27].

1.8.5. Pore Forming Methods

PMP cells can be processed on c-Si wafers that are $> 100 \mu\text{m}$ thick or thin film substrates, such as Si or Aluminum (Al) foils, which are on the order of tens of microns, same as the relevant range of hole diameters. Therefore, a suitable pore forming method should have the following criteria:

1. High resolution pore patterning capability
2. High drill or etch rates to avoid lengthy processing and ensure 100% penetration
3. Minimal influence on the electrical and morphological quality of the device
4. Practical implementation (low cost and complexity) in industrial manufacturing

From the literature it was found that Deep Reactive Ion Etching (DRIE) [71] – [73] and Pulsed or Percussive Laser Drilling (PLD) [74] – [76] are the most suitable pore forming methods for this application. Other etch/drilling methods, which are not as appropriate include:

1. **Electron Beam Lithography (EBL)** and **Ion Beam Lithography (IBL)**, which have slow etch rates on the order of nanometers/minute and would, thus, take too long to etch through tens to hundreds of microns of material [77] – [80].
2. **Electrical Discharge Machining (EDM)** involves the generation of a spark gap between the wafer and an electrode, which causes local heating and damages the device [81] – [82].
3. **Wet etching** is highly inappropriate for deep, straight and vertical pores ($> 10 \mu\text{m}$), since there is no directionality when etching in solution. The isotropic nature of this process would result in unilateral etching with minimal penetration depth through the device [83] – [84]

1.9. Previous Work

This PMP concept has already been investigated. Bosserez et al determined that ohmic overpotentials can be limited to < 100 mV if the spacing between the holes can be kept at a minimum < 0.25 mm spacing [68]. When considering a 0.25 M KOH electrolyte concentration, an ohmic overpotential of 78 mV was obtained. Trompoukis et al showed that pore dimensions on the order of a few to hundreds of microns constitute an ideal range for attaining low ohmic losses [67], which is in agreement with Bosserez et al.

A collaboration was done between the PVMD group at TU Delft and Twente University for processing PMP cells based on Si triple-junction PV, as shown in Figure 1.17 [70]. The pores were processed via DRIE. Several considerations were taken into account to address the limitations of this configuration, namely: (1) the formation of a pH gradient between the anode and cathode due to restricted proton flow between the electrodes and (2) product gas (H_2 and O_2) crossover, which in addition to reducing yields, poses a safety hazard. Both these issues were remedied by including Nafion[®] Proton Exchange Material PEM in the pores; and (3) contact shading, which required patterning the anode as microdots with an optimized coverage area of 5% [70]. A 2D COMSOL model was included to demonstrate the large pH gradient suppression that results from including micropores compared to the dense configuration [70]. The STH efficiency was found to be around 7%, compared to the non-porous and unpatterned PV efficiency of 10.8% [70]. It is possible that larger STH efficiencies can be obtained if the pore size and distribution are optimized.

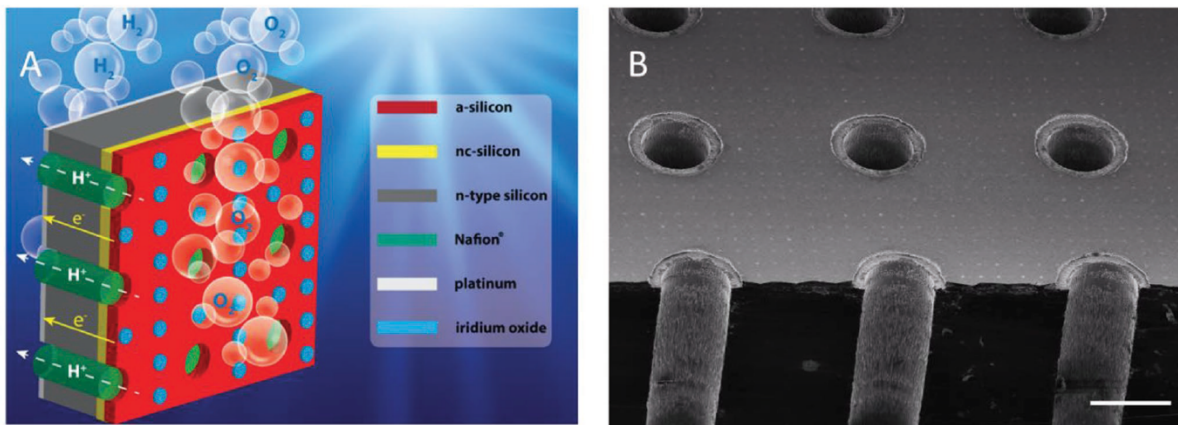


Figure 1.17: (A) Schematic of the PMP cell based on multi-junction Si solar cell with an a-Si:H/nc-Si:H/c-Si configuration [70]. The small blue circles are the anode microdots, the green material is the PEM inside the pores. The cathode (grey) is the cathode/back contact; (B) Scanning Electron Microscopy (SEM) image of a cross section of the PMP cell [70].

1.10. Thesis Project Goals and Outline

Pore size and distribution remains an area in need of optimization for enhancing the performance of PMP cells. The fact the ionic transport is a major contributor to performance loss highlights the importance of optimizing the hole configuration to one that minimizes the distances generated protons need to travel to reach the holes, while maximizing their flow inside the pores, at the same time ensuring that the porosity is low enough to maintain sufficiently high photocurrents. A delicate balance that needs careful assessment.

This thesis project aims at optimizing the pore size and distribution of PMP cells based on Si multi-junction PV to further enhance their performance. The main objectives are to:

1. Study the influence of pore size and distribution on the performance of PMP cells to define the range of optimal hole patterns:

- a. What is the influence of the pores on PV performance?
 - b. What is the influence of the pores on EC performance?
 - c. Is there an absolute optimum, or an optimal range of hole patterns?
2. Compare pore processing techniques, namely Deep Reactive Ion Etching DRIE and Pulsed or Percussive Laser Drilling PLD, to assess their suitability for different PMP technologies:
 - i. Which method yields better overall PV-EC device performance?
 - ii. Which method yields better pore dimensioning control and resolution?
 - iii. Which method is more practical to implement on an industrial scale?

A theoretical analysis is carried out that includes 2D simulations of PMP cells in COMSOL Multiphysics® 5.4 to model the evolution of pH gradients between the electrodes, which are then used as inputs for evaluating losses associated with ionic transport. The influence of porosity on PV performance is also taken into account in the analysis. An experimental procedure is developed for processing PMP cells, wherein the experimental dataset consists of eight hole patterns to study the influence of: (1) the pore diameter; (2) the pore spacing; and (3) the porosity on the PEC, PV, and overall performance.

This thesis is organized as follows: Chapter 1 served as an introduction to the basics of Photovoltaics as well as its implementation in the PEC generation of hydrogen. Chapter 2 will cover the theoretical background in relation to the research objectives at hand. The theoretical methods are presented in Chapter 3, which describes the framework for the 2D COMSOL simulations and their implementation in the theoretical optimization approach. Chapter 4 delves into the experimental methods, wherein the PMP cell processing and measurement equipment are discussed. The results from the theoretical analysis and experimental results are covered in Chapters 5 and 6, respectively. The report ends with Chapter 7, where the key conclusions regarding the research objectives at hand and the suggested recommendations will be highlighted.

2. Theoretical Background

In this chapter, the theoretical background relating to the work done in this thesis is presented. The Porous-Monolithic-Photovoltaic-Electrochemical (PMP) cell essentially consists of two components: (1) Photovoltaic (PV) component; (2) Electrochemical (EC) component. In order to understand the influence of pore size and distribution on the solar to hydrogen performance, it is important to, first, define the key parameters used to characterize the PV and EC performances, individually, as well as the types of losses that arise from each process.

2.1. PV Performance

In this section, the current-voltage relations in a solar cell are described, through which the PV performance is determined.

2.1.1. Ohm's Law

When charge carriers are photogenerated, they travel towards the terminals of the solar cell, completing the circuit. This flow of charge is by definition a current I which has the unit of Amperes (A) or Coloumbs per second (C/s). Thus, a larger density of charge yields a larger current. To eliminate the influence of cell area, the current can be expressed as a current density (A/m^2), denoted by (J). As was discussed in section 1.3.1, the conductivity of a material largely depends on the relative positioning of the VBE and CBE. Having a wider band gap increases the resistance to current flow, since more energy is needed to promote electrons to the conduction band. This explains the highly resistive nature of insulators. On the other hand, metals, having no band gap, are highly conductive, yielding a linear proportionality between the potential difference V applied across the metal and the generated current by means of the resistance R in the material, as per Ohm's law:

$$V = IR \tag{2.1}$$

The resistance of a particular material can be obtained from its resistivity ρ and geometrical dimensions as follows:

$$R = \rho \frac{L}{A} \tag{2.2}$$

Where A is the cross-sectional area of the material and L is its length.

2.1.2. J-V Characteristic of a Solar Cell

As was discussed in section 1.3.2, current flows across a PN-junction are governed by the potential established at the junction. In the absence of illumination and when no external bias is applied ($V_a = 0$), the built-in potential V_{bi} defines the voltage across the junction, wherein the drift and diffusion currents are in equilibrium. However, when V_a is non-zero, the potential across the junction varies as ($V_{bi} - V_a$).

If $V_a > 0$, a **forward bias** is applied and the barrier to diffusion is reduced, resulting in a recombination current density J_{rec} , driven by the flow of minority carriers into the quasi-neutral region of their respective region and their recombination with the majority carriers:

$$J_{rec}(V_a) = J_0 \exp\left(\frac{q(V_a - V_{bi})}{nk_B T}\right) \quad (2.3)$$

Where T is the temperature and $k_B = 1.382 \times 10^{-23}$ J/K is the Boltzmann Constant and q , also referred to as $e = 1.602 \times 10^{-16}$ C is the unit charge. n is the ideality factor, which influences the slope of the J-V curve. At low forward bias, n is closer to 2, indicating a slow J-V response. At higher bias, n is around 1, and the diffusion current increases faster as the built-in potential gets more significantly weakened. J_0 is the dark current density, which represents the flow of charges in the absence of illumination and an applied bias. It is not possible to completely nullify the current under such conditions, since free charge carriers can still be thermally generated and have non-zero concentrations. It is equivalent to the generation current J_{gen} in the dark and increases with temperature, as more free charge carriers are generated. J_0 needs to be kept as small as possible, as it limits the built-in potential.

If $V_a < 0$, a **reverse bias** is applied, the barrier is increased as more dopants get ionized, widening the SCR. With sufficient reverse bias, the forward current is halted, leaving only the dark current density flowing in the opposite direction uninfluenced by the bias until the threshold, or breakdown voltage is breached. The overall current density as a function of the applied bias in the dark is thus:

$$J(V_a) = J_{rec} - J_{gen} = J_0 \left[\exp\left(\frac{q(V_a - V_{bi})}{nk_B T}\right) - 1 \right] \quad (2.4)$$

Photocurrent Density

Upon illumination, minority charge carriers in the absorber (electrons for p-type, and holes for n-type) get excited and are electrically driven towards the adjacent material (n-type for electrons, and p-type for holes). This photocurrent density is directly proportional to the irradiance or generation rate G , as follows:

$$J_{ph} = qG(L_N + L_P + W) \quad (2.5)$$

Where W is the depletion width, and L_N and L_P are the minority carrier diffusion lengths for electrons in p-type and holes in n-type materials, respectively.

The maximal photocurrent density a solar cell can achieve is denoted as the short-circuit current density J_{sc} , which considers the case of zero voltage. The distinction between dark and light conditions can be seen in the J-V characteristic plot in Figure 2.1 [18]. The photocurrent simply offsets the J-V curve from zero and the net current density becomes:

$$J_{net}(V_a) = J_0 \left[\exp\left(\frac{q(V_a - V_{bi})}{nk_B T}\right) - 1 \right] - J_{ph} \quad (2.6)$$

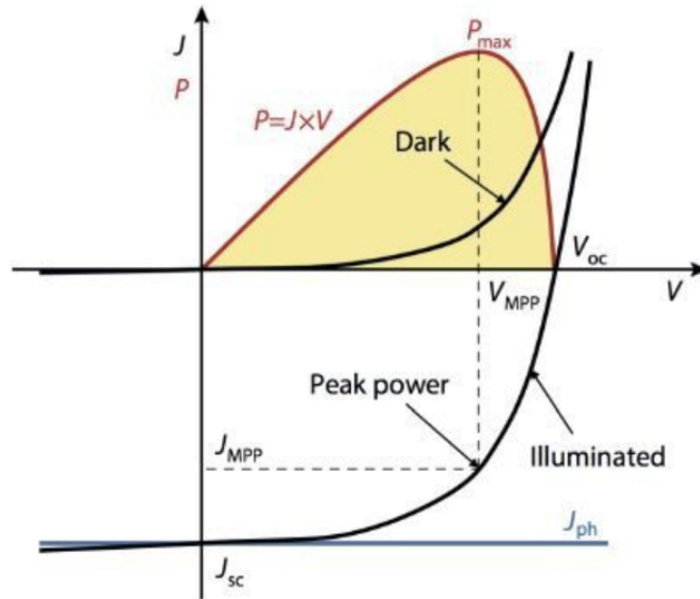


Figure 2.1: J-V Characteristic of a solar cell in the dark and under illumination [18].

Open Circuit Voltage

The J-V curve in Figure 2.1 shows that as the forward bias is increased, the photocurrent, initially, drops with a very slow slope, essentially forming a plateau until the bias is significant enough to compete with the built-in potential. At that point, the current reduces steeply, and intersects the voltage axis. At that bias, the diffusion current and photocurrent cancel each other out, as the forward bias balances the built-in potential, resulting in net-zero current. The open circuit voltage V_{oc} is the maximum potential that a solar cell can produce, when no current is flowing. It can be expressed in terms of the photocurrent density by considering net-zero current conditions:

$$V_{oc} = \frac{k_B T}{q} \ln \left(\frac{J_{ph}}{J_0} + 1 \right) \quad (2.7)$$

Maximum Power Point (MPP) Parameters

It is not possible to generate power under zero current or zero voltage conditions, since:

$$P = VI \quad (2.8)$$

Substituting J for I converts the power [W] into power density [W/m^2]. As shown in Figure 2.1, the power reaches a maximum power point MPP. This represents the maximum power output (P_{MPP}) that the solar cell can produce and is expressed as the product of the MPP voltage and MPP current, V_{MPP} and I_{MPP} , respectively.

Fill Factor

The quality of a solar cell can be evaluated from a parameter known as the Fill Factor, or FF, which is, by definition:

$$FF = \frac{P_{MPP}}{V_{oc} J_{sc}} \quad (2.9)$$

The product ($V_{oc} \times J_{sc}$) represents the hypothetical (unreachable) maximum power. So, a FF closer to 1 is indicative of a higher quality, since that means that the maximum possible output power is closer to ($V_{oc} \times J_{sc}$).

Shunt and Series Resistance

The FF is exclusively influenced by the resistances in the device. There are two types of resistance: (1) **series resistance** R_s , which represents resistances along the main power flow direction, characterized by the resistivities of the materials, as well as defects present in the device layers and their interfaces; and (2) **shunt resistance** R_p , which is resistance to electrical pathways off the main power flow direction. R_s needs to be minimized as much as possible, otherwise there will be too many voltage drops along the current path, which shifts the maximum power point to a lower voltage, as shown in Figure 2.2 [85]. R_p , on the other hand, should be very high, on the order of thousands of Ohms, otherwise, large portions of the current will get redirected off the main path, resulting in a quicker decline in current, as shown in Figure 2.2. When R_s and R_p are considered, a more complex J-V relation arises [18]:

$$J_{net}(V_a) = J_0 \left[\exp\left(\frac{q(V-IR_s)}{nk_B T}\right) - 1 \right] - \frac{V-IR_s}{R_p} - J_{ph} \quad (2.10)$$

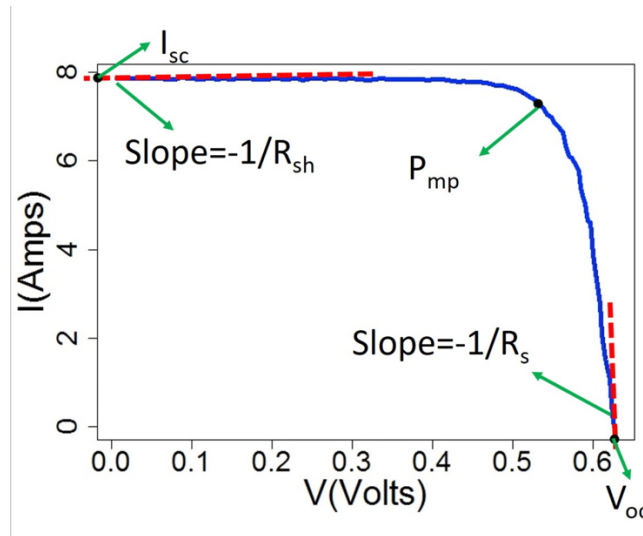


Figure 2.2: Current-voltage plot of a solar cell showing the influence of R_s and R_p [84].

Photovoltaic Efficiency η_{PV}

Now that the key PV parameters have been discussed, it is possible to express the photovoltaic efficiency, considering the AM1.5 incident power density, $P_{in} = 1000 \text{ W/m}^2$:

$$\eta_{PV} = \frac{P_{MPP}}{P_{in}} = \frac{FF \times V_{oc} \times J_{sc}}{P_{in}} \quad (2.11)$$

2.1.3. External Quantum Efficiency (EQE)

The External Quantum Efficiency (EQE) is defined as the ratio of collected charge carriers to the number of absorbed incident photons. This is a wavelength dependent entity, as the photon flux is also wavelength dependent and directly proportional to the photocurrent. Therefore, the EQE is obtained at each wavelength, by shining monochromatic light on the solar cell and measuring the photocurrent. The wavelength dependent EQE is related to the photon flux and photocurrent via:

$$EQE(\lambda) = \frac{I_{ph}(\lambda)}{q\phi_{ph}(\lambda)} \quad (2.12)$$

Where ϕ_{ph} is the photon flux. Figure 2.3 shows an example of an EQE for a high performing c-Si solar cell [18]. As can be seen, the EQE never reaches 1, which is expected when losses are considered. The J_{sc} is determined by integrating over the relevant wavelength range in the EQE plot. The J_{sc} obtained from the EQE is more accurate than the current from the J-V plot. Only photons that lead to charge carrier collection are considered, which removes the influence of transmission, reflection, parasitic absorption, and inaccuracy in cell area on the overall current density. The J_{sc} from the EQE measurement can be substituted into (2.11) to yield a more accurate PV efficiency.

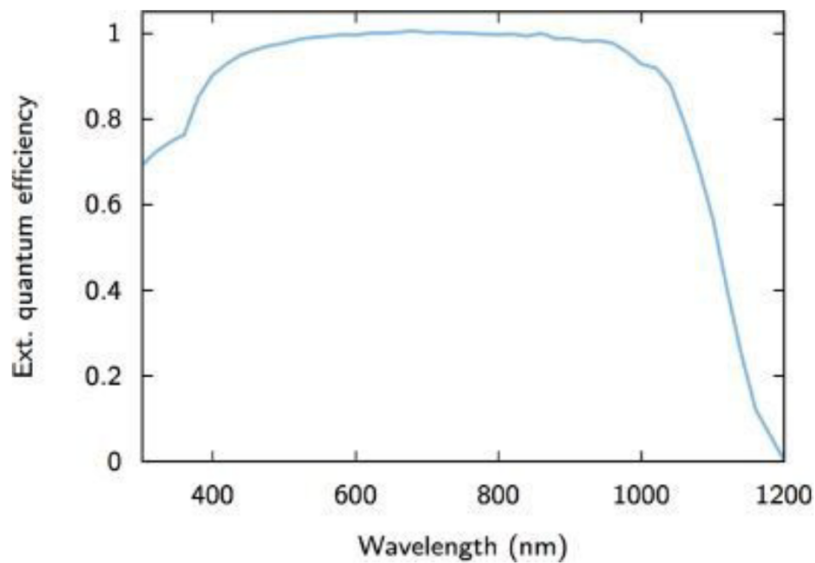


Figure 2.3: EQE plot for a high performing c-Si based solar cell [18].

2.1.4. PV Losses

Losses in a solar cell can be divided into the following categories:

Electrical Losses: As was discussed earlier in this section, solar cells experience electrical losses in the form of ohmic losses, or resistances in the device layers, at the interfaces, and at the contacts. There are also recombination losses, as described in Chapter 1, that take place in the absorber and emitter regions.

Optical Losses: In addition to the non-absorption and thermalization losses discussed in Chapter 1, one must also consider losses due to reflection at the front surface and internal reflection at the interfaces of the device layers. Transmission losses can occur at the backside if the absorber is not thick enough to absorb all incident photons, or if no back reflector is implemented. Parasitic absorption takes place in layers other than the absorber, resulting in photogeneration losses.

Solar cells require metallic contacting on both sides to enhance lateral conduction at the surface and collect charge carriers. However, the surface area covered by metal is shaded and will not receive illumination, leading to a reduction in the photocurrent. This effect is also present in special PV applications that require processing pores into the device.

Front Contact Shading

The influence of front contact shading can be defined by the contact coverage factor:

$$\theta_C = \frac{A_C}{A_T} \quad (2.13)$$

Where A_T and A_C are the surface areas of the whole device and the contact, respectively. The associated PV performance losses are expressed by the effective short-circuit current density $J_{sc,eff}$, effective open circuit voltage $V_{oc,eff}$, and effective PV efficiency $\eta_{PV,eff}$ as:

$$J_{sc,eff} = (1 - \theta_C)J_{sc,eff} \quad (2.14)$$

$$V_{oc,eff} = V_{oc} + \frac{k_B T}{nq} \ln(1 - \theta_C) \quad (2.15)$$

$$\eta_{PV,eff} = \frac{FF \times V_{oc,eff} \times J_{sc,eff}}{P_{in}} \quad (2.16)$$

In the context of the PMP cell, a geometry worth analysing is the anode microdot configuration. In which case:

$$A_C = \frac{1}{4} N_\mu \pi D_\mu^2 \quad (2.17)$$

Where N_μ is the number of microdots and D_μ is the microdot diameter. On the other hand, as noted in the 2.1.1, increasing the surface area of the contact results in smaller series resistance, thus the contact coverage should be large enough to minimize ohmic losses.

Porosity

The PMP cell involved in this study requires processing periodic cylindrical pores into the device in order to reduce ionic transport distances and minimize ohmic losses. Unfortunately, pore integration also reduces the available active area for light absorption, thus having an influence on PV performance similar to that of contact shading. Since the pores go through the device, the losses are not limited to the surface, but are instead volumetric and can be expressed in terms of the pore volumetric coverage factor θ_P :

$$\theta_P = \frac{V_P}{V_T} \quad (2.18)$$

Where V_P is the total pore volume, while V_T is the total device volume. Ideally, all the pores are cylindrical and have vertically straight sidewalls (no taper). In that case, V_P is the volume of a cylinder multiplied by the number of pores:

$$V_{pores} = \frac{1}{4} N_P \pi h_P D_P^2 \quad (2.19)$$

Where N_P is the number of pores, D_P is the pore diameter, and h_P is the pore depth. Since h_P cancels out in the expression of θ_P , the volumetric coverage factor is the same as the surface coverage factor when the pores are ideally straight.

Due to machining limitations or unoptimized conditions, especially in the case of thick devices, the pores may experience tapering, wherein the pore diameter is not consistent along the pore depth. A

positive taper is when the entrance hole > exit hole, while a negative taper is when the entrance hole < exit hole, as shown in Figure 2.4.

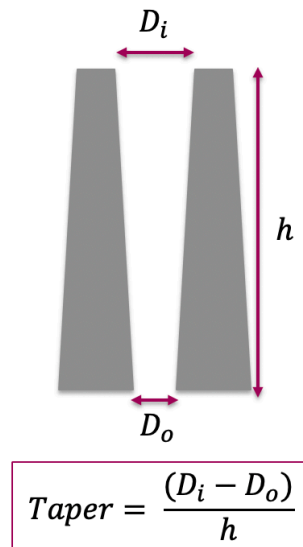


Figure 2.4: Tapering illustrated in 2D.

In that case, the pore diameter varies between D_i (entrance hole diameter) and D_o (exit hole diameter) across the pore depth, so the total pore volume can be estimated as that of a circular truncated cone:

$$V_{pores} = \frac{N_p \pi h}{3} (D_i^2 + D_i D_o + D_o^2) \quad (2.20)$$

Note that the diameter may vary non-linearly, as in the cases shown in Figure 2.5. This non-linearity results in a more complex formulation of the total pore volume. It should be noted that in the above analysis, light absorption is assumed to be uniform throughout the entire device. However, in the case of thick multi-junction devices, such as c-Si wafer PMP cells, most of the absorption takes place in the top part of the device, meaning that part of the pore volume may not influence PV performance, and may result in an under-estimated θ_p .

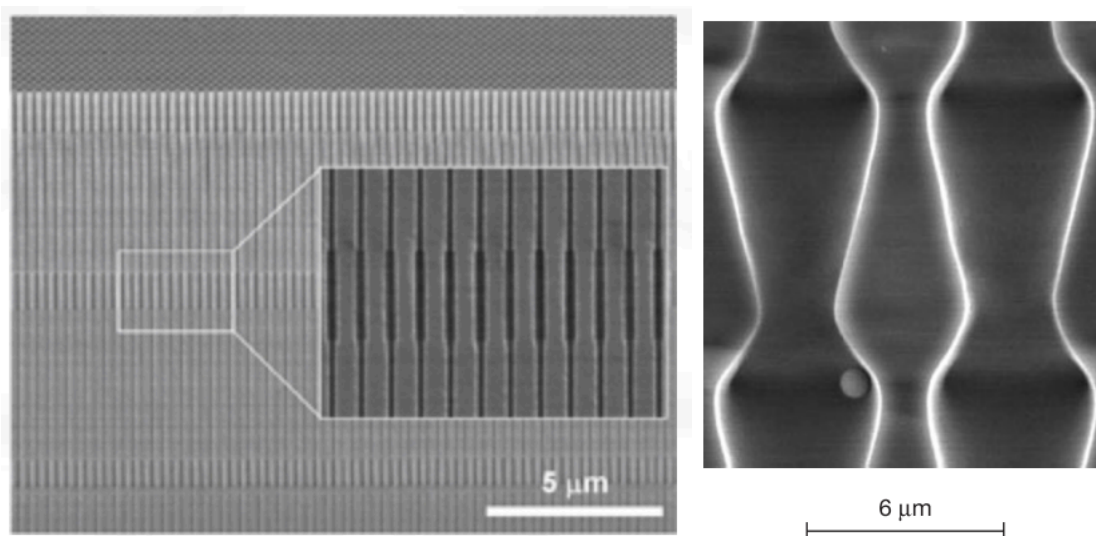


Figure 2.5: Examples of pores with modulated diameters [86].

To account for both front contact coverage θ_c and pore coverage θ_p , the overall coverage factor $\theta_{overall}$ is simply the sum of the two ($\theta_{overall} = \theta_c + \theta_p$) and the effect on PV performance is also expressed in formulations similar to (2.14) – (2.16), replacing θ_c with $\theta_{overall}$.

2.2. PEC Performance

The standard change in Gibbs free energy for the water splitting process $\Delta G^0 = 237 \text{ kJ/mol}$. Since $\Delta G^0 > 0$, this reaction is unfavourable and requires an input of energy to proceed [18]. As shown in Figure 2.6, when ΔG becomes more positive, the potential energy barrier to go from reactants to products increases, making the process less spontaneous.

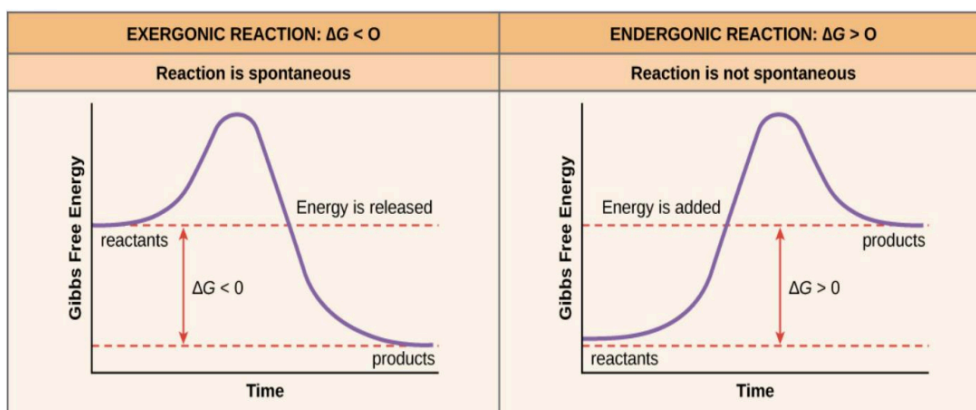


Figure 2.6: Thermodynamics plot of the Gibbs free energy versus time. A positive ΔG indicates a barrier for the reaction to proceed, whereas a negative ΔG represents a spontaneous reaction [87].

2.2.1. Chemical Definition of STH Efficiency

The Solar to Hydrogen (STH) efficiency of a PEC cell is chemically defined as the ratio of the power produced from combining the photo-generated hydrogen with oxygen to the incident solar power. Since oxygen is readily available in the atmosphere, the amount of power that can be delivered from the electrolysis of water is quantified as the product of the rate of H_2 production in mol/s and ΔG^0 . Therefore, the STH efficiency at STC can be expressed as [88]:

$$\eta_{STH,chem} = \frac{\frac{\text{mol}_{\text{H}_2}}{\text{s}} \times \Delta G^0}{P_{in}} \quad (2.21)$$

Therefore, by measuring the H_2 production rate via techniques like Gas Chromatography or Mass Spectrometry, it is possible to evaluate the STH performance of a PEC cell.

2.2.2. Electrical Definition of STH Efficiency

The standard Gibbs free energy is related to the standard potential via the following equation [89]:

$$\Delta G_{cell}^0 = -nFE_{cell}^0 \quad (2.22)$$

Where n is the number of moles of charge, $F = 96.485 \text{ C/mol}$ is Faraday's Constant, and E_{cell}^0 is the standard Reduction-Oxidation (RedOx) potential of the PEC cell. Thus, a positive E_{cell}^0 represents a favourable process (galvanic), whereas a negative potential is unfavourable (electrolytic).

The water-splitting process takes place via the following RedOx reactions, depending on the pH of the electrolyte solution. The standard electrode potentials at extreme pH conditions are also included [9] & [11]:

	<u>Acidic Half Cell Reactions</u>	(pH = 0)
Anode	$2H_2O + 4h^+ \rightarrow O_2 + 4H^+$	$E^0_{Anode} = -1.23 \text{ V}$
Cathode	$4H^+ + 4e^- \rightarrow 2H_2$	$E^0_{Cathode} = 0.00 \text{ V}$
Overall	$2H_2O \rightarrow 2H_2 + O_2$	$E^0_{WS} = -1.23 \text{ V}$
	<u>Basic Half Cell Reaction</u>	(pH = 14)
Anode	$4OH^- + 4h^+ \rightarrow O_2 + 2H_2O$	$E^0_{Anode} = -0.401 \text{ V}$
Cathode	$4H_2O + 4e^- \rightarrow 2H_2 + 4OH^-$	$E^0_{Cathode} = 0.829 \text{ V}$
Overall	$2H_2O \rightarrow 2H_2 + O_2$	$E^0_{WS} = -1.23 \text{ V}$

At low pH levels, $[H^+] \gg [OH^-]$, since [90]:

$$[H^+] = 10^{-pH} \quad (2.23)$$

And the auto-ionization constant of water K_w is [90]:

$$K_w = [H^+][OH^-] = 10^{-14} [M^2] \quad (2.24)$$

This favours the acidic reactions, while the opposite is true under basic conditions. Figure 2.7 illustrates the influence of pH on the electrode potentials, which decrease linearly such that the difference between the two half cells E^0_{WS} remains constant:

$$\Delta E^0_{WS} = E^0_{Anode} - E^0_{Cathode} = -1.23 \text{ [V]} \quad (2.25)$$

Therefore, at any pH level, the overall water splitting reaction is not spontaneous and requires a voltage input $\geq E^0_{WS}$ to proceed.

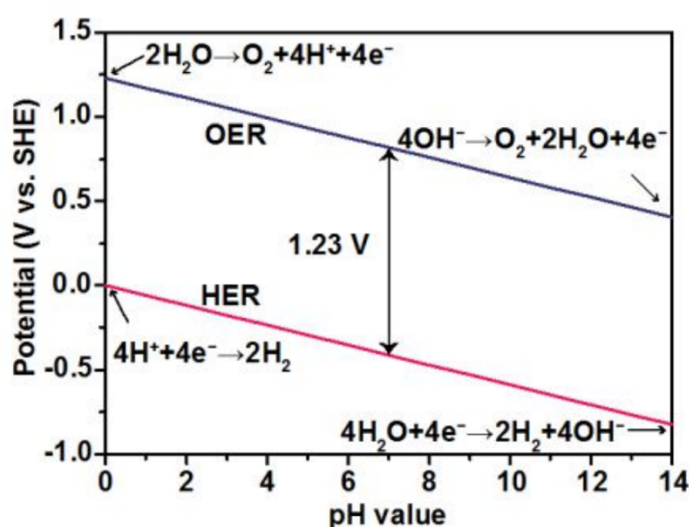


Figure 2.7: Plot of the water splitting electrode potentials versus the pH [91].

The devices in this work are based on Si, which is more susceptible to etching under basic conditions. Therefore, the remainder of this discussion will only consider PEC processes under acidic conditions.

The Nernst Equation

The RedOx species concentrations at the electrodes can be related, under any condition, via the reaction quotients, with the reduced species conventionally set as the product:

$$Q = \frac{[Reduced]^m}{[Oxidized]^n} \quad (2.26)$$

Where m and n are the stoichiometric coefficients of the reduced and oxidized species, respectively. The magnitude of the reaction quotient indicates which direction the reaction will proceed in. The potential at each electrode depends on the concentrations of the participating ionic species and can thus be described by the Nernst equation [92]:

Anode Potential:

$$E_a = E_a^0 + \frac{RT}{nF} \ln(Q_a) \quad (2.27)$$

Cathode Potential:

$$E_c = E_c^0 + \frac{RT}{nF} \ln(Q_c) \quad (2.28)$$

Where R = 8.314 J/mol.K is the universal gas constant and the quantity RT/F = 0.059 eV at STC. In the case of acidic water-splitting, the only ionic species involved in both half-cell reactions is H⁺, such that the oxidation of every 4n protons generated at the anode, another 4n protons are reduced into 2n hydrogen molecules at the cathode. Therefore, the reaction quotients can be expressed as:

$$Q_{OER} = [H_a^+]^{4n} \quad (2.29)$$

$$Q_{HER} = [H_c^+]^{4n} \quad (2.30)$$

The HER at the cathode represents the Standard Hydrogen Electrode (SHE), which is set as a universal reference and has, by definition, a standard potential of 0.00 V under STC of 25 °C, [H⁺] = 1M, and pressure = 1 atmosphere for both the forward and backward reactions. Thus, it is possible to express the RedOx potentials in terms of the proton concentration at each electrode as:

Anode Potential:

$$E_{OER} = 1.23 + 0.059 \ln(Q_{OER}) \quad (2.31)$$

Cathode Potential:

$$E_{HER} = 0.00 + 0.059 \ln(Q_{HER}) \quad (2.32)$$

With the cathode serving as the ground electrode, the potential difference $\Delta\phi_s = E_{OER} - E_{HER}$ represents the required voltage to drive the PEC generation of hydrogen.

Ideal PEC Behaviour

Ideal PEC behaviour implies lossless ionic transport, wherein every proton generated at the anode gets consumed at the cathode. Therefore, under such conditions and considering both electrodes are submerged in the same solution, the water splitting reaction should not influence the equilibrium solution concentration, resulting in a homogeneously distributed pH between the electrodes.

This is demonstrated via the Nernst equation. When $[H^+_c] = [H^+_a]$, the logarithmic terms cancel out and $\Delta\phi_S = 1.23$ V, the standard water splitting potential. Thus, under such conditions, there are no additional voltages, or overpotentials, required to drive the EC process.

Activation Overpotential

In reality, however, PEC cells encounter losses due to electrode activation energy requirements and ohmic losses in the device layers, as well as in the electrolyte. The latter bears a significant limiting effect, given that the conductivity of ions (< 1 S/cm) is considerably smaller than that of electrons (10^5 S/cm). Moreover, protons may interact with other species in solution, or more notably, combine with each other to form hydrogen before reaching the cathode. This is further aggravated if the geometry of the system leads to restricted proton flow between the electrodes. As protons are generated at the anode, the pH will be lower there than it is at the cathode and the excess of protons at the anode induces the generation of hydrogen near the anodically produced oxygen. This is known as product gas cross-over, which, in addition to reducing hydrogen yields, poses a safety hazard, given the explosive nature of the water forming reaction.

It is possible to characterize the losses associated with proton transport as activation overpotentials E_{Loss} via the pH gradient that develops between the two electrodes. It is defined as the additional voltage needed to overcome losses in the EC system in order to leave sufficient potential to drive the EC reactions:

$$E_{Loss} = \Delta\phi_S - E_{WS}^0 \quad (2.33)$$

For example, if:

$$[H^+_a] = 1.2 \text{ M} \rightarrow E_{OER} = 1.234 \text{ V}$$

$$[H^+_c] = 0.9 \text{ M} \rightarrow E_{HER} = -0.003 \text{ V}$$

$$E_{Loss} = \Delta\phi_S - E_{WS}^0 = 1.237 - 1.23 = 0.007 \text{ V} = 70 \text{ mV}$$

This means that 70 mV of additional voltage are required to drive the water splitting reactions.

Electrochemical Reaction Kinetics

As was earlier noted, the RedOx reactions generate a Charge Transfer (CT) current density, represented by the flow of protons from the anode to the cathode. The CT current is related to the rates of the half-cell reactions that occur at the electrode surface, which have an Arrhenius dependence on the potential difference $\Delta\phi$ [92] & [93]:

$$k_f = k_{f,0} \exp\left(\frac{-(1-\alpha)nF\Delta\phi_S}{RT}\right) \quad (2.34)$$

$$k_r = k_{r,0} \exp\left(\frac{\alpha nF\Delta\phi_S}{RT}\right) \quad (2.35)$$

$k_{f,0}$ and $k_{r,0}$ are the rate constants for the forward (cathodic) and reverse (anodic) reactions, respectively. α is the transfer coefficient, or the fraction of electrostatic potential energy contributed to either the anodic/cathodic current density J_C/J_A . Thus, $(1 - \alpha)$ is the potential energy contribution to other process, J_A/J_C , respectively. The overall CT current density J_{CT} is, hence, obtained as:

$$J_{CT} = J_A - J_C = nFk_f C_R - nFk_r C_O \quad (2.36)$$

Where C_R and C_O are the products of the concentrations of reduced and oxidized species at the surface of the electrode, respectively, each raised to the power of their stoichiometric coefficients. At equilibrium potential ($\Delta\phi_s = E_{WS}^0$), the net current is zero and $J_A = J_C = J_{exc}$ the exchange current density:

$$J_{exc} = nFk_{f,0}C_O \exp\left(\frac{-(1-\alpha)nFE_{WS}^0}{RT}\right) = nFk_{r,0}C_R \exp\left(\frac{\alpha nFE_{WS}^0}{RT}\right) \quad (2.37)$$

Therefore, the current density J_{BV} induced by the activation overpotential can be expressed via the Butler-Volmer (BV) equation:

$$J_{BV} = J_{exc} \left[\exp\left(\frac{-(1-\alpha)nF}{RT} E_{Loss}\right) - \exp\left(\frac{\alpha nF}{RT} E_{Loss}\right) \right] \quad (2.38)$$

J-E Characteristic

As was earlier determined, in order for the EC current to be maximized, $E_{Loss} \rightarrow 0$. This is represented by an un-interrupted proton flow between the electrodes and the consequent homogeneity in proton concentration in the system. The J-E plot in Figure 2.8 indicates that that is the case when the Butler-Volmer current density $J_{BV} \rightarrow 0$ [92] – [95]. That is expected, since J_{BV} is generated from the pH imbalance between the electrodes and serves as the magnitude of the associated current loss. Note that η in Figure 2.8 represents E_{Loss} .

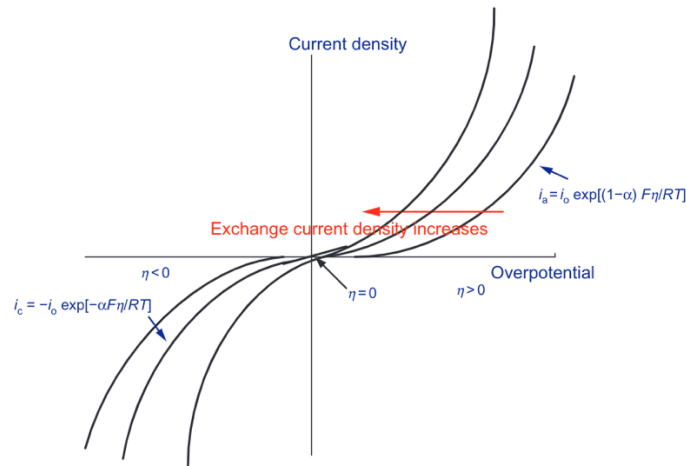


Figure 2.8: J- η characteristic of a PEC cell, demonstrating the influence of the exchange current density and overpotential on PEC performance [92].

At low overpotentials, the Butler-Volmer equation reduces to a linear current-overpotential relation:

$$J_{BV, E_{Loss} \rightarrow 0} = J_{exc} \frac{\alpha nF}{RT} E_{Loss} \quad (2.39)$$

As the overpotential increases in magnitude, the J-E relation becomes non-linear. For large $|E_{Loss}| \gg RT/nF$, and depending on the sign of E_{Loss} , either J_A or J_C will become dominant and the Tafel equation is obtained:

$$E_{Loss} = -\frac{RT}{(1-\alpha)nF} \ln\left(\frac{J_{BV}}{J_{exc}}\right) \quad \text{For } E_{Loss} \gg \frac{RT}{nF} \quad (2.40)$$

$$E_{Loss} = \frac{RT}{(\alpha)nF} \ln\left(\frac{J_{BV}}{J_{exc}}\right) \quad \text{For } E_{Loss} \ll -\frac{RT}{nF} \quad (2.41)$$

The large overpotential driving the dominant half-cell reaction, consequently, forms a large barrier to its RedOx counterpart, thus limiting the progression of the overall reaction.

For non-zero overpotential, the CT current density experiences losses that can be quantified in terms of J_{BV} . The actual CT current density after accounting for pH gradient related losses is defined here as:

$$J_{pH} = J_{CT} - J_{BV} \quad (2.42)$$

Electrically, the STH efficiency is a function of J_{pH} and E_{WS}^0 and is defined as:

$$\eta_{STH,elec} = \frac{J_{pH} \times \Delta E_{WS}^0 \times \eta_f}{P_{in}} \quad (2.43)$$

Where η_f is the Faradaic efficiency, which describes the efficiency of charge transfer in the EC process. If the Faradaic efficiency is assumed large ~ 1 , the efficiency is solely dependent on the current density, which, thus, needs to be maximized.

2.3. Overall PV-EC Performance

The performance of an integrated PV-EC system is obtained from the superposition of the J-V and J-E characteristics of the PV and EC processes, respectively. This is illustrated in Figure 2.9, where the intersection point between the two plots highlights the operational point (OP) of the PV-EC system [9]. The overall STH efficiency in that case is expressed in terms of the operational current density J_{OP} :

$$\eta_{STH,overall} = \frac{J_{OP} \times \Delta E_{WS}^0 \times \eta_f}{P_{in}} \quad (2.44)$$

Since the potential requirement for driving the EC process under lossless conditions is E_{WS}^0 , increasing the operational voltage V_{OP} does not enhance device performance. In fact, lower overpotentials and a stronger rectification of the EC current result in a higher J_{OP} . Inversely, if the OP lies at a potential beyond the MPP of the solar cell, the intersection occurs in the low current region of the current voltage plot. η_{STH} cannot exceed η_{PV} due to pore and front electrode coverage, which limits the photogenerated current. Therefore, in addition to having a large built-in potential to overcome overpotentials, for PV technologies to qualify for PEC water splitting, they should also yield large photocurrents to achieve high STH efficiencies.

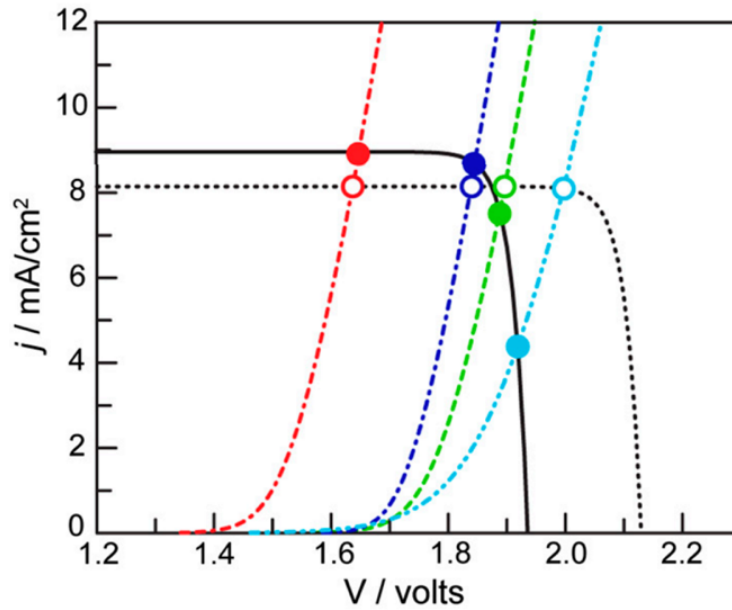


Figure 2.9: Overlap of PV and PEC current voltage characteristics for determining the operational point of the PV-PEC system [9].

2.4. Overall Performance of PMP Cells

The record STH efficiency was achieved for a wireless monolithic PV-EC device based on a III-V triple junction solar cell. The device was based on the dense configuration, yet still managed to retain $\sim 85\%$ of the PV current, yielding a J_{OP} of 15.7 mA/cm^2 [65]. However, the cost constraints and process complexity limit the commercial viability of this technology. Earth-abundant and cost-effective photovoltaics that can generate high photovoltages, unfortunately, yield much lower photocurrent densities $< 10 \text{ mA/cm}^2$ and experience significantly higher ohmic losses compared to III-V technologies.

2.4.1. PMP Cell Configuration

In order to overcome the challenges encountered by a dense fully integrated cost-effective PV-EC cell, pores can be processed into the device to serve as channels or shortcuts that shorten ionic transport distances, thereby leveraging the relatively poor performance of these materials, and allowing for larger STH efficiencies to be achieved. Vijselaar et al modelled the influence of including pores into the device architecture on suppressing the pH gradient between the electrodes, which, as highlighted earlier in this chapter, is a measure of the losses associated with ionic transport [70]. As shown in Figure 2.10, the pH gradient is largely suppressed from $\Delta\text{pH} = 7.5$ to 0.61 pH units when the pores are included, which corresponds to a significant reduction in overpotentials $\sim 390 \text{ mV}$.

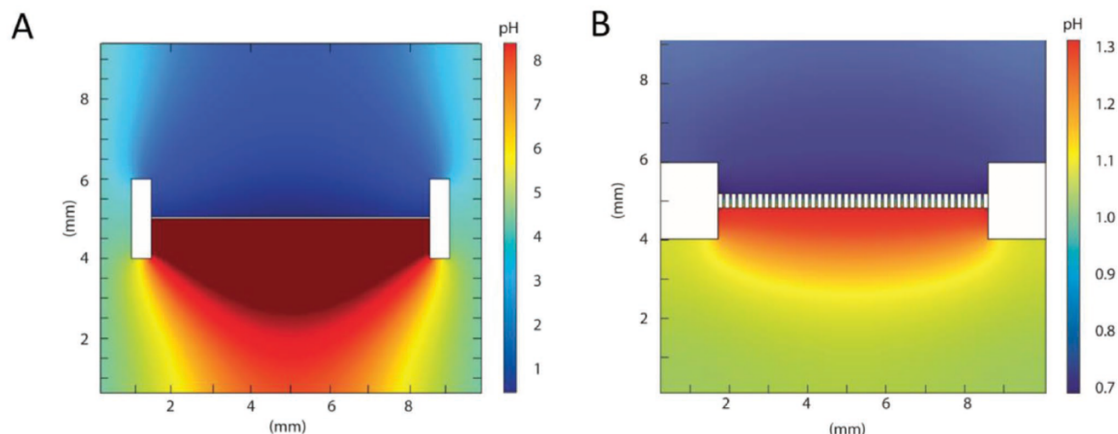


Figure 2.10: 2D COMSOL model of (A) a dense PV-EC cell and (B) a porous PV-EC cell [70].

Proton Exchange Material (PEM)

The pH gradient can be further suppressed by filling the pores with a Proton Exchange Material (PEM), such as Nafion[®], which would limit gas cross-over and enhance proton flow to the cathode. A PEM is a fluorinated polymer that conducts protons via its anionic functional groups, like, sulfonate SO_3^- . The anionic nature of the PEM results in a substantially higher diffusivity for H^+ compared to OH^- and O_2 inside the pores, thereby enhancing the proton flow, while minimizing the risk of generating the product gases in close proximity to one another. A PEM is more generally referred to as a Cation Exchange Membrane (CEM). Under basic conditions, an Anion Exchange Membrane (AEM) is implemented, since the conducted ion in that case is an anion (OH^-). Vijsselaar et al demonstrate the importance of including a PEM in the device by measuring the extent of hydrogen evolution in the anodic or O_2 compartment [70]. The stabilized cross-over percentage was reduced from 6% to < 0.1% when the PEM was incorporated, as shown in Figure 2.11 [70]. This is quite significant, considering that the lower flammability limit and explosive limit are 4% and 17% H_2 in the O_2 compartment, respectively.

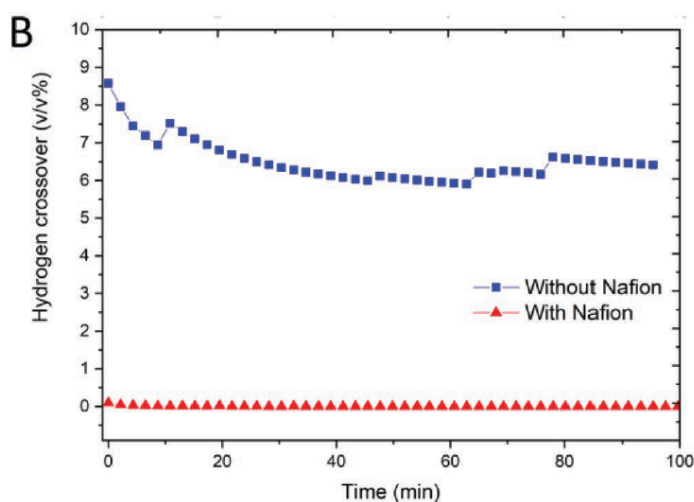


Figure 2.11: Hydrogen cross-over for PMP cell with and without Nafion[®] [70].

Electrode Coverage

The electrodes in a PMP cell serve two functions:

- **PV function:** Serving as the front and back contacts that enhance the transfer of charge carriers between the PMP cell and the electrolyte.
- **EC function:** Serving as the electrocatalysts that reduce the kinetic overpotentials for the water splitting process, thereby increasing the EC reaction rates, and thus the operational current density.

The photoactive layers of the PMP cell in this study are based on n-type semiconductors. The device thus has, by default, a photoanode configuration, placing the anode at the front side of the device. So, while the cathode coverage is only limited by the pore patterning, which was discussed in section 2.1.4, front contact coverage losses need to be considered as well. The latter will need to be optimized such that a balance between having sufficiently high light absorption and reasonably low ohmic losses is established.

The anode may be patterned into microdots, uniformly distributed across the top surface. Fortunately, an optimum for this configuration was determined at 5% coverage (Diameter = 5 μm ; Pitch = 8 μm), after accounting for PV and EC losses. This corresponds to a $\theta_c = 0.95$. It must be noted that the microdot optimization was done considering a fixed diameter of 5 μm . It is possible to further enhance the coverage geometry by investigating different diameters or shapes that could yield higher performance. However, the scope of this study is limited to the optimization of pore size and distribution. For that reason, the 5% anode microdot configuration is considered in this study.

Pore Size and Distribution

The pores, or microchannels, are the distinguishing factor between dense and porous monolithic PV-EC cells. Optimizing the pore size and distribution is thus mandatory for adequately evaluating the maximum possible performance gains from using the porous structure, as well as highlighting its main limitations.

The impact of pore size and distribution on PV performance is characterized by the losses in absorber area due to the porosity imposed by the holes, as well as the resistive losses associated with reduced back contact coverage. Vijsselaar et al found that after pore integration, 98.6% of the losses in the short circuit current density were due to porosity. However, the fill factor was also reduced by about 6.1%, which signals an increase in resistive losses. The J-V curves of the PMP cells before and after pore and microdot processing are presented in Figure 2.12 [70]. The PV performance of PMP cells can be evaluated using equations (2.14) – (2.16) and substituting θ_{overall} , as discussed in section 2.1.4.

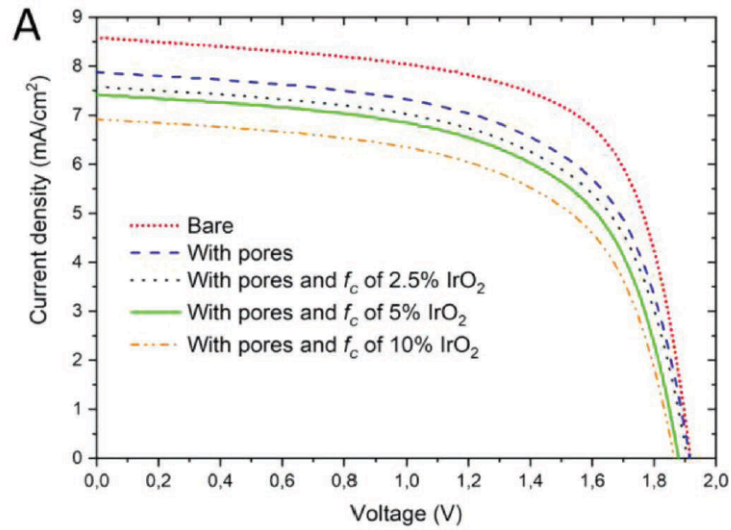


Figure 2.12: J-V characteristic for PMP cell: bare; with pores; with pores and anode microdot coverage of 2.5%, 5%, and 10%, respectively [70].

The influence of pore size and distribution on the EC performance, and more particularly on proton transport, is, however, more complex. Trompoukis et al simulated the effects of pore diameter, pitch, and depth on the EC performance of PMP cells, as demonstrated in Figure 2.13 [68]. They concluded that the EC performance improves as pore dimensions are decreased, which is reasonable, since smaller device features would lead to shorter ionic distances between the electrodes. This seems to suggest that the optimum pore size and distribution is limited by the manufacturing capability of the processing equipment, since smaller features are harder to produce.

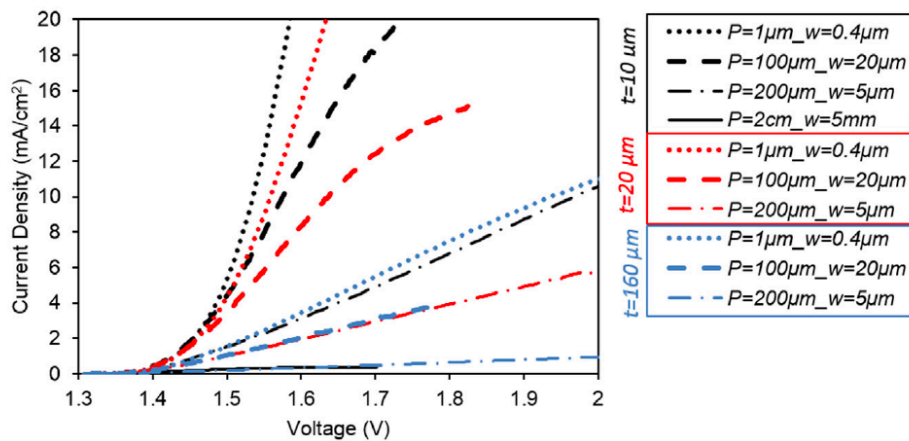


Figure 2.13: Effect of pore geometry on the current voltage characteristic of PMP cells [68].

To better understand how the inclusion of pores influences proton transport, and ultimately the EC performance, it helps to sub-divide the EC process into two transport steps:

1. Surface Proton Transport (SPT)
2. In-Pore Proton Transport (IPT)

In the EC context, the pore size and distribution are assumed to be exclusively associated with ionic transport losses, thus, all components, besides the electrolyte, are considered ideal.

Surface Proton Transport (SPT):

When a proton is generated at the anode, the first objective is for it to travel towards the nearest pore. Thus, in order to enhance surface transport, the spacing between the holes needs to be minimized.

Consider a small portion of a PMP cell consisting of four pores in Figure 2.14. B_p is the maximum distance a generated proton needs to travel before reaching the nearest hole. Consequently, enhancing SPT requires minimizing B_p . This quantity is determined geometrically as a function of the pore diameter D_p and pitch P_p :

$$B_p = \frac{1}{2}(\sqrt{2}P_p + D_p) \tag{2.45}$$

Though it is common practice to express the pore size and distribution in terms of the diameter and pitch, it can be argued that it is better to replace the pitch with B_p . Patterns having the same B_p , but different diameters experience ~ 3 times less change in the inter-array spacing $L_p = P_p - D_p$. Thus, keeping B_p constant allows for maintaining a more uniform hole spacing between patterns having different pore diameters. This should result in more comparable SPT between the patterns than when the pitch is kept constant. The significance of this is that the SPT and IPT effects can be more effectively decoupled, such that the individual impact of each transport step on the overall EC performance can be more accurately quantified.

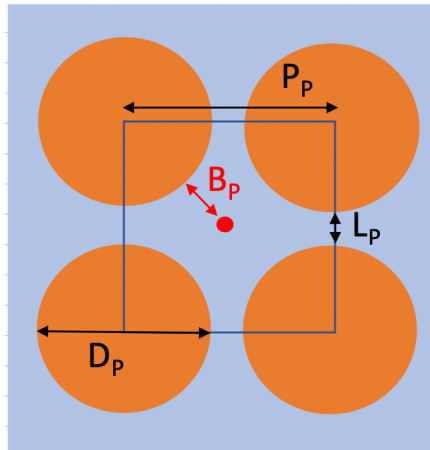


Figure 2.14: A PMP unit cell consisting of four pores. The red dot is farthest H^+ generation point to the nearest hole.

Though shorter ion-to-hole distances lead to a better EC performance, they also favour patterns that have higher porosity θ_p , which exhibit a lower PV performance. It is, thus, insufficient to consider the impact of B_p alone. It was demonstrated earlier that $B_p = f(D_p, P_p)$. θ_p can also be expressed as a function of D_p and P_p , meaning that for a given D_p/P_p combination, it is possible to determine the corresponding B_p and θ_p .

Consider a square array of side X with holes having a uniform pore size and distribution. The total area $A_T = X^2$, while A_p is the overall pore area, thus, θ_p can be expressed as:

$$\theta_p = \frac{A_p}{A_T} = \frac{N_p \pi D_p^2}{4X^2} \tag{2.46}$$

Every row or column of pores starts and ends at the corners of the square array. So, if n_p is the number of pores per row or column then the number of spaces between them is $(n_p - 1)$. X , can thus be defined as:

$$X = n_p D_p + (n_p - 1)L_p \quad (2.47)$$

Rearranging this equation and substituting $(P_p - D_p)$ for L_p , the number of pores per row or column becomes:

$$n_p = \frac{(X + P_p - D_p)}{P_p} \quad (2.48)$$

Therefore, the total number of pores in the entire square, $N_p = n_p^2 = f(D_p, P_p)$ and the porosity is:

$$\theta_p = \frac{\pi}{4X^2} \cdot (X + P_p - D_p)^2 \cdot \left(\frac{D_p}{P_p}\right)^2 \quad (2.49)$$

From the derived geometrical expressions relating D_p , P_p , B_p , and θ_p , one finds that at constant porosity (PV losses \sim constant), lower B_p values (enhanced SPT) are achieved for smaller D_p .

In-Pore Proton Transport (IPT):

After reaching the pore edge, the proton has to flow through the entire depth to reach the cathode. Thus, improving IPT requires thinner devices. However, since a PMP cell requires the exposure of both surfaces to the electrolyte, at least one of the layers in the device will have to be thick enough to dual as a support structure. Mechanical robustness is a crucial reliability factor and must be considered when optimizing pore depth. Thickness is not related to pore size and distribution and, therefore, requires separate optimization.

IPT is also influenced by the pore diameter D_p . Following from fluid dynamics, protons will flow in larger fluxes inside the pores if D_p is larger. It is also important to note that smaller diameters lead to more constricted proton flow inside the pores, which can present multiple problems. For one, the pressure build-up inside the holes could cause the side walls to crack, which would create defects in the device and, in the worst case, collapse the structure. Additionally, if the pores are too small, it might not be possible to fill them with Proton Exchange Material (PEM). Moreover, for a given thickness, smaller pore diameters have higher Aspect Ratios (AR), defined as the ratio of the pore depth to its diameter, especially in the case of thick devices, which may require more complex and expensive processing if very high resolutions are desired.

For pore size and distribution, the question becomes: Does SPT or IPT bear more effect on the EC performance, provided that the PV losses remain constant? Increasing the pore diameter appears favourable for IPT, while smaller diameters seem preferable for SPT, provided that the porosity is fixed.

The next Chapter covers the theoretical framework, developed in this thesis, to understand the influence of pore size and distribution on PMP cell performance taking into account the associated PV and EC losses covered in this Chapter.

3. Theoretical Methods

Following the discussion in Chapter 2, a theoretical approach is devised for quantifying the effect of pore size and distribution on the performance of PMP cells.

The **EC performance** is evaluated from the **pH gradient** that evolves between the anode and the cathode for different hole patterns. The pH at the surface of each electrode is obtained from 2D simulations of PMP cells in COMSOL Multiphysics® [96], based on the reference models from [69], [70]. The results are then used as input to evaluate the Butler-Volmer current density J_{BV} , which as described in section 2.2.2, represents the losses in the charge transfer current density due to pH gradient-related overpotentials.

The **PV performance** is evaluated from the **porosity** θ_p , which as was shown in section 2.4.1, can be calculated as a function of D_p and P_p for a given hole pattern. The effect of contact shading is neglected, since the geometry of the anode is not a variable in this study.

3.1. Modelling pH Gradients in PMP Cells

2D PMP cells of varying pore size and distribution are modelled in COMSOL Multiphysics®, using the Electrochemistry Module, specifically, the Tertiary Current Distribution (TCD) Nernst-Planck Interface.

3.1.1. Geometry

First, the desired geometries are constructed. Since the model is in 2D, the pores are modelled as slits. D_p is the pore diameter, P_p is the pitch, and h_p is the thickness or depth. All three parameters are expressed in microns (μm). An example is shown in Figure 3.1, considering $D_p/P_p = 40\mu\text{m}/150\mu\text{m}$. The electrolyte domain, in purple, is included in the TCD interface. The grey domain represents the porous device, which primarily serves as an obstructive medium for proton flow and is not involved in the simulation.

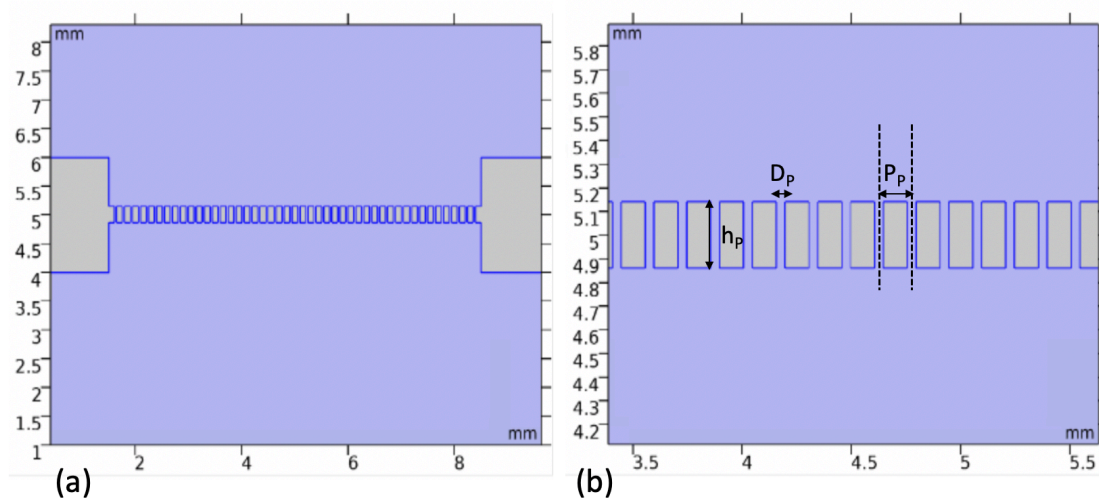


Figure 3.1: Geometry for $D_p/P_p = 40\mu\text{m}/150\mu\text{m}$ (a) full view; (b) close up.

3.1.2. Model Setup

The TCD interface models the current – voltage relations in an EC cell in terms of the molar fluxes of chemical species N_k in the electrolyte solution and is described by the Nernst-Planck Equation:

$$N_k = D_k \nabla c_k - z_k \mu_k F c_k \nabla \phi_l + c_k v \quad \text{For } k = 1, 2, 3, \dots, n \quad (3.1)$$

Where c_k is the concentration, D_k is the diffusion coefficient, z_k is the charge number, and $\mu_k = D_k/RT$ is the mobility of the k^{th} species. $\nabla \phi_l$ is the electrolyte potential, and v is the solution velocity. The first two terms on the right-hand-side represent the diffusion flux and electrically driven migration flux, respectively. The last term, $c_k v$, is the convective flux, which can be caused by bubble formation at the electrode surfaces during product gas evolution and is neglected in this study. The sum of the fluxes of all the charged species yields the electrolyte current density:

$$i_l = F \sum_{k=1}^n z_k N_k \quad (3.2)$$

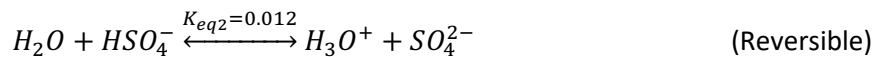
The Charge Conservation Model (CMM) selected for this simulation is the Supporting Electrolyte (SE) CCM, which allows for setting the electrolyte conductivity σ_l . By doing so, ohmic losses related to resistances in the electrolyte can be minimized and the potential difference across the device is localized at the electrode-electrolyte interfaces [89]. The electrolyte potential can thus be determined via Ohm's Law:

$$\nabla \phi_l = \sigma_l i_l \quad (3.3)$$

In this model, σ_l is set to 0.5 S/cm, as is the case in [70], while the initial electrolyte potential is set to 0 V.

Electrolyte

The electrolyte is a 0.1 M H_2SO_4 solution at a standard temperature of 25 °C. All relevant species in the bulk solution and their initial concentrations can be derived from the dissociation reactions of H_2SO_4 :



H_2SO_4 essentially undergoes complete dissociation, given the relatively large equilibrium constant K_{eq1} of 97.7. HSO_4^- dissociation, on the other hand, is slower and proceeds reversibly. The product gases are not considered in this model. The electrolyte parameters, namely the initial concentrations, diffusion coefficients, and charge numbers of the species are summarized in Table 3.1 [69] & [70].

Table 3-1: Electrolyte parameters for 0.1 M H_2SO_4 solution at T = 25 °C

Species	$c_{k,\text{initial}}$ [mol/L]	D [cm ² /s]	Z
H ⁺	1.24×10^{-1}	9.3×10^{-5}	1
OH ⁻	1.47×10^{-13}	5.3×10^{-5}	-1
H ₂ SO ₄	2.20×10^{-13}	1×10^{-5}	0
HSO ₄ ⁻	7.45×10^{-2}	1.31×10^{-5}	-1
SO ₄ ²⁻	2.49×10^{-2}	1.07×10^{-5}	-2
H ₂ O	5.52×10^1	2.01×10^{-5}	0

Electrodes

The electrodes are modelled as boundary layers held at a fixed $\Delta\phi_s$, with the anode (top) set at 1.229 V, while the cathode (bottom) is grounded at 0 V. The cathode and anode layers are assumed to be made of Platinum Pt and Ruthenium Oxide (RuO₂), respectively, given their high performance as electrocatalysts, and are parameterized based on literature values [69] & [70]. Moreover, an electrolyte current density is set as a boundary condition for the electrode surfaces arbitrarily. The value is chosen at 8.13 mA/cm². This value is representative of the average current densities achieved by Si-based multijunction solar cells in practice and corresponds to a 10% STH efficiency. Moreover, the same current density was used in [70], which would help in validating the model. The electrical behaviour of the electrodes is assumed ideal, wherein film resistance is neglected. The RedOx reaction kinetics are modelled for each electrode using the Butler-Volmer equation, namely (2.38) in section 2.2.2. Note that each electrode is parameterized with its own transfer coefficient α and exchange current density J_{exc} , denoted by subscript “a” for anode and subscript “c” for cathode. The equilibrium potentials of the RedOx process are matched with $\Delta\phi_s$, while the stoichiometric coefficients are based on the acidic water-splitting half-reactions discussed in Chapter 2. Table 3.2 summarizes the electrode kinetics input parameters [69] & [70].

Table 3-2: Electrode kinetics input parameters

Parameter	Description	Value
$J_{exc,OER}$	OER Exchange Current Density	1.48×10^{-8} [A/cm ²]
$\alpha_{a,OER}$	OER Anodic Transfer Coefficient	1.7 [-]
$\alpha_{c,OER}$	OER Cathodic Transfer Coefficient	0.1 [-]
$J_{exc,HER}$	HER Exchange Current Density	1.00×10^{-3} [A/cm ²]
$\alpha_{a,HER}$	HER Anodic Transfer Coefficient	1 [-]
$\alpha_{c,HER}$	HER Cathodic Transfer Coefficient	1 [-]
J_{Lim}	Limiting Photocurrent Density	20 [mA/cm ²]

Mesh and Simulation

The mesh was set to “finer” for all components in the model, since there was negligible difference in the results when using higher resolution meshes (extra fine and extremely fine), which increase the simulation time. The simulation is run using a standard time dependent study node (the other option being stationary) and is run over a 15-minute time interval in increments of 0.02 minutes.

For the purpose of validation, Figure 3.2 shows the simulation results for $D_p/P_p = 50\mu\text{m}/200\mu\text{m}$, which yield a pH gradient similar to the model implemented in [70], though it is about 0.1 pH units smaller. This is likely due to differences in the model parameters, namely the ionic species included in the model and their initial concentrations (Na⁺ ions are not included in this model), which seem to have some impact on the size of the pH gradient obtained. With that being said, all parameters are kept fixed in the model, with the exception of the hole patterns, to maintain consistency.

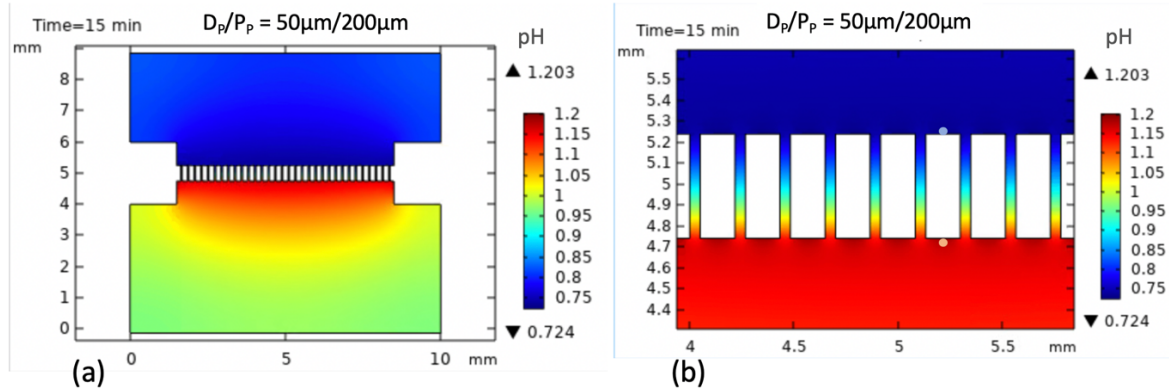


Figure 3.2: pH gradient simulation for $D_p/P_p = 50\mu\text{m}/200\mu\text{m}$ (a) full view; (b) close up. The blue and red dots correspond to the anode and cathode pH values, respectively.

Example: Evaluating PMP Cell Performance for $D_p/P_p = 50\mu\text{m}/200\mu\text{m}$

In this section, the $D_p/P_p = 50\mu\text{m}/200\mu\text{m}$ hole pattern will be used as an example for evaluating the performance of PMP cells in relation to pore size and distribution via this theoretical approach. The pH values at the anode and cathode surfaces, indicated by the blue and red dots, respectively, in Figure 3.3(b), are extracted from the data file of the simulation. The pH values can be converted into proton concentrations, which are then used to determine the electrode potentials from the Nernst equation. In this case, the pH level at the cathode and anode are 1.203 and 0.724, respectively, which following the derivation from (2.31) – (2.33), corresponds to an E_{Loss} of 28 mV,

E_{Loss} is then input into the Butler-Volmer equation (2.38) to find the BV current density at each electrode, considering the parameters in Table 3.2. The cathodic Butler-Volmer current density is found, in general, to be over 4 orders of magnitude larger than the anodic current density in this PV-EC system. The loss in ionic current is mainly represented by the failure of protons to reach the cathode, which would explain why these losses seem to be, essentially, only due to the cathodic process. Thus $J_{\text{BV}} = J_{\text{BV},c} - J_{\text{BV},a} \approx J_{\text{BV},c} = 2.7 \text{ mA/cm}^2$ for this pattern. So, considering a charge transfer current density $J_{\text{CT}} = 8.13 \text{ mA/cm}^2$, which happens to be a pre-set boundary condition for all simulations in this study, J_{pH} , the current density after accounting only for pH gradient losses is found to be 5.43 mA/cm^2 , as per (2.42). Furthermore, assuming 100% Faradaic efficiency, the STH efficiency, considering only EC losses related to pore size and distribution is 6.67%, as per (2.43).

The porosity for $D_p/P_p = 50\mu\text{m}/200\mu\text{m}$, considering a 1 cm^2 square array of pores is 4.9%, leaving 95.1% of the available active area for absorption. If the PV photocurrent density for the dense configuration is 8.13 mA/cm^2 then the current density after only accounting for porosity losses, defined here as J_0 , is equal to 7.72 mA/cm^2 , which corresponds to a 9.51% STH efficiency.

The overall current density J_{overall} , after accounting for both porosity and pH gradient losses, is obtained by multiplying the pore coverage factor $(1 - \theta_p)$ by J_{pH} , which yields a current density of 5.03 mA/cm^2 and an STH efficiency of 6.18%.

4. Experimental Methods

In this section, the methods and equipment used for processing and characterizing PMP cells are described. The fabrication process is carried out in the Else Kooi Laboratory (EKL) and Kavli cleanrooms (CR's) at TU Delft. The process is divided into three parts:

1. Silicon Heterojunction (SHJ) Processing
2. Electrode Deposition
3. Pore Processing and PEM In-filling

The pore processing step will be discussed in two sections, one considering the Deep Reactive Ion Etching method and the other in relation to the Pulsed Laser Drilling approach.

4.1. Silicon Hetero-Junction (SHJ) Processing

The role of the PV component in a PMP cell is to generate the required photovoltage to drive the water splitting half reactions. In this study, the PV cell is a Silicon Hetero-Junction (SHJ).

4.1.1. Si Wafer Cleaning and Preparation

First, Topsil Float Zone, $280 \pm 20 \mu\text{m}$ n-type Si wafers are then cleaned to remove organic and metallic surface impurities via the following cleaning sequence:

1. 10-minute soak in 99% fuming Nitric Acid (HNO_3) bath at 25°C
2. 10-minute soak in 69% fuming Nitric Acid (HNO_3) bath at 110°C
3. 4-minute soak in 0.55% Hydrogen Fluoride (HF) at 25°C

After each step, the wafer is rinsed and dried in deionized (DI) water until the water pH is neutral. The HNO_3 cleaning steps oxidize both surfaces of the wafer, trapping impurities in the oxide layers that form. The HF bath strips the oxide layer, leaving a clean unoxidized Si surface ready for processing. The final HF step takes place in a Marangoni drying setup, wherein after rinsing in DI water, the wafers are drawn out of the bath with Isopropanol (IPA) spray to ensure no water droplets remain on the surface.

In order to improve light in-coupling in the solar cell, the wafer surfaces are textured with smooth pyramidal structures. In addition to the conventional TMAH etching step, an acid etch is performed:

1. 15 minute etch in a 25:3:100 TMAH (25%): ALKA-TEX.8 (ISRA): H_2O solution at 85°C
2. 5 minute etch in a 1:6:3 HF (40%): HNO_3 (69%): H_2O solution at 25°C

The wafer is rinsed for 3 minutes in DI water after each step. After etching, the wafer is cleaned again, using the abovementioned sequence, prior to PECVD processing.

4.1.2. Plasma Enhanced Chemical Vapor Deposition (PECVD)

All the thin film silicon layers are deposited using a Plasma Enhanced Chemical Vapor Deposition (PECVD) multi-chamber system, wherein precursor gases breakdown into ions and radicals that get

deposited onto the substrate. Figure 4.1 illustrates a typical PECVD chamber [18]. The process involves the gas phase chemical reactions of precursor gases, such as Silane (SiH_4), Hydrogen (H_2), Phosphine (PH_3), and Diborane (B_2H_6) at relatively low processing temperatures (200 – 400 °C) in a plasma, with chamber pressures on the order of 0.5 – 5 mbars. Since some of the thin film layers in the device are based on silicon oxide, CO_2 gas is used as an oxygen source during their deposition. In this work, PECVD is performed using an Elettrorava Radio Frequency (RF)-PECVD cluster tool in EKL, also known as AMIGO.

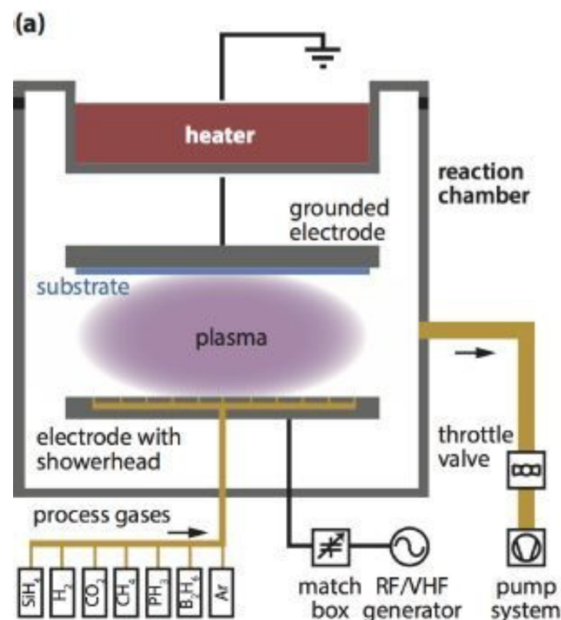


Figure 4.1: Plasma Enhance Chemical Vapor Deposition (PECVD) setup illustration [18].

As the name suggests, a plasma is ignited in the chamber by applying an RF potential between two parallel electrodes, one of which harbors the substrate. The gases in the chamber are ionized via the electric field that develops between the electrodes, generating reactive species at relatively low temperatures and pressures. Deposition ensues as gaseous ions get accelerated towards the substrate. The main parameters influencing the properties of the deposited thin films are the RF power, gas flow rates, chamber pressure, temperature, and deposition time. The parameters for processing the SHJ's used in this study are summarized in Table A1, from the Appendix A.

4.1.3. Transparent Conductive Oxide (TCO) Deposition

The conduction of charge carriers between the photoactive surfaces and the metal contacts is enhanced by implementing Transparent Conductive Oxide (TCO) layers between them. The thickness of the TCO layers on either side can be optimized further for enhanced light trapping in the SHJ, thus serving as an Anti-Reflective Coating (ARC) at the front, and a light reflector at the back. The TCO thickness was optimized by other members in the group for each side, with the front side thickness = 75 nm, while the backside thickness = 150 nm. The TCO used in this application is Indium Tin Oxide (ITO) and is deposited via RF Magnetron Sputtering, which is illustrated in Figure 4.2 [97].

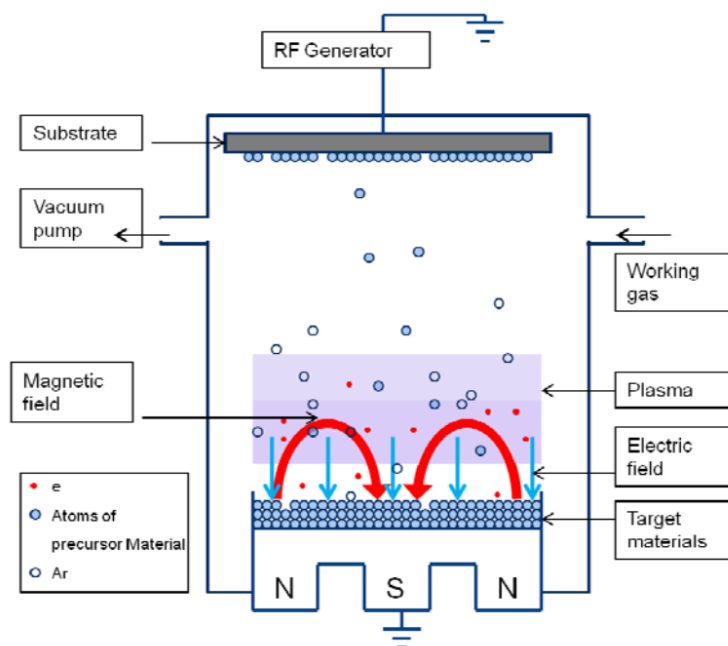


Figure 4.2: RF Magnetron Sputtering process [97].

The sputtering process involves the bombardment of a target material with an energetic beam of ions in a vacuum chamber. Upon bombardment, the sputtered compounds are accelerated towards the substrate for deposition, driven by the potential difference between the substrate and the target. The gas is, typically, Argon, Nitrogen, or Oxygen, the latter particularly required for reactive sputtering processes, while the former two are inert and perform only physical bombardment. A plasma is also generated in this process via a parallel electrode configuration. Magnets are incorporated in the setup to direct the ion beam towards the target and away from the substrate, situated opposite to it.

The RF Magnetron Sputtering tool used in this work is a Cryofox Polytechnik AS cluster tool and the target consists of 10% Tin Oxide (SnO_2) and 90% Indium Oxide (In_2O_3). The main influencing parameters are the source power, chamber temperature and pressure, as well as the deposition time. Table A2 from Appendix A summarizes the ITO sputter deposition parameters. The unit PMP cells are electrically isolated by patterning the ITO on the front side into equally sized separate squares using a metallic mask.

4.1.4. Si Stacks Used in PMP Cell Experiments

A complete Si-based PMP device would consist of a textured triple junction solar cell, based on an SHJ bottom cell, with two thin film junctions based on a-Si:H and nc-Si:H deposited on top of it. The SHJ consists of the Si wafer itself, so it duals as a physical support structure as well. The PVMD group at TU Delft recently developed a Si PV triple junction, based on this configuration, with a record efficiency of 13.6% ref. The J-V characteristic of this device will be considered for overall STH performance evaluation in this study.

The fabrication of the entire triple junction Si stack, however, takes a long time. Therefore, SHJ's without the additional thin film junctions were fabricated for analyzing the PV performance dependence on pore size and distribution. Evaluating the EC performance as a function of hole patterning does not require a PV junction. Thus, for J-E measurements, the Si stack is just a bare n-type Si wafer, without the thin film Si layers.

4.2. Electrode Deposition

The contacts in this device need to be electrochemically active, otherwise they cannot catalyse the EC half-cell reactions. In this work, Pt is used as both the cathode and anode material, owing to its suitable electrical and electrocatalytic properties. Additionally, an Aluminium (Al) metal grid is deposited on the top surface around the borders of the PMP cells for front side contacting during J-V and J-E characterization.

4.2.1. Electron Beam Evaporation

Both the Pt and Al are deposited via Electron Beam Evaporation, which is a Physical Vapor Deposition (PVD) process, as illustrated in Figure 4.3 [98]. This technique is similar to sputtering in the sense that a beam of particles is accelerated towards the deposition material, but instead of ions, electrons generated from a Tungsten filament are used. Also, the material is loaded as pellets into a crucible in place of a target. The pellets are heated into a melt and then evaporated onto the substrates, which are loaded at the top of the chamber onto a dome. The dome rotates during deposition at around 20 Rounds Per Minute (RPM) to promote uniform deposition. The electron beam source power, chamber pressure, desired thickness, and deposition rate are the key factors influencing this process, wherein the deposition time is defined by the latter two parameters.

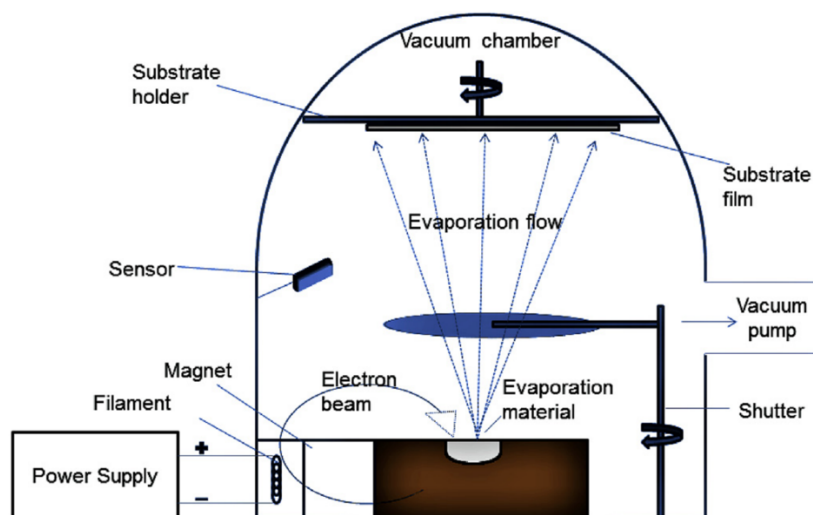


Figure 4.3: Electron Beam Evaporator illustration [98].

Though the process is the same for both Pt and Al, they are deposited via two different machines, the CHA Solutions process development system and PROVAC Pro 500S, respectively. The Pt layer is 75 nm, deposited at a rate of 3 Å/s, whereas the Al grid is 500 nm thick, and deposited at a rate of 20 Å/s.

As earlier mentioned, the anode side needs to be patterned to allow for sufficient light penetration into the solar cell. However, due to the geometry of the substrate holders in the CHA Solutions evaporator, Pt patterning is not practical to implement with a metallic mask. Additionally, there is a high-resolution requirement, with feature sizes on the order of a few microns, which are difficult to achieve for such masks, that have minimum resolution of about 5 μm. Therefore, the wafer is patterned via photolithography, which has a minimum resolution of about 10 nm, prior to Pt deposition. A 5% coverage anode microdot pattern similar to the one used in [70] is implemented in this work. The Al metal grids can be patterned in PROVAC by attaching the wafer onto a metallic mask, given the larger feature sizes. Therefore, the Al deposition step does not require photolithography.

There is another concern that was not considered in previous works, which may lead to further issues in charge collection, especially for thinner devices. Typically, the cathode, or back contact, is deposited

with full, thus, the holes are etched or drilled through the metallic contact. The sputtered Pt particles at the surface may risk getting lodged into the pores, which could make them conductive and introduces shunting paths in the device near the pores. Hypothetically, this issue would be more aggravated for thinner devices, since Pt particles need to travel shorter distances to reach the photoactive part of the device. Moreover, in [70], the anode microdots were not patterned around the hole positions and were deposited after the pores were formed, which further risks introducing metal particles into the holes. The device in [70] experienced a decrease in fill factor from 0.66 to 0.62 after pore processing, which leads to two questions: will patterning both electrodes around the hole positions and depositing them before processing the pores improve the electrical properties of the device? If so, how does this effect scale with device thickness?

Originally, different wafer thicknesses (100 – 300 μm) were going to be included in the analysis. However, due to delays associated with the pandemic situation and equipment being down, there was not enough time to process and analyze the wafer thickness series.

4.2.2. Photolithography

Photolithography is a high-resolution patterning technique that involves four steps:

1. Coating the wafer with photosensitive masking material called photoresist
2. Exposure of the photoresist with an optical or UV light source to decompose or polymerize it
3. Development of the photoresist to remove the undesired areas and obtain the pattern
4. Post deposition/etch photoresist removal "Lift-off"

The photolithographic process is summarized in Figure 4.4 [99]. There are two types of photoresist, positive and negative. The positive photoresist is a polymer that decomposes upon light exposure. The depolymerization weakens the adhesion of the exposed areas to the substrate, such that upon development, the exposed region is removed. A negative photoresist works oppositely. It is a compound that polymerizes upon light absorption, bonding more strongly to the substrate, such that upon development, the unexposed areas get removed.

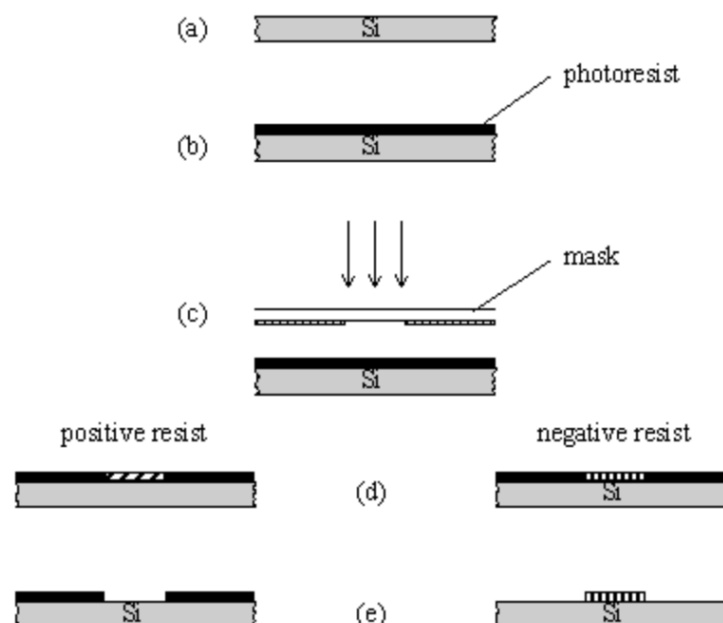


Figure 4.4: Photolithography process: (a) \rightarrow (b) Coating; (b) \rightarrow (d) Exposure; (d) \rightarrow (e) Development [99].

In this work, photolithography is done in the cleanroom 100 (CR100) section of EKL. The 100 corresponds to the number of particles present within a cubic meter of space, with diameter $> 0.5 \mu\text{m}$. The other processes, besides PLD, namely, Si PV stack deposition, electrode deposition and DRIE, are done in the CR10000 part of the lab.

Coating

First, the wafers are treated in Hexamethyl Disilazane (HMDS) vapor for 15 minutes to enhance adhesion of the photoresist layer to the wafer. For Pt deposition, both the cathode and anode are patterned with a negative photoresist, Nlof2020, using a standard procedure. A $3.5 \mu\text{m}$ layer of photoresist is spin-coated on a Brewer Science manual spinner at 1067 RPM for 60 seconds then baked indirectly on a hotplate at $115 \text{ }^\circ\text{C}$ for 90 seconds, using a carrier wafer to avoid scratching the opposite side.

Exposure

The exposure step requires the use of a photomask to define the exposed regions. Two sets of photomasks were designed, using L-Edit software, for the cathode and anode, accounting for the hole positions. Figure 4.5 shows the photomask patterns for the anode and cathode, respectively. As noted in Chapter 1, the experimental data set consists of eight hole patterns, which can be divided equally between two wafers. Each quadrant consists of 6 cells all having the same D_p/P_p ratio, and 2 control cells. The anode control pattern is just a uniform distribution of microdots, without accounting for hole positions, while the cathode control is full coverage.

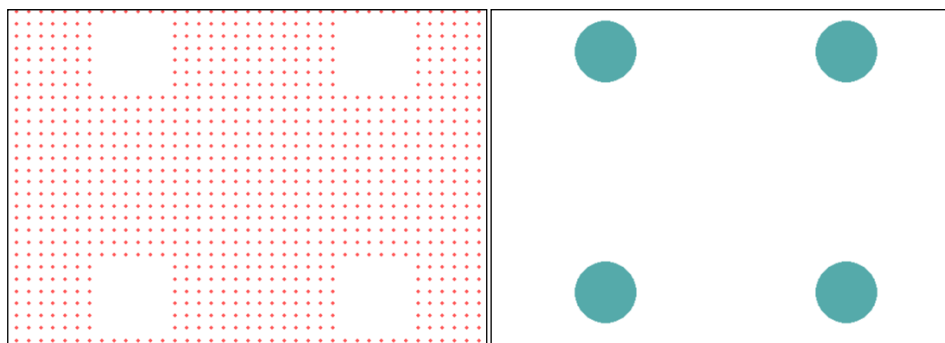


Figure 4.5: Photomask pattern designs: (Left) Anode microdot mask; (Right) Cathode hole mask.

Exposure is done using a SUSS MA8 Contact Aligner, with an energy of 220 mJ/cm^2 , determined as the product of the light intensity = 11 mW/cm^2 and exposure time = 20 seconds. The minimum energy requirement is 150 mJ/cm^2 , but the additional energy ensures that the photoresist is well exposed, which is crucial for getting a clean etch. The cathode is patterned first, using a Front Side Alignment (FSA) recipe, wherein the alignment markers of the photomask and wafer are matched via live microscopy. Back Side Alignment (BSA) is done for the anode to ensure that both sides are well aligned. Unfortunately, with this instrument, BSA is done by using a still rather than a live image, so any shifting prior to exposure cannot be detected and accounted for. Thus, perfect front to back alignment is challenging to achieve.

Development

After exposure, a post-bake step is done on the hotplate, again using a carrier wafer, at $115 \text{ }^\circ\text{C}$ for 60 seconds prior to development. This step is crucial to strengthen the adhesion of the exposed areas, otherwise the entire coating is removed. Development is done in pure MF322 developer in a puddle process for 2 minutes and 30 seconds until the pattern is visibly developed, as shown in Figure 4.6 for the $D_p/P_p = 20\mu\text{m}/80\mu\text{m}$ pattern.

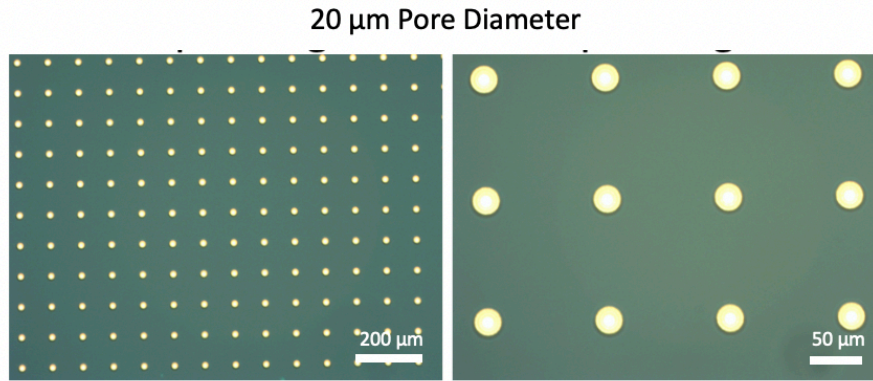


Figure 4.6: Photoresist patterning of 20 μm holes with a pitch of 80 μm on the cathode side.

NMP Photoresist Lift-Off

After Pt deposition in the evaporator, the photoresist is removed by sonicating in N-Methyl-2-pyrrolidone (NMP) solution at 75 $^{\circ}\text{C}$ for 20 minutes, followed by a DI water rinse and spin drying. This process is referred to as Lift-off and is the final step before the desired pattern is revealed, as shown in Figure 4.7.

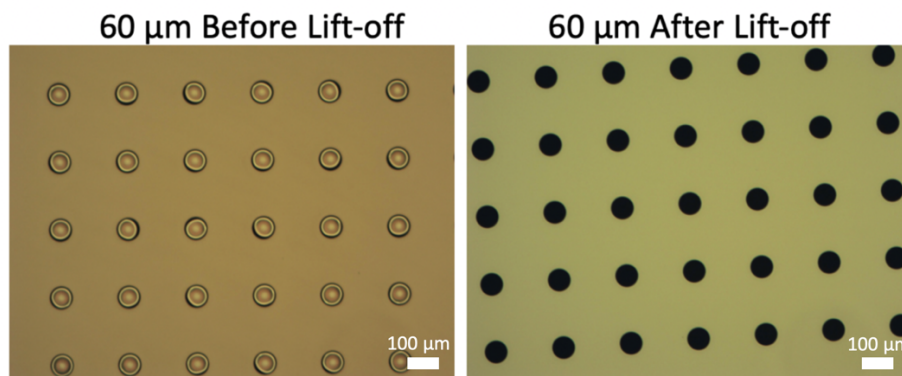


Figure 4.7: 60 μm holes after Pt deposition: (Left) Before lift-off; (Right) After lift-off.

Though the cathode side deposition proved to be consistently successful, following the standard recipe, the anode microdot deposition was not. It appears that the photoresist is not properly developing, so the wafer surface is not properly exposed for Pt deposition. This is one of the main issues as to why complete PMP cells could not be processed.

4.3. Pore Processing Methods

This section describes the pore processing methods used in this study, namely, Deep Reactive Ion Etching (DRIE) and Pulsed or Percussive Laser Drilling (PLD).

4.3.1. Deep Reactive Ion Etching (DRIE)

DRIE is an etching process that involves the ionization and radical formation of fluorine-based etchant and passivation gases in a high-density plasma. The plasma is typically generated via inductive coupling, and hence is defined as an Inductively Coupled Plasma. A potential bias is also applied between the plasma and the substrate, normally by a separate parallel-plate or Capacitively Coupled Plasma system, that drives ions and free radicals towards the substrate surface. Therefore, in addition to chemical etching, the DRIE process also involves physical ion bombardment. In order to etch a pattern,

a mask (hard = Silicon Oxide / soft = photoresist) is applied on the wafer prior to etching. The mask materials are etched at a much slower rate than the substrate and are assessed by their *selectivity*, which is defined as the ratio of the substrate etch rate to the mask etch rate, which can be as high as 300:1. The mask is removed post-process via Oxygen etch cleaning or sonicating in a suitable lift-off reagent in the case of photoresist.

The significance of this method is its anisotropic etching ability. The process can attain deep and vertical pores, with almost no taper, even for relatively small diameters < 10 μm. This attribute is represented by the Aspect Ratio (AR), a useful property for evaluating the etching or drilling quality of a given process. In the case of pores, it is the ratio of the hole depth to its diameter h_p/D_p .

Bosch Versus Cryogenic DRIE Process

The standard etchant gas is Sulfur Hexafluoride (SF_6). The etchant dissociates into Fluorine-based free radicals in the plasma that react with Si surface atoms and remove them in the form of Silicon Fluoride (SiF_x) gas. Oxygen can also be used as a supporting etchant. The choice of passivation gas depends on the DRIE process followed. The two types of DRIE processes are the **Bosch "Pulsed" Process** and the **Cryogenic Process**, illustrated in Figure 4.8(a) and (b), respectively.

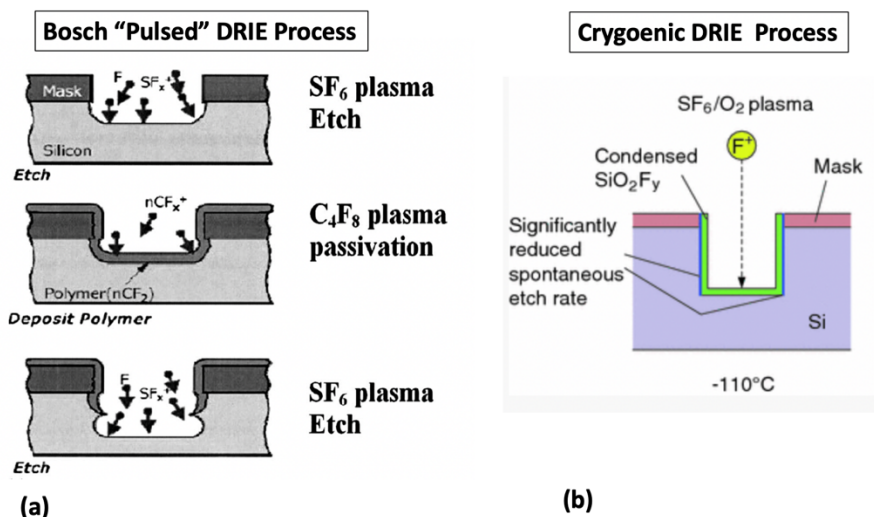


Figure 4.8: Illustration of the (a) Bosch "Pulsed" DRIE process [100]; (b) Cryogenic DRIE process [101].

The Bosch method involves cycling between a sequence of alternating steps of etching with SF_6 and passivation with C_4F_8 . The fluorocarbon passivation gas breaks down into long chain CF_x radicals that form a protective coating on the sidewalls and bottom of the pore. The vertical ion bombardment in the etching step removes the bottom layer before etching further into the material. The duration of each step, number of cycles, flow rates of the gases, chuck temperature, as well as the source and bias power need to be well tuned to achieve high aspect ratios and well passivated sidewalls. The Cryogenic method follows a similar process, except that the etching and passivation can occur at the same time. Passivation involves the formation of a thin Fluoride/Oxide blocking layer, which is resilient to etching at cryogenic temperatures (as low as - 110 °C). This process also utilizes low gas flow rates relative to the Bosch process.

The Bosch process yields feature sizes on the order of tens of microns and depths of hundreds of microns. It has the advantage of attaining high etch rates of around 10 – 20 μm/minute, compared to < 3 μm/minute for the cryogenic process, while still maintaining good morphology. This is mainly attributed to the sequential cycling, which allows for using high gas flow rates. Moreover, the

fluorocarbon polymer is easier to etch through, relative to the oxide employed in the Cryogenic method. For this reason, selectivity is, generally, higher for the Bosch process. However, the cycling also leads to sidewall roughness, due to scalloping. The Cryogenic method is signified by its higher resolution, with nm-size features and depths of a few microns. Furthermore, scalloping does not occur in this method, which results in smoother sidewalls.

The etchers at EKL and Kavli are the Adixon AMS110 and AMS100, respectively, are both based on the Bosch process, which, conveniently, is more compatible with the required dimensions for this study.

PMP Cell DRIE Process

The PMP cell DRIE approach consists of the following steps:

1. Etch Mask Photolithography
2. Carrier Wafer Binding
3. DRIE Pore Processing
4. Post-Process O₂ Plasma Clean
5. Carrier Wafer Unbinding
6. NMP Lift-off of Photoresist

A 16 – 18 μm masking layer of positive photoresist (AZ10XT) is spin coated at 1000 RPM for 30 seconds. The layer is baked on a hotplate, using a carrier wafer, at 115 °C for 4 minutes, then left to rehydrate for 30 minutes before exposure. The cathode side (hole) mask is used during the exposure step, but in this case, the exposed area will get developed. Thus, with good alignment, the hole positions and patterned Pt back contact will, essentially, have no overlap. Afterwards, the photoresist is developed in a 1:4 AZ400K:DI water puddle process for 10 minutes then rinsed with DI water and dried on the spinner. Next, the uncoated side of the wafer is bound with two small drops of Fomblin oil to a 500 μm Si wafer coated with a 5 μm Silicon Oxide layer via wet thermal oxidation at 700 °C for 15 hours. This serves as a blocking layer that prevents exposing the chuck to the process gasses.

The etching recipe was adapted from [90] and served as a starting point for the optimization process, the parameters of which are summarized in Table A3 of Appendix A. The unmodified recipe was tested using the AMS110 in EKL. It was found that all pore diameters (20 – 80 μm) penetrate the entire depth after etching for a total of 6 hr and 30 minutes, pausing every hour to rest the wafer. A standard O₂ plasma clean recipe was applied afterwards at a flow rate of 200 sccm (standard cubic centimetre per minute) for 30 minutes.

The wafer is then unbound from the carrier using little force and cleaned via NMP lift-off, as discussed in the previous section.

DRIE processing based on the latest parameters results in damage to the anode (bottom) side of the wafer, as well over-etching near the entrance holes. This is possibly due to the very long etch time, which also hindered the pore processing throughput to one wafer per day. DRIE etch rates could reach up to 20 μm/minutes, while maintaining good morphology, whereas in this case, it was limited to around 1 μm/minute, which suggest that further optimization is required.

4.3.2. Pulsed Laser Drilling (PLD)

In PLD, ultra-fast laser pulses are incident onto the substrate, thereby melting and expelling the material in its path. As more energy is input, more molten matter is recoiled out onto the surface. Moreover, the area around the pore openings become more damaged. Pulsing the laser allows for controlling the input energy and substrate heating to minimize such effects. The laser pulse energy is determined from the intensity and the pulse duration, which is typically in the femtosecond –

nanosecond time scale. Either the laser or the stage is scanned in the XY plane to map out the pattern. Pulses are sent at a fixed frequency at each hole in sync with the scanning motion, hence “percussive”. Unlike DRIE, photolithography is not required, given the XY scanning capability, so fewer processing steps are needed. However, a Thermal Conductive Barrier (TCB) coating may be applied to avoid damaging the device surfaces. Moreover, PLD does not require vacuum conditions.

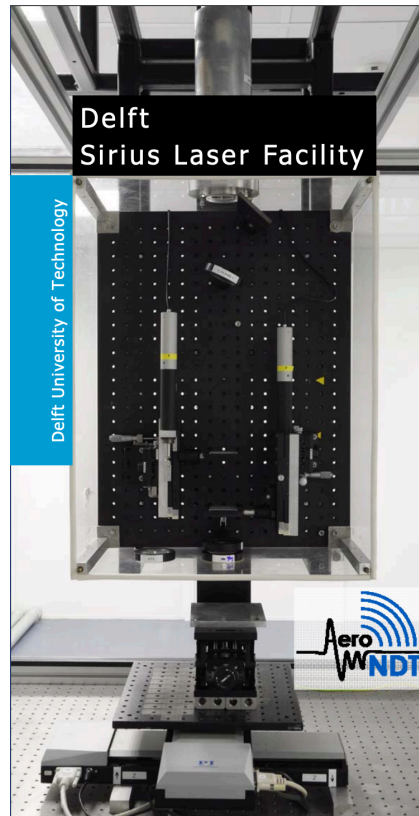


Figure 4.9: Pulsed laser drilling setup [102].

All laser drilling experiments were carried out at the Sirius Laser Facility in the Aerospace Engineering department of TU Delft. Figure 4.9 shows an image of the laser at the facility [102]. The laser has a wavelength of 300 nm and a maximum intensity of 1000 W/cm^2 . The pulse width is fixed at 200 nanoseconds, but the pulse energy can be incrementally attenuated via filters. A PI programmable XY stage is used to map out the hole patterns. The L-Edit file used for the cathode hole photomasks can be used to program the stage mapping trajectory, so that both DRIE and PLD devices have consistent configurations. A substrate holder was made to prevent the substrate from touching the stage and maintain stability. Also, $12\mu\text{m}$ thick AZ12XT layers deposited at 2000 RPM for 60 seconds and baked at $115 \text{ }^\circ\text{C}$ for 3 minutes, were used as TCB coatings.

Rough edges, either from DRIE or PLD, can be smoothed via etching in a solution consisting of a carefully balanced ratio of water (H_2O), Nitric Acid (HNO_3) and Hydrogen Fluoride (HF). Figure 4.10 shows an example of a laser drilled holes before and after etching in a 15:9:2 40% HF:69.5% HNO_3 : H_2O solution for 40 seconds [103].

In this study, the PMP cells are treated in a polyetch solution for 2 minutes then rinsed and dried. The composition used was:

1. 10mL of H_2O
2. 350 mL of 69.5% HNO_3
3. 140 mL 40% HF

Unfortunately, the pores were not imaged post the polyetch treatment.

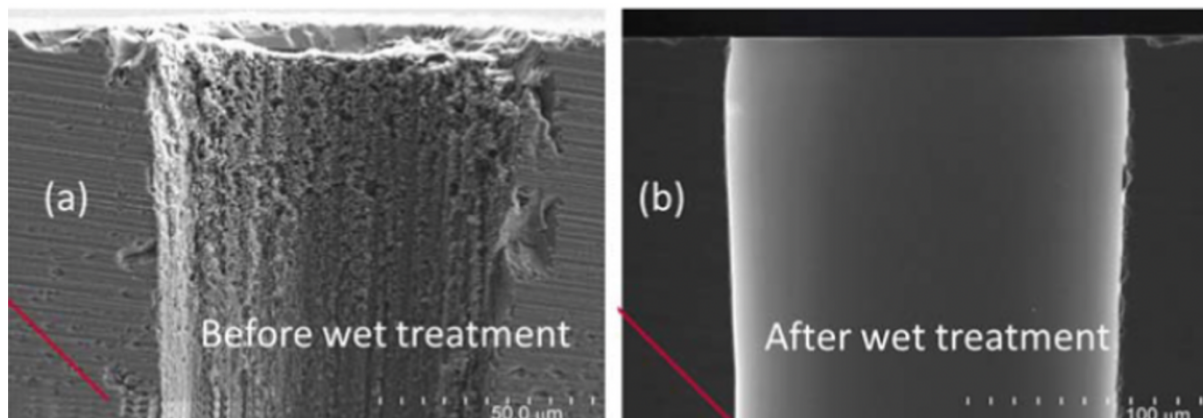


Figure 4.10: SEM's of PLD processed pores before and after treatment with 15:9:2 40%HF:69.5%HNO₃:H₂O etchant solution [103].

4.4. Nafion[®] PEM In-Filling

The final step in the fabrication process is the in-filling of the pores with PEM. 10 mL of 20% by weight Nafion[®] solution is mixed with 10 mL of Dimethylformamide (DMF) then evaporated in a rotovap at 10⁻³ mbar and 80 °C to remove the water content and small chain aliphatic alcohols from the mixture. Using a micropipette, a 100 μL of solution is dropcast at the cathode side then baked on a hotplate at 60 °C for 60 seconds to evaporate the solvent. With a razor blade, the Nafion[®] coating is scraped off leaving PEM only inside the pores [70].

4.5. PV Performance Characterization

In order to accurately assess the PV performance of the PMP cells, there are two types of measurements that need to be carried out, namely Current-Voltage (J-V) measurements and External Quantum Efficiency (EQE).

4.5.1. J-V Measurements

J-V measurements were done using a Wacom AAA solar simulator, from which the PV parameters covered in section 2.1.2 are obtained. The J-V measurements are done under Standard Testing Conditions (STC): AM1.5 spectrum at 1000 W/m² irradiance (one Sun illumination) and 25 °C. The spectral range is supplied by a combination of two lamps, Xenon (350 – 600 nm) and Halogen (600 – 1500 nm). The instrument is calibrated with two Silicon reference cells prior to measurements. The potential is automatically swept by varying the load resistance in the potentiostat as the cell is being illuminated. The cell is contacted at the front and back via two magnetic contact probes. The measurement is started after defining the cell area = 1 cm² and specifying the voltage range (-1.5 – 1.5 V).

The sample in this case is a full wafer with 32 test cells. Each cell is measured individually, with the anode as the illuminated side, while the other cells are blocked with black cardboard pieces.

4.5.2. External Quantum Efficiency (EQE)

As discussed in section 2.1.3, the EQE is also a crucial PV parameter, which indicates the efficacy of converting absorbed photons into generated, separated, and collected electron-hole pairs and allows for more accurately evaluating the short circuit current density compared to J-V characterization.

EQE measurements are conducted via an in-house setup at TU Delft. The AM1.5 spectrum is produced by a Xe lamp and a monochromator. The short circuit current is measured at each wavelength in the range (300 – 1200 nm) in increments of 10 nm for the SHJ samples then integrated over the wavelength range to obtain the overall Jsc. Prior to measurements, the setup is calibrated with a Si photodiode.

4.6. EC Performance Characterization

The EC performance can be measured via J-E characterization. Wires are soldered or glued onto the front and back contact of the PMP cell, serving as connection points to the potentiostat. The cell is then placed in a reactor chamber and contacted with the electrolyte by pressing the cell against an O-ring to form a water-tight seal, shielding the other electrode from the electrolyte. This does pose a challenge for porous devices, as the electrolyte can leach right through the pores. However, it seems that issue was somehow overcome in [70], where the pores were filled with proton exchange material. This approach does not allow for evaluating the device performance as a whole. Instead, each electrode is individually characterized.

PMP cells can be measured in a photocathode or photoanode configuration, since all three components are integrated. However, the anode has to always be at the illuminated side, given the device configuration adapted in this study. The J-E measurements are carried out in a 3-electrode system, wherein only one of the electrodes is measured. The Working Electrode (WE) is the electrode that is not being measured. In the photoanode configuration, for example, the cathode is connected as the Working Electrode (WE), with only the anode in contact with the electrolyte, while the opposite is true for the photocathode configuration. The other two electrodes are the Counter Electrode (CE) and the Reference Electrode (RE). Figure 4.11 illustrates the photocathode configuration for a PMP cell [70]. The J-E characteristic is obtained from cyclic voltammetry measurements versus a Reverse Hydrogen Electrode (RHE).

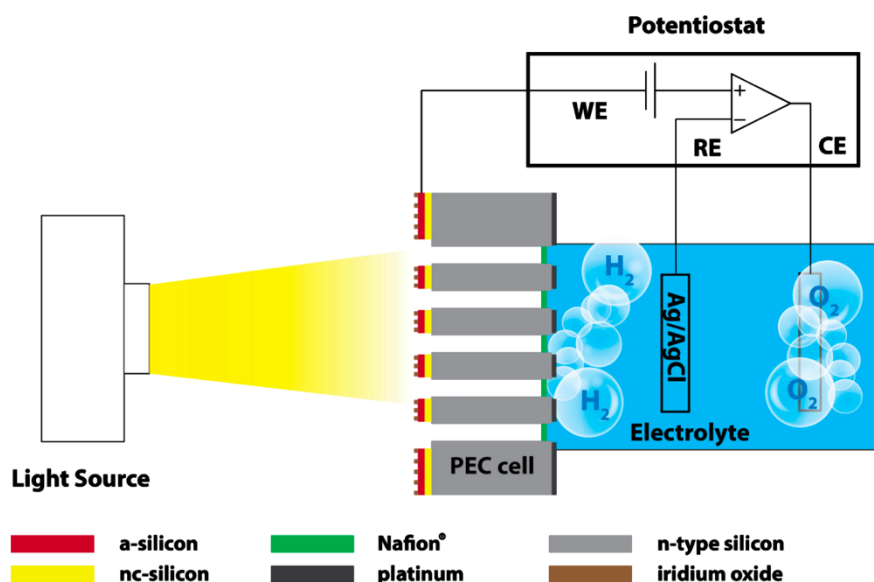


Figure 4.11: J-E measurement setup for a PMP cell in the photocathode configuration. The cathode is exposed to the electrolyte, while the anode is at the illuminated side outside the solution and connected as the working electrode. A counter electrode and reference electrode are included to complete the 3-electrode configuration [70].

Alternatively, the EC performance can be evaluated by measuring the hydrogen generation rate. This method is convenient for assessing the overall performance of a complete PMP cell, wherein the

device is immersed in a reactor chamber with electrolyte, without electrical connection. The chamber is fitted with a gas line to a Gas Chromatography instrument to measure the hydrogen generation rate, which is used to calculate the STH efficiency using (2.2.1) from section 2.2.1. The device thus operates in its intended stand-alone wireless configuration.

Due to time constraints, the PMP cell processing procedure was not fully developed in time to process complete devices for J-E measurements and hydrogen gas detection.

The operation of PMP cells was, however, qualitatively demonstrated. This experiment does not require a photoactive component, so the cells are based on bare n-type c-Si rather than SHJs. The device is wired and connected to a potentiostat then submerged in electrolyte. A potential is applied between the electrodes to drive the water splitting reaction, which is observed in the form of hydrogen and oxygen gas bubbles forming in the electrolyte.

5. Pore Size & Distribution Optimization

In this Chapter, the results of the theoretical pore size and distribution optimization study are described.

5.1. Theoretical Results

For the theoretical analysis, a 4x4 matrix of D_p/P_p combinations is evaluated based on pore-related current density losses:

1. When only porosity losses are considered $\rightarrow J_q$
2. When only pH gradient losses are considered $\rightarrow J_{pH}$
3. When both losses are considered $\rightarrow J_{overall}$

Thus, three 4x4 matrices are assembled to map out the performance of a range of (D_p/P_p) combination in terms of current density in the form of contour plots. The D_p and P_p arrays used are:

$$D_p = [20 \ 40 \ 60 \ 80]$$

$$P_p = [100 \ 150 \ 200 \ 250]$$

The current density values are all normalized to the pre-defined operational current density J_{OP} (when no losses are considered), which is set in this study to **8.13 mA/cm²** and corresponds to an STH efficiency of 10%. This value was chosen because (1) it is a good representation of the typical J_{sc} values obtained for a triple junction solar cell based on an SHJ bottom cell, and (2) It is the same value used in the reference model [70], which would help in validating the model implemented in this study.

5.1.1. Porosity (J_θ):

The current density after accounting only for porosity losses J_θ is determined as follows:

1. Determine porosity as $\theta = f(D_p, P_p)$
2. Determine pore coverage factor $(1 - \theta)$
3. Determine current density after accounting for porosity $J_\theta = (1 - \theta) \times J_{OP}$

Figure 5.1(a) shows a contour plot of the current density $J_{\theta, norm}$, which is normalized to the pre-set $J_{OP} = 8.13 \text{ mA/cm}^2$, as a function of D_p and P_p . A higher porosity will lead to reduction in the area available for light absorption, which results in a proportional reduction in the photocurrent. Smaller diameters and larger pitches yield better performance, as is expected since such combinations lead to lower porosities. For $D_p/P_p = 20\mu\text{m}/250\mu\text{m}$ the porosity is only 0.5% $\rightarrow J_{\theta, norm} = 0.995$, while for $80\mu\text{m}/100\mu\text{m}$, the porosity is around 50.3%, reducing J_{OP} by more than half.

5.1.2. pH Gradient (J_{pH}):

The current density after only accounting for pH gradient losses J_{pH} is determined as follows:

1. Determine pH gradient between anode and cathode from COMSOL simulations

2. Determine H^+ concentration at anode and cathode
3. Determine Δf between electrodes from Nernst equations
4. Determine overpotential losses E_{Loss}
5. Determine current density loss ΔJ_{BV} via the Butler-Volmer Equation
6. Determine current density $J_{pH} = J_{OP} - \Delta J_{BV}$

Figure 5.1(b) shows a contour plot of the normalized current density $J_{pH, norm}$ as a function of diameter and pitch considering losses due to pH gradient only.

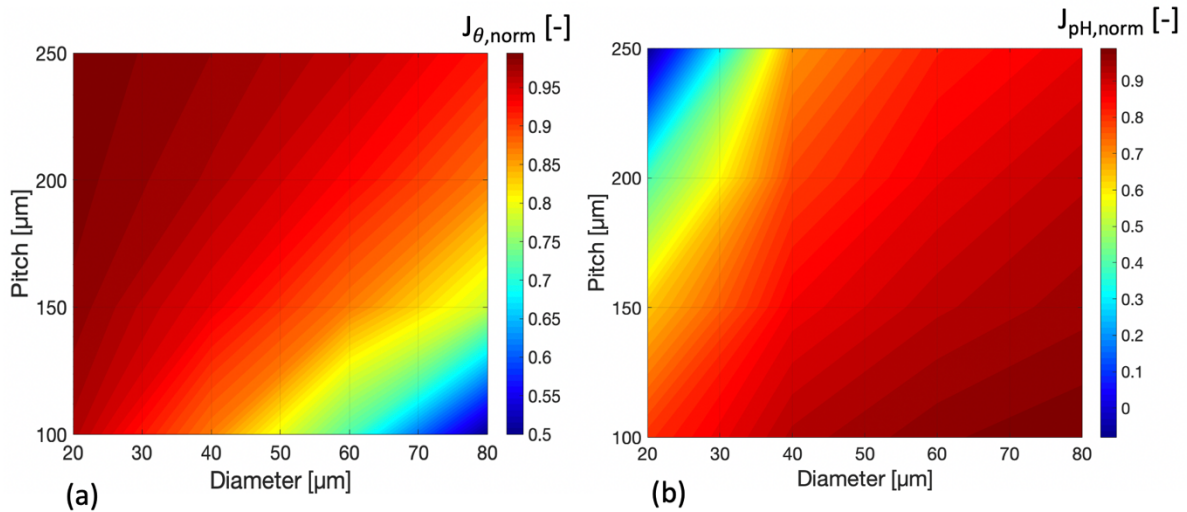


Figure 5.1: Contour plot of the normalized current density: (a) $J_{\theta, norm}$ when only porosity is accounted for; (b) $J_{pH, norm}$ when only pH gradient losses are considered.

The trend is opposite when only pH gradient losses are considered. A larger pH gradient between the electrodes indicates that proton flow from the anode to the cathode is more restricted. This occurs when the spacing between the holes gets larger, limiting surface proton transport (SPT), or when diameters are smaller, which leads to a more constricted proton flow inside the pores (IPT), as is evident from Figure 5.1(b). For $D_p/P_p = 20\mu m/250\mu m$, $J_{pH, norm} = -8\%$, while for $80\mu m/100\mu m$ it is over 98.5%. Note that a negative $J_{pH, norm}$ is obtained when $\Delta J_{BV} > J_{OP}$.

5.1.3. Porosity + pH Gradient ($J_{overall}$):

The porosity and pH gradient losses are combined as follows to yield the overall current density $J_{overall}$:

1. Determine J_{pH} as discussed in section 5.1.2
2. Multiply by the pore coverage factor $(1 - \theta)$ to get $J_{overall}$

Figure 5.2 shows a contour plot of the normalized overall current density $J_{overall, norm}$, as a function of D_p and P_p .

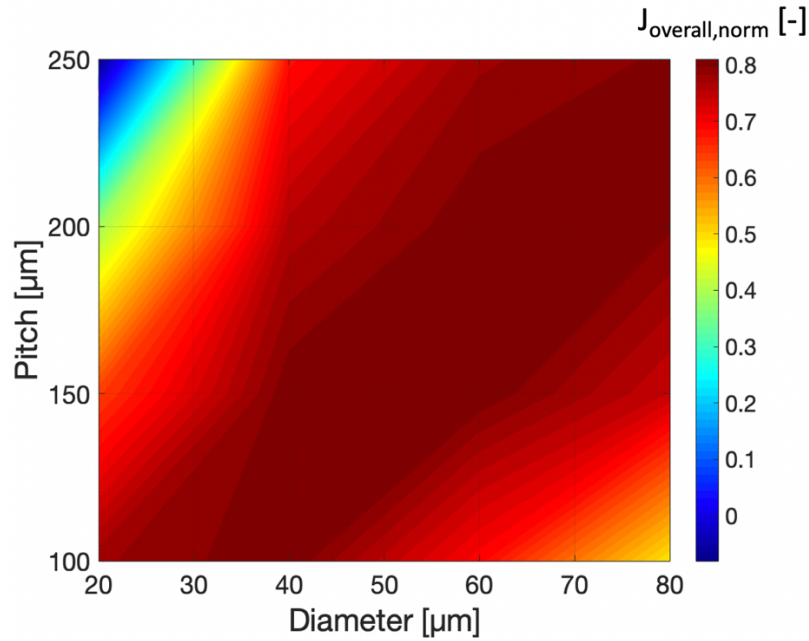


Figure 5.2: Contour plot of the normalized current density $J_{\text{overall,norm}}$ when both porosity and pH gradient losses are considered.

From Figure 5.2 it is clear that for this system, the influences of porosity and pH gradient are similar in magnitude and trend oppositely, with pH gradient losses being slightly more significant, as the optimum range is a bit offset from the center towards larger diameters and smaller pitches.

5.1.4. Defining the Optimum Pore Size and Distribution

Figure 5.2 shows that the optimal D_p/P_p combinations extend diagonally across the whole diameter range. Therefore, a good approach is to optimize the hole spacing for each diameter then plotting them against $J_{\text{overall,norm}}$ to determine how the optimum trends. Figure 5.3 plots $J_{\text{overall,norm}}$ versus the optimal spacing for each diameter in the series, in addition to 10 μm .

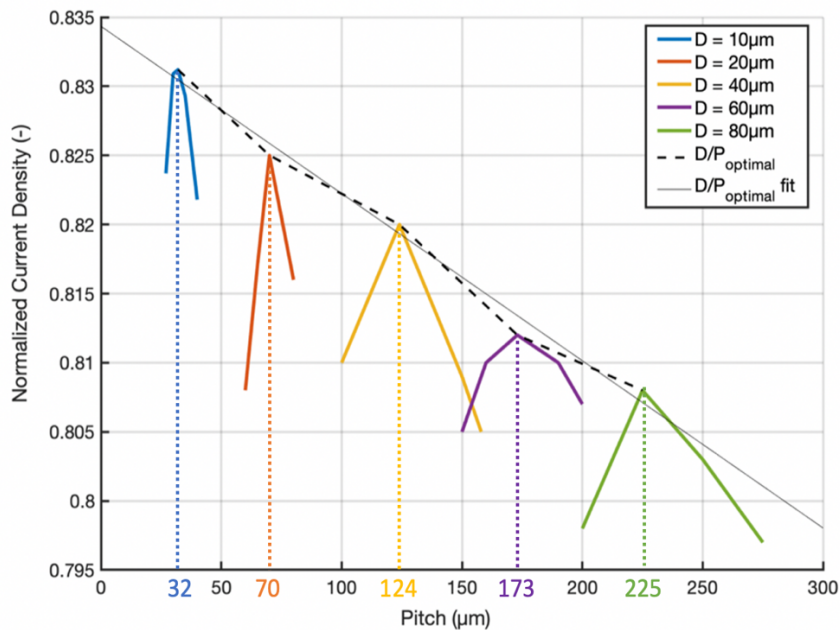


Figure 5.3: Plot of the normalized overall current density as a function of pore diameter, considering optimal pore spacing.

The trend clearly shows that the current density is maximized as D_p and $P_p \rightarrow 0$. Considering pore diameters $\geq 1 \mu\text{m}$ to be the fabrication and/or operational limit, the PMP cell can retain a maximum $\sim 83.4\%$ of the PV photocurrent when operated at 0.1 M proton concentration and without a PEM. Again, it should be noted that the electrodes and absorber are assumed ideal in this model, so the current density may be overestimated. Based on Figure 5.3, the maximum overall current density is for the 10 μm pores and is about 2.3% (absolute) larger than the 80 μm pores. However, in the simulations, all the components in the PMP cells, except for the electrolyte, are assumed ideal. Thus, a larger performance contrast may be expected when comparing actual devices.

5.1.5. Generalizing the Influence of Pore Size & Distribution

The results from the previous section pertain to the system developed in this study. By parameterizing the system differently, namely via changing the electrode material, the electrolyte composition and concentrations, or electrolyte conductivity, if the Supporting Electrolyte Charge Conservation Model (SE CCM) is used, it is possible to change the magnitude of the pH gradient for a given hole pattern. Proton Exchange Material (PEM) may also be included in the model to enhance IPT, which would reduce the pH gradient, as the simulations in Figure B1 from Appendix B show.

The simulations indicate that the average simulated pH gradient ($\Delta\text{pH}_{\text{sim}}$) for the optimal set is around 0.18 ± 0.0075 pH units. However, when the pores are in-filled with PEM or if a different PMP technology is used, different pH gradient (ΔpH) values could be obtained. So, how does changing the magnitude of ΔpH affect the trend of the optimal D_p/P_p combinations?

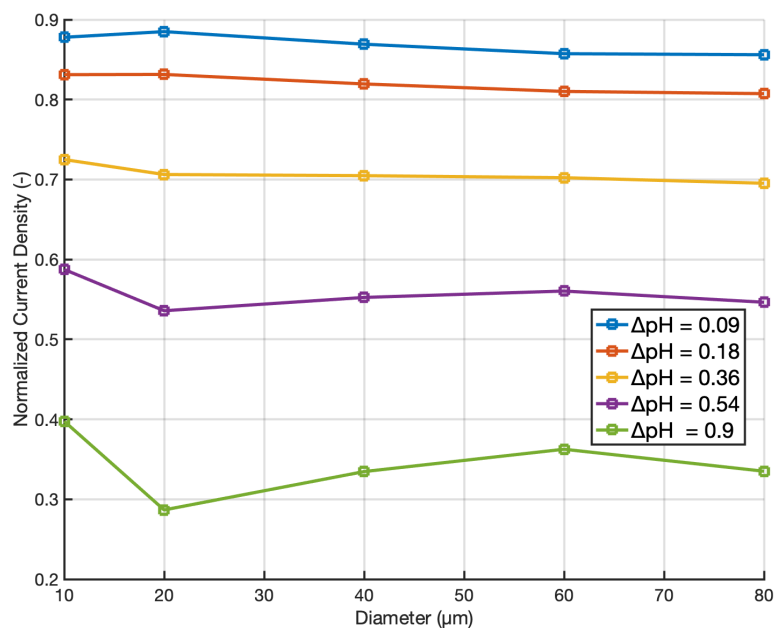


Figure 5.4: Plot of the normalized overall current density as a function of pore diameter, considering optimal pore spacing, for different pH gradient values: (1) $\frac{1}{2}\Delta\text{pH}_{\text{sim}}$; (2) $\Delta\text{pH}_{\text{sim}}$; (3) $2\Delta\text{pH}_{\text{sim}}$; (4) $3\Delta\text{pH}_{\text{sim}}$; (5) $4\Delta\text{pH}_{\text{sim}}$.

Figure 5.1.4 plots the normalized overall current density versus the optimal D_p/P_p combinations, wherein $\Delta\text{pH}_{\text{sim}}$ is multiplied by a factor of: $\frac{1}{2}$, 2, 3, and 4, to simulate a range of ΔpH values. It is directly apparent that in order to retain $> 70\%$ of the PV current, ΔpH cannot exceed 0.36 pH units. In such cases, the porosity losses are more significant, which would explain why the optimum lies at $D_p = 20 \mu\text{m}$, as it also happens to have the lowest porosity in the optimal set. Moreover, the spread in performance is relatively small when compared with larger gradients. For $\Delta\text{pH} = \frac{1}{2}\Delta\text{pH}_{\text{sim}}$, the spread in the normalized overall current density is around 0.13 % (absolute), versus 0.41 % (absolute) for ΔpH

$= 4\Delta\text{pH}_{\text{sim}}$. As the pH gradient becomes more significant, it overtakes the porosity in influencing the performance. The 20 μm pore diameters actually have the largest $\Delta\text{pH}_{\text{sim}} = 0.191$ pH units, which explains the minimum normalized current density at 20 μm when ΔpH is high.

Following this theoretical approach, the optimal range of pore size and distribution for PMP cells has been determined, based on the pH gradients obtained from COMSOL simulations and theory covered in Chapter 2. Moreover, the performance of the optimal patterns was also assessed by varying magnitude of the pH gradient for each hole pattern for more comprehensive optimization, extending the applicability of this approach to different PMP technologies.

6. Experimental Results

Due to the Coronavirus pandemic, as well as untimely issues with the equipment, namely the Deep Reactive Ion Etcher and the laser, there was a significant delay in conducting the pore processing experiments, which limited the potential progress that was initially expected. Additionally, the anode microdot deposition procedure was not optimized in time to fabricate and measure full devices. Therefore, J-V and EQE characterization could only be done for SHJ's with only a Pt back contact and an Al grid at the front side (no holes or microdots). Moreover, without the anode microdots, the EC component of the PMP device is not complete, meaning that J-E measurements could not be done. This Chapter is, therefore, structured in the following manner:

1. Challenges encountered with the microdot processing step
2. Results from the DRIE pore processing experiments
3. Results from the PLD pore processing experiments
4. Applying the theoretical optimization approach to the experimental dataset

6.1. Anode Microdot Challenges

The main hurdle to processing a complete PMP device is the anode microdot deposition. Though following the standard lithography and Pt deposition process for the hole patterned cathode is consistently successful, the same is not the case for the anode. After Pt deposition, the photoresist film is uniformly cracked with the generic features, such as the alignment markers and verniers still visible, while the square arrays of microdots having completely disappeared. NMP lift-off was done to remove the cracked photoresist layer; however, after 2 hours of sonication, the wafer surface is still visibly littered with Pt islands < 1 μm in diameter, with none of the microdot squares deposited. The partial and random deposition of Pt on the anode side disqualifies the wafer from further processing.

The first adjustment was reducing the Pt deposition rate from 3 $\text{\AA}/\text{s}$ to 1 $\text{\AA}/\text{s}$. The lower deposition rate would reduce the pressure inside the chamber and was expected to reduce or eliminate cracking. For this experiment, two test wafers were patterned with the anode microdots, following the standard procedure, and deposited at the lower deposition rate. However, besides the fact that the cracking persisted, all the square arrays disappeared after Pt deposition and did not re-appear after NMP lift-off, same as with the first attempt.

It appeared as though the issue had to do with the incomplete development of the photoresist in the microdot region. Thus, the next approach was to reduce the photoresist thickness from 3.5 μm to 3 μm and 2 μm , while keeping all other parameters constant, including the 1 $\text{\AA}/\text{s}$ Pt deposition rate. In this case, after Pt deposition, all 32 microdot square cells were visible. Again, the cracking was not reduced. However, after NMP lift-off, the pattern completely disappeared yet again.

To ensure that the microdot pattern gets completely developed, a wafer coated with 3 μm Nl0f2020 layer was developed in MF322 for 10 minutes, after which some of the squares began discoloring.

After Pt deposition, the cracking persists, as expected, but a few microdot squares were visible after Pt deposition and NMP lift-off. Out of 8 square per quadrant, about 1 – 2 whole cells survived and another 1 – 2 with more than 50% of the pattern visible.

The microdot deposition was far from optimal, and there was hesitation about processing the SHJ further with microdots, without certainty that each hole pattern would have at least one complete cell. Regardless, however, the contact aligner broke down before this or any further processing could be done, prior to concluding this thesis. Without a contact aligner, it is not possible to do any lithographic patterning.

The next “intended” step was to look into the baking and exposure parameters in the patterning process. It is likely that the photoresist in the microdot region is adhering more strongly than it should to the wafer. Since this is a negative photoresist, it is possible that lower thermal energy input could reduce polymerization and allow the film to develop properly. The first experiment is to reduce the post bake time from 60 seconds to 30 seconds and 15 seconds. As mentioned earlier in the Chapter 4, without a post-expose bake, the film is completely removed during development in under 30 seconds, so it may be possible to find an optimal development time.

If that is to fail, the next attempt would involve reducing the exposure time from 20 seconds to 15 seconds and 10 seconds. The microdots are very closely spaced (3 μm apart), so it is possible that the exposure time is too long, such that the small, closely spaced features in the un-exposed areas indirectly receive an excess of thermal energy during exposure and begin to cross-link, adhering more strongly to the wafer.

6.2. Deep Reactive Ion Etching

DRIE processing sessions could not begin till three months prior to the thesis deadline. Moreover, the available etchers did not have a suitable recipe for achieving high aspect ratios for samples coated with soft masks, like photoresist. Luckily, Xu et al had already developed a high aspect ratio DRIE recipe that can yield close to perfect cylindrical pore morphology with practically no tapering [104]. Xu et al did their processing, however, using a different instrument, so the recipe may not necessarily yield the same results with the AMS110, and serves more as a starting point.

The first DRIE test (DRIE-1) performed was the original recipe for 1 hour and 49 minutes, which corresponds to a depth of 310 μm for 33 μm pore diameter according to [90]. The results of DRIE-1 were quite promising. For each diameter, the pores had a cylindrical shape with essentially no tapering and essentially identical depths, as shown in the SEM in Figure 6.1.

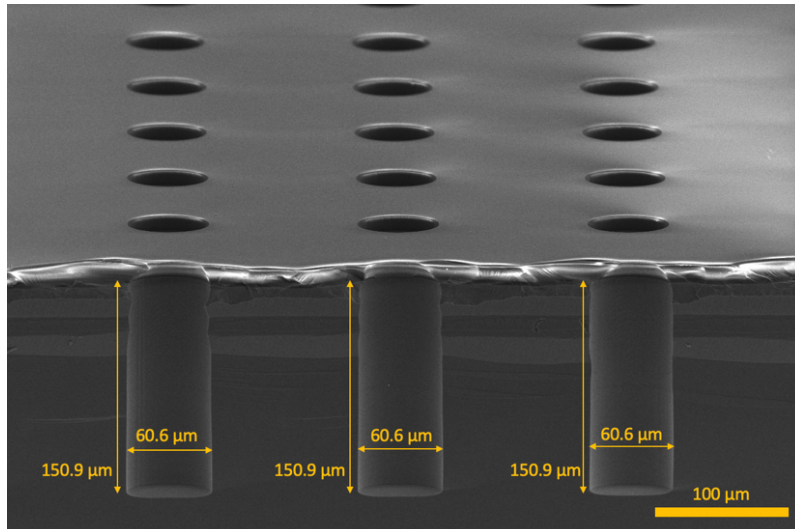


Figure 6.1: 60 μm pores etched 150.9 μm deep via DRIE following the recipe from [90].

However, none of the pores went through the entire wafer thickness. The etch depths range from around 125 to 165 μm for 20 – 80 μm pore diameters, respectively. To avoid drastically changing what appears to be an optimized recipe, for DRIE-2, only the etch time was increased to 4 hours and 15 minutes. With the exception of the 20 μm pores, all the holes penetrated through the entire device, as can be seen in Figure 6.2(a).

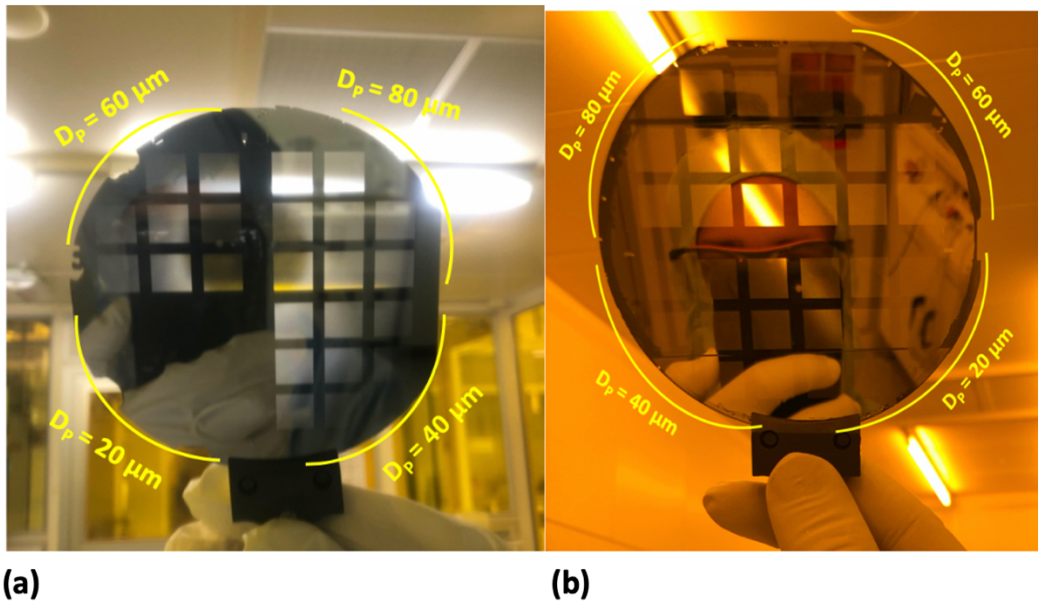


Figure 6.2: Complete penetration achieved for: (a) All pore diameters, except 20 μm, after 4 hours and 15 minutes; (b) All pore diameters (20μm – 80μm) after 6 hours 30 minutes of DRIE.

The SEM cross section in Figure 6.3 indicates that the 20 μm pores from DRIE-2 still has about 15% of the depth to go through. The holes have the same morphology as in DRIE-1, with the top and bottom diameters being practically equal. The central parts of the pores in the SEM are hidden due to improper scribing during cross section preparation. Finally, after 6 hours and 30 minutes of etching (DRIE-3), all the pores managed to go through, as shown in Figure 6.2(b).

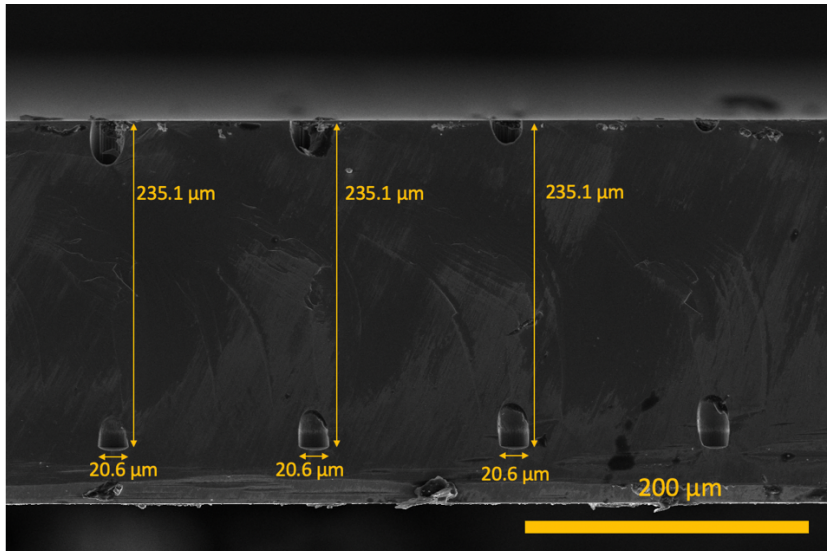


Figure 6.3: 20 μm diameter pores with an etch depth of 235.1 μm after 4 hours and 15 minutes of DRIE using the recipe from [90].

One of the main issues with this step has to do with the pattern design. Since different pore diameters get etched through at different rates, the wider diameter pores will reach the bottom of the wafer much quicker, as shown earlier. Thermal effects appear to take place at the bottom side of the wafer, and seem to be worse for wider pores, as shown when contrasting Figure 6.4 for 20 μm pores and Figure 6.5 for 60 μm pores. This suggests that the longer an open pore is exposed during DRIE, the more damage takes place at the bottom (anode) side. In some cases, the microdots appear to have deformed into streaks, as is the case in Figure 6.5. Another issue is the front-to-back alignment. Since the alignment was done on a still rather than live image, slight shifting cannot be detected, or corrected for. Thus, the pores actually go through the Pt on the anode side, which goes against the purpose of their patterning.

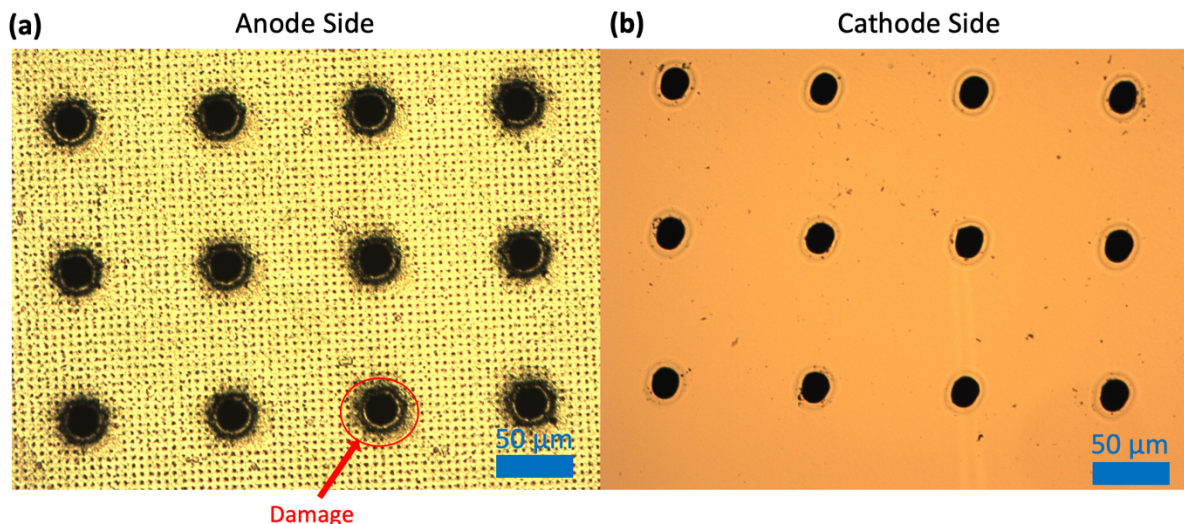


Figure 6.4: 20 μm diameter pores: (a) Anode side; (b) Cathode side.

The DRIE pore processing method still requires some optimization. For one, the etch rate needs to increase to avoid backside heating effects. Based on this recipe, the etch rate is $< 1 \mu\text{m}/\text{minute}$, when it should be able to reach $10 - 20 \mu\text{m}/\text{minute}$, while maintaining good morphology. Additionally, the time required to penetrate through the whole thickness for each diameter should be accurately

determined. That way, when each set of pores is etched through, they can be covered with an oxidized Silicon wafer piece to prevent over-etching during the remainder of the process.

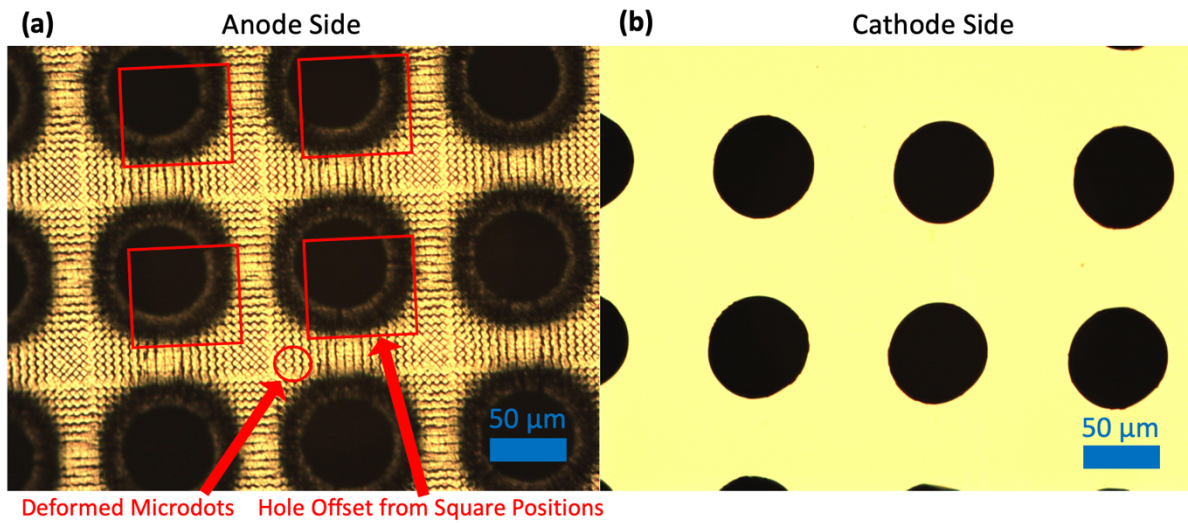


Figure 6.5: 60 μm diameter pores: (a) Anode side; (b) Cathode side.

Once the DRIE procedure is optimized, wherein no damage is incurred to the backside, the next step would involve testing polyetch solution treatments for passivating and smoothing the sidewalls, followed by pore in-filling with Proton Exchange Material (PEM).

From a morphological standpoint, it is possible to achieve consistent and near perfect pores using DRIE, even for substrates that are hundreds of microns thick. However, obtaining good morphology with near perfect cylindrical holes requires well-tuned parameters, such as to minimize front side over-etching and backside thermal effects, as well as processing time. The DRIE process requires lithographic patterning in order to etch out the pores. It is also expensive and time-consuming, introducing more steps into the fabrication process and requiring expensive chemicals. Furthermore, in an industrial context, the manufacturing facility has to invest in a DRIE etching system, as well as a coating, exposure, and development system for lithographic patterning.

6.3. Pulsed Laser Drilling

For PLD, preliminary drilling experiments were done to determine the parameter ranges suitable for this application. These tests helped in designing the sample preparation procedure and accounting for important considerations, such as including a stable substrate holder.

The two main laser parameters considered are the pulse energy E_{pulse} and number of pulses N_{pulse} . To narrow the ranges, pores were drilled at $E_{\text{pulse}} = 20\%$, 5% , and 1% , with N_{pulse} ranging from 2 to 400. Figure 6.6 shows the results along with the number of pulses needed to go through. For energies $> 1\%$ the drilling process results in re-deposited materials on the surface around the pore. However, the taper is significantly larger when 1% energy is used, and more pulses are needed to go through. For all cases, the entrance diameters are $> 200 \mu\text{m}$, falling well outside the diameter range of interest ($20 - 80 \mu\text{m}$).

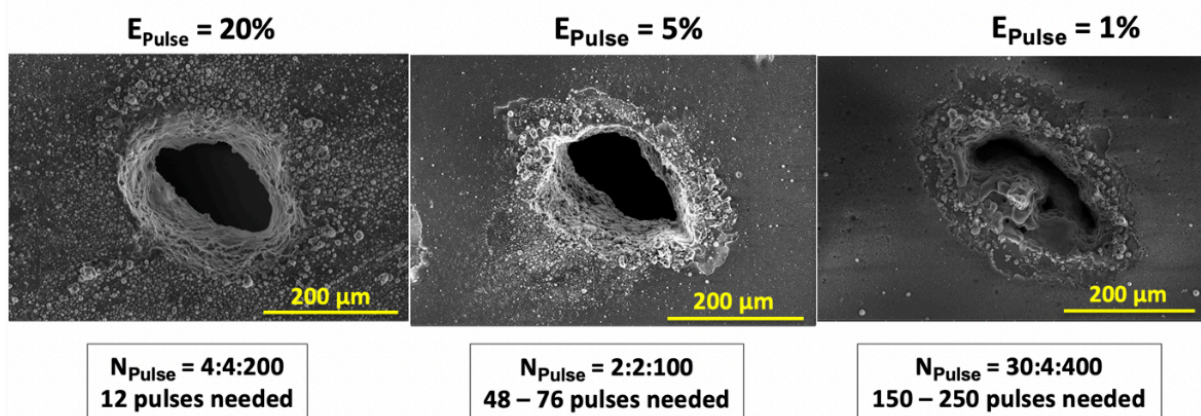


Figure 6.6: (from left to right) Pores drilled at $E_{\text{pulse}} = 20\%$, 5% , and 1% , respectively.

Figure 6.7 shows that there is no difference in morphology when the pores are laser drilled from the cathode side (Pt) or the anode side (ITO); however, the taper is significantly smaller when drilling from the Pt, or cathode side, since as a noble metal, Pt is more inert towards laser drilling than ITO and is harder to go through.

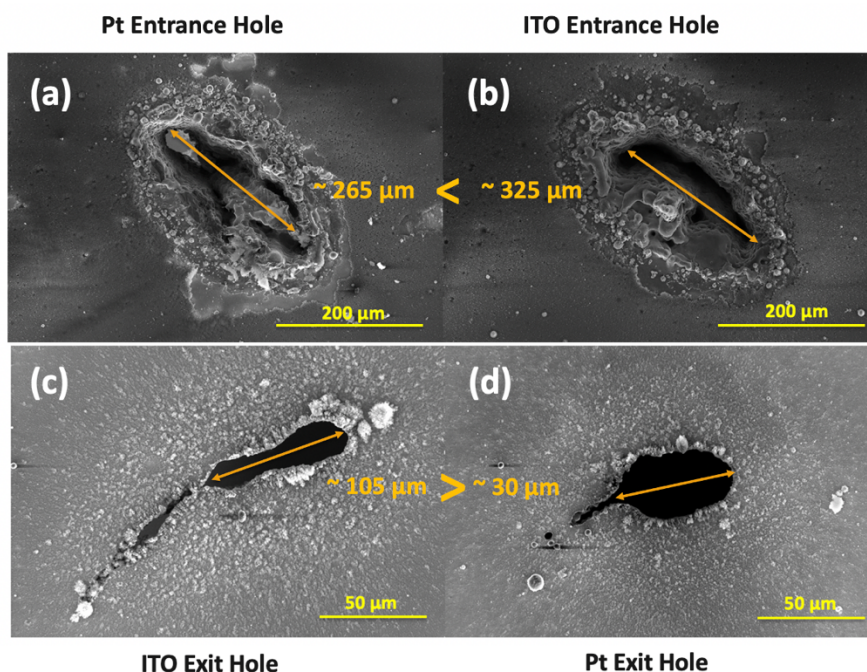
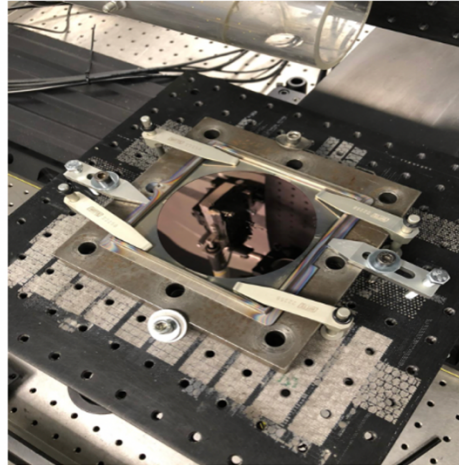
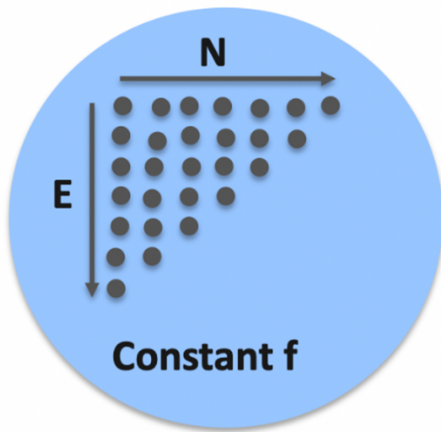


Figure 6.7: SEM images of: (a) Pt entrance hole; (b) ITO entrance hole; (c) ITO exit hole; (d) Pt exit hole.

Furthermore, it is preferable to have the smaller exit holes at the illuminated (anode) side, since most of the light absorption takes place in the top part of the cell. Thus, the drilling is done from the cathode side. An optimization experiment was devised, wherein a triangular matrix of holes would be processed onto a wafer with varying E_{pulse} and N_{pulse} , as shown in Figure 6.8(a). The matrix would then be evaluated using an automated analysis technique that involves a Keyence Microscope.



(a)

(b)

Figure 6.8: (a) Illustration of the triangular pore matrix for the parameter optimization experiments; (b) Photograph of the substrate holder used to stabilize the wafer.

In addition to the abovementioned consideration, a substrate holder was made to keep the wafer stable during drilling while preventing the bottom side from touching the stage, as shown in Figure 6.8(b). A 12 μm thick AZ12XT photoresist layer was applied at the cathode as a TCB layer. The wafer was roughly handled before stripping the photoresist layer with NMP. Figure 6.9 shows that the Pt surface is practically spotless and unharmed by the drilling process after removing the coat. Ideally, another layer should be applied on the opposite side as well to avoid re-deposition on the anode upon punching through the wafer.

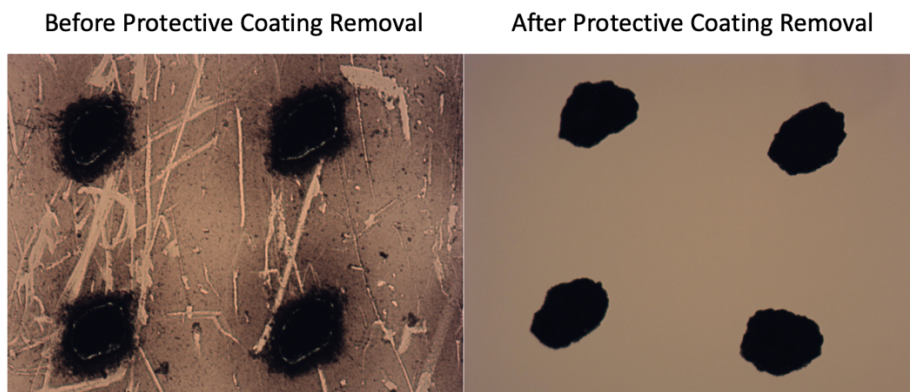


Figure 6.9: Wafer surface before and after removal of the protective photoresist layer.

Shortly after the preliminary tests, the laser began encountering stability issues. So, the first few sets of holes from the optimization experiment did not yield conclusive results. The laser operator managed to, eventually, achieve stability for a maximum of 1000 holes per drilling session with 20 minutes breaks in between. Figure 6.10 shows reproducible pores with an average entrance diameter $D_i = 104.7 \pm 4.1 \mu\text{m}$ and an average exit diameter $D_o = 46.7 \pm 2.6 \mu\text{m}$, measured in three separate areas. The PLD parameters for these pore dimensions are $E_{\text{Pulse}} = 0.58 - 0.6 \%$ and $N_{\text{Pulse}} = 80 - 90$. Unfortunately, the operator was scheduled to go on leave about a week after this was accomplished, which did not leave sufficient time to prepare actual devices for PLD processing. Thus, the performance of PLD processed PMP cells was not characterized.

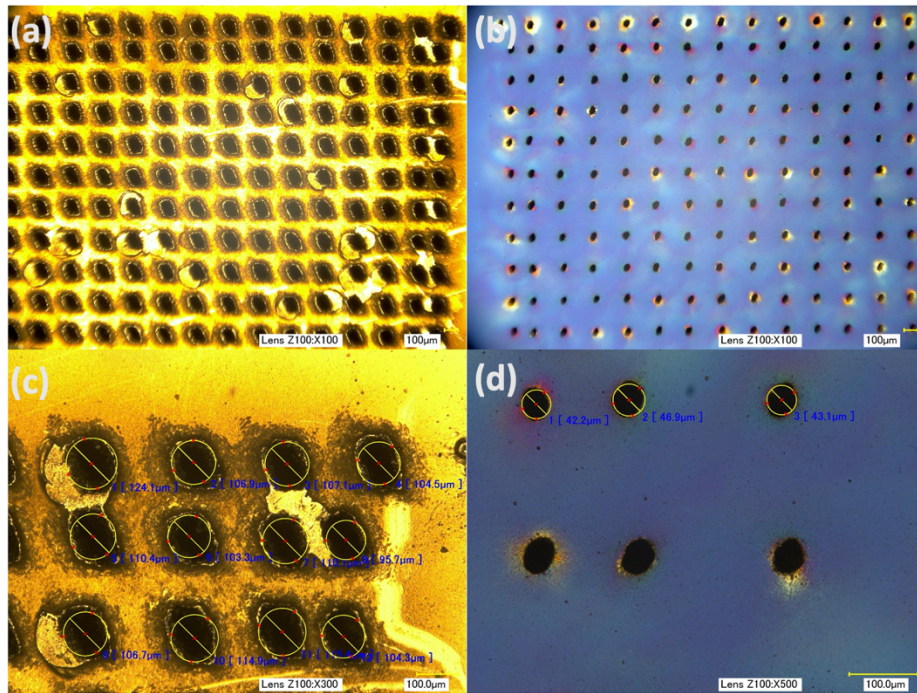


Figure 6.10: Reproducible PLD processed pores at $E_{Pulse} = 0.58 - 0.6 \%$ and $N_{Pulse} = 80 - 90$. (a) and (c) show the cathode side (entrance holes), while (b) and (d) show the anode side (exit holes).

The morphology of PLD processed holes is rather poor compared to DRIE. The pores have rough sidewalls and are more elliptical than circular, an indication that the laser is out of focus. The cross section in Figure 6.11 shows how rough the sidewalls are. Though, as earlier mentioned, polyetch treatment can smoothen the sidewalls. Furthermore, there is a significant taper ~ 0.21 , with $D_i > 2D_o$. The achievable resolution for PLD is also poorer, as the minimum D_i achievable $> 80 \mu m$. On the other hand, assuming a robust and stable laser is used, processing pores with PLD does have its benefits for industrial applications. For one, lithography, or any additional processing steps for that matter, are not required, granted that XY scanning capability is available, though a TCB layer may be required to protect the device surfaces.

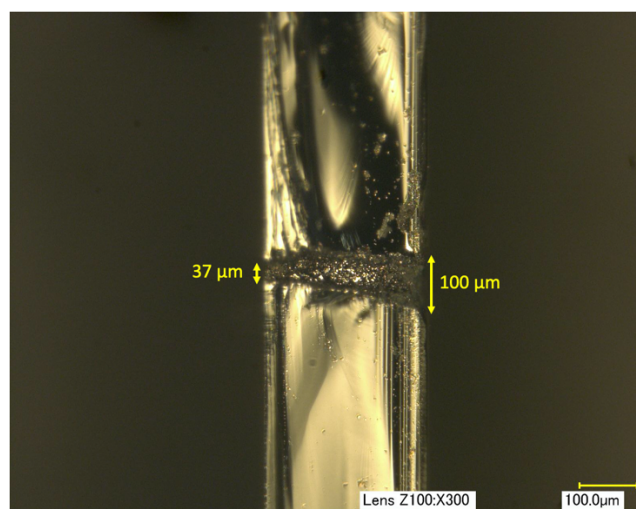


Figure 6.11: Cross-section of PLD processed pore, indicating clear sidewall roughness.

Though, ideally, cylindrical pores are desired, it is possible that the taper could have an enhancement effect on In-pore Proton Transport IPT. The protons are generated at the anode, where the exit holes are located. Therefore, it is likely that the protons would experience a less constricted flow as they

travel deeper into the pore. This hypothesis could have been tested had there been sufficient time to prepare PLD processed cells and compare them to the DRIE processed ones that have perfectly cylindrical sidewalls.

PLD processing may have more potential for PMP devices based on thin film substrates, like flexible conductive foils. They would require relatively lower laser energies and fewer pulses, since they have smaller thicknesses $< 20 \mu\text{m}$, which could potentially yield smaller pore diameters. The cross section in Figure 6.11 shows almost no taper in the first $30 \mu\text{m}$ of the pore depth, so this issue may be eliminated in the case of thin film-based devices. Moreover, thin film PV technologies already require a laser facility for isolating the individual solar cells across the module. It is, thus, possible to use the same laser system to also process the pores, which would lead to lower investment costs for expanding the facility to include PMP cell processing.

7. Conclusion and Recommendations

7.1. Conclusion

In this work, the effect of pore size and distribution on the performance of PMP cells was analyzed, in the effort to determine the optimal hole pattern or range of patterns that are suitable for this application. A theoretical framework was established, to account for losses associated with PV performance (Porosity) and EC performance (Proton Transport) for different pore patterns. Additionally, two pore-processing techniques were compared, namely Deep Reactive Ion Etching and Pulsed Laser Drilling, to determine their suitability for this application.

The results from the theoretical analysis indicate that a larger portion of the PV current is retained when smaller pore diameters and pitches are used. The optimal range was found to extend across the entire diameter region considered in this study, thus, a local optimization was done for each diameter. The spread in overall performance, based on pore diameter was limited to 2.3 % when the magnitude of the pH gradient is limited to < 0.2 pH units, and a minimum of 70% of the PV current can be retained if $\Delta\text{pH} < 0.36$ pH units. When comparing the DRIE and PLD pore processing methods, it is clear that DRIE can achieve better morphology (perfectly cylindrical, no tapering, smoother sidewalls) and has a higher rate of reproducibility compared to PLD. However, PLD processing is more practical from a manufacturing perspective, as it does not require lithographic patterning of the pore positions and does not need vacuum conditions. Moreover, in the case of thin film PV technologies, the same laser scribing instruments used for isolating individual cells in modules, could be used for pore processing. Which reduces investment requirements for thin film-based PMP cell processing. The PMP cell fabrication procedure was not fully developed, as issues relating to the anode microdot deposition and DRIE pore processing steps still needed to be addressed. However, luckily, it was possible to obtain a few completed PMP cells, which were then used to qualitatively assess the hydrogen generation capability of these devices.

7.2. Recommendations

Due to delays mentioned previously, a large fraction of the experimental work could not be concluded:

1. Complete two full experimental dataset (2 wafers): (1) DRIE processed and (2) PLD processed
2. Fabricate and characterizing the wafer thickness series (100, 200, and 300 μm)
3. Apply the polyetch treatment for sidewall smoothing
4. In-fill PMP cell pores with Nafion[®] PEM
5. Fabricate and characterize completed triple junction Silicon PMP cells
6. Fabricate and characterize completed thin film Silicon PMP cells

For future work, the most important step is to finalize the fabrication procedure and J-E measurement setup, so more focus could be put on characterization rather than optimization. Next, is to compare J-V and J-E results of PLD and DRIE processed devices for a more accurate determination of which process is more suitable for this application. The thickness series will be useful in this determination, since pores for thinner devices can be processed more easily and with better morphology, while yielding better EC performance, due to shorter ionic transport distances. Optimizing the polyetch treatment and Nafion[®] in-filling procedures will be necessary before complete PMP cells can be

analyzed. Given the limited photovoltage of SHJ's relative to what is required for water splitting, evaluating the overall performance of a complete Silicon based PMP cell will require the use of a multi-junction Si solar cell that can achieve sufficient photovoltages in the range of 1.7 – 2 V. Since thickness plays a crucial role in defining the performance and practicality of manufacturing of PMP cells, devices based on thin film Silicon, as opposed to thick c-Si wafer-based cells, should also be evaluated and compared to their thicker counterparts in terms of processing complexity and overall STH performance. This serves to further highlight the suitability of each technology (wafer versus thin film) for this application.

8. Bibliography

- [1] "Electricity Information 2019," Electricity Information, 2019.
- [2] "World Energy Outlook 2019," World Energy Outlook, 2019.
- [3] K. Hashimoto, "Current Situation of Energy Consumption and Carbon Dioxide Emissions of Our World," *Global Carbon Dioxide Recycling SpringerBriefs in Energy*, pp. 25–31, 2019.
- [4] J. Jurasz, F. Canales, A. Kies, M. Guezgouz, and A. Beluco, "A review on the complementarity of renewable energy sources: Concept, metrics, application and future research directions," *Solar Energy*, vol. 195, pp. 703–724, 2020.
- [5] S. R. Sinsel, R. L. Riemke, and V. H. Hoffmann, "Challenges and solution technologies for the integration of variable renewable energy sources—a review," *Renewable Energy*, vol. 145, pp. 2271–2285, 2020.
- [6] P. A. Østergaard, N. Duic, Y. Noorollahi, H. Mikulcic, and S. Kalogirou, "Sustainable development using renewable energy technology," *Renewable Energy*, vol. 146, pp. 2430–2437, 2020.
- [7] T. Ameri, N. Li, and C. J. Brabec, "Highly efficient organic tandem solar cells: a follow up review," *Energy & Environmental Science*, vol. 6, no. 8, p. 2390, 2013.
- [8] M. Junginger and A. Louwen, "Technological learning in the transition to a low-carbon energy system: conceptual issues, empirical findings, and use, in energy modeling". London, United Kingdom: Academic Press, 2020.
- [9] J. Rongé, T. Bosserez, D. Martel, C. Nervi, L. Boarino, F. Taulelle, G. Decher, S. Bordiga, and J. A. Martens, "Monolithic cells for solar fuels," *Chem. Soc. Rev.*, vol. 43, no. 23, pp. 7963–7981, 2014.
- [10] Z. Hu, "Integration of Large-Scale Energy Storage System into the Transmission Network," *Energy Storage for Power System Planning and Operation*, pp. 185–202, 2020.
- [11] J. H. Kim, D. Hansora, P. Sharma, J.-W. Jang, and J. S. Lee, "Toward practical solar hydrogen production – an artificial photosynthetic leaf-to-farm challenge," *Chemical Society Reviews*, vol. 48, no. 7, pp. 1908–1971, 2019.
- [12] A. Collinson, "The Costs and Benefits of Electrical Energy Storage," *Renewable Energy Storage*, pp. 25–33, 2014.
- [13] Y. Mao, "Branched nanostructures for photoelectrochemical water splitting," *Nanomaterials and Energy*, vol. 3, no. 4, pp. 103–128, 2014.

- [14] P. Arunachalam and A. M. A. Mayouf, "Photoelectrochemical Water Splitting," Noble Metal-Metal Oxide Hybrid Nanoparticles, pp. 585–606, 2019.
- [15] W. Wang, M. Xu, X. Xu, W. Zhou, and Z. Shao, "Perovskite Oxide Based Electrodes for High-Performance Photoelectrochemical Water Splitting," *Angewandte Chemie International Edition*, vol. 59, no. 1, pp. 136–152, 2020.
- [16] R. Rath, P. Kumar, S. Mohanty, and S. K. Nayak, "Recent advances, unsolved deficiencies, and future perspectives of hydrogen fuel cells in transportation and portable sectors," *International Journal of Energy Research*, vol. 43, no. 15, pp. 8931–8955, 2019.
- [17] C. Wei, R. R. Rao, J. Peng, B. Huang, I. E. L. Stephens, M. Risch, Z. J. Xu, and Y. Shao-Horn, "Recommended Practices and Benchmark Activity for Hydrogen and Oxygen Electrocatalysis in Water Splitting and Fuel Cells," *Advanced Materials*, vol. 31, no. 31, p. 1806296, 2019.
- [18] Jäger Klaus-Dieter, O. Isabella, A. Smets, Swaaij René van, and M. Zeman, "Solar energy: The physics and engineering of photovoltaic conversion technologies". Cambridge: UIT Cambridge, 2016.
- [19] PVEducation. [Online]. Available: <https://www.pveducation.org/pvcdrom/introduction/introduction>.
- [20] K. A. Conley, "Solar energy". Minneapolis, MN: Core Library, an imprint of Abdo Publishing, 2017.
- [21] M. Nell and A. Barnett, "The spectral p-n junction model for tandem solar-cell design," *IEEE Transactions on Electron Devices*, vol. 34, no. 2, pp. 257–266, 1987.
- [22] S. M. K. Team, "Si Silicon Element Information: Facts, Properties, Trends, uses and Compare silicon with other elements - Periodic Table of the Elements," 26-Jul-2020. [Online]. Available: <https://www.schoolmykids.com/learn/interactive-periodic-table/si-silicon>.
- [23] Cea, "TB_Sim," CEA/Modeling and Exploration of Materials Laboratory, 30-Jan-2019. [Online]. Available: http://www.mem-lab.fr/en/Pages/L_SIM/Softwares/TB_Sim.aspx.
- [24] N. Mahato, M. O. Ansari, and M. H. Cho, "Production of Utilizable Energy from Renewable Resources: Mechanism, Machinery and Effect on Environment," *Advanced Materials Research*, vol. 1116, pp. 1–32, 2015.
- [25] "Chapter 4: p-n Junctions," p-n Junctions. [Online]. Available: https://ecee.colorado.edu/~bart/book/book/chapter4/ch4_2.htm.
- [26] J. Ramanujam, D. M. Bishop, T. K. Todorov, O. Gunawan, J. Rath, R. Nekovei, E. Arregiani, and A. Romeo, "Flexible CIGS, CdTe and a-Si:H based thin film solar cells: A review," *Progress in Materials Science*, vol. 110, p. 100619, 2020.
- [27] P. Perez Rodriguez, "Photovoltaic-(photo)electrochemical devices for water splitting and water treatment," Delft University of Technology Dissertation, p 169, 2018.
- [28] X. Wang and A. Barnett, "The Evolving Value of Photovoltaic Module Efficiency," *Applied Sciences*, vol. 9, no. 6, p. 1227, 2019.

- [29] D. K. Kumar, J. Kříž, N. Bennett, B. Chen, H. Upadhayaya, K. R. Reddy, and V. Sadhu, "Functionalized metal oxide nanoparticles for efficient dye-sensitized solar cells (DSSCs): A review," *Materials Science for Energy Technologies*, vol. 3, pp. 472–481, 2020.
- [30] J. Fang, et al. "Improvement in Ultra-Thin Hydrogenated Amorphous Silicon Solar Cells with Nanocrystalline Silicon Oxide." *Solar Energy Materials and Solar Cells*, vol. 176, pp. 167–173, 2018.
- [31] T. K. Todorov, et al. "Materials Perspectives for next- Generation Low-Cost Tandem Solar Cells." *Solar Energy Materials and Solar Cells*, vol. 180, pp. 350–357, 2018.
- [32] M. T. Hörantner, and H. J. Snaith, "Predicting and Optimising the Energy Yield of Perovskite-on-Silicon Tandem Solar Cells under Real World Conditions." *Energy & Environmental Science*, vol. 10, no. 9, pp. 1983–1993, 2017.
- [33] T. P. White, N. N. Lal, K. R. Catchpole, "Tandem Solar Cells Based on High-Efficiency c-Si Bottom Cells: Top Cell Requirements for >30% Efficiency." *IEEE Journal of Photovoltaics*, vol. 4, no. 1, 2014, pp. 208–214. [8] N. N. Lal, et al. "Perovskite Tandem Solar Cells." *Advanced Energy Materials*, vol. 7, 2017.
- [34] T. D. Lee and A. U. Ebong, "A review of thin film solar cell technologies and challenges," *Renewable and Sustainable Energy Reviews*, vol. 70, pp. 1286–1297, 2017.
- [35] C. H. Lee, D. R. Kim, and X. Zheng, "Transfer Printing Methods for Flexible Thin Film Solar Cells: Basic Concepts and Working Principles," *ACS Nano*, vol. 8, no. 9, pp. 8746–8756, 2014.
- [36] A. K. Shukla, K. Sudhakar, and P. Baredar, "Recent advancement in BIPV product technologies: A review," *Energy and Buildings*, vol. 140, pp. 188–195, 2017.
- [37] P. E. Campana, L. Wästhage, W. Nookuea, Y. Tan, and J. Yan, "Optimization and assessment of floating and floating-tracking PV systems integrated in on- and off-grid hybrid energy systems," *Solar Energy*, vol. 177, pp. 782–795, 2019.
- [38] M. Powalla et al, "Thin-film solar cells exceeding 22% solar cell efficiency: An overview on CdTe-, Cu(In,Ga)Se₂-, and perovskite-based materials". *Applied Physics Reviews*, 5(4), 2018
- [39] T. Fiducia et al., "Understanding the role of selenium in defect passivation for highly efficient selenium-alloyed cadmium telluride solar cells". *Nature Energy*, 4(6), pp.526-526, 2019.
- [40] M. Nakamura, K. Yamaguchi, Y. Kimoto, Y. Yasaki, T. Kato, and H. Sugimoto, "Cd-Free Cu(In,Ga)(Se,S)₂ Thin-Film Solar Cell With Record Efficiency of 23.35%". *IEEE Journal of Photovoltaics*, 9(6), pp.1863-1867, 2019.
- [41] M. Elbar, S. Tobbeche, A. Merazga, "Effect of top-cell CGS thickness on the performance of CGS/CIGS tandem solar cell", *Solar Energy*, vol. 122, pp. 104-112, 2015.
- [42] F. Zhang, and K. Zhu, "Additive Engineering for Efficient and Stable Perovskite Solar Cells". *Advanced Energy Materials*, 2020.
- [43] J. Duan et al, "Lanthanide Ions Doped CsPbBr₃ Halides for HTM-Free 10.14%-Efficiency Inorganic Perovskite Solar Cell with an Ultrahigh Open-Circuit Voltage of 1.594 V". *Advanced Energy Materials*, 8(31), 2018.

- [44] M. Saliba et al. "Perovskite Solar Cells: From the Atomic Level to Film Quality and Device Performance", *Angewandte Chemie International Edition*, vol. 57, pp. 2554-2569, 2018.
- [45] M. K. Assadi et al. "Recent progress in perovskite solar cells", *Renewable and Sustainable Energy Reviews*, vol. 81, pp. 2812-2822, 2018.
- [46] Z. Shi, J. Ahalapitiya, "Perovskites-Based Solar Cells: A Review of Recent Progress, Materials and Processing Methods." *Materials*, vol. 11, no. 5, p. 729, 2018.
- [47] M. Spalla, "Effect of the Hole Transporting/Active Layer Interface on the Perovskite Solar Cell Stability". *ACS Applied Energy Materials*, 3(4), pp.3282-3292, 2020.
- [48] C. Wolff et al, "Perfluorinated Self-Assembled Monolayers Enhance the Stability and Efficiency of Inverted Perovskite Solar Cells". *ACS Nano*, 14(2), pp.1445-1456, 2020.
- [49] X. Yang et al, "Multifunctional Dye Interlayers: Simultaneous Power Conversion Efficiency and Stability Enhancement of Cs₂AgBiBr₆ Lead-Free Inorganic Perovskite Solar Cell through Adopting a Multifunctional Dye Interlayer". *Advanced Functional Materials*, 30(23), 2020.
- [50] C. Battaglia, A. Cuevas, S. De Wolf, "High-Efficiency Crystalline Silicon Solar Cells: Status and Perspectives." *Energy & Environmental Science*, vol. 9, no. 5, pp. 1552–1576, 2016.
- [51] J. Fang, et al. "Improvement in Ultra-Thin Hydrogenated Amorphous Silicon Solar Cells with Nanocrystalline Silicon Oxide." *Solar Energy Materials and Solar Cells*, vol. 176, pp. 167–173, 2018.
- [52] S. F. Tong, O. Isabella, M. Zeman, "Thin-film amorphous silicon germanium solar cells with p- and n-type hydrogenated silicon oxide layers", *Solar Energy Materials & Solar Cell*, vol. 163, pp. 9-14, 2017.
- [53] M. Stuckelberger, et al. "Review: Progress in solar cells from hydrogenated amorphous silicon", *Renewable and Sustainable Energy Reviews*, vol. 76, pp. 1497-1523, 2017.
- [54] S. Kirner, et al. "Quadruple-Junction Solar Cells and Modules Based on Amorphous and Microcrystalline Silicon with High Stable Efficiencies." *Japanese Journal of Applied Physics*, vol. 54, no. 8S1, 2015.
- [55] P. R. Cabarrocas, "Plasma Enhanced Chemical Vapor Deposition of Amorphous, Polymorphous and Microcrystalline Silicon Films." *Journal of Non-Crystalline Solids*, vol. 266-269, pp. 31–37, 2000.
- [56] F. Meillaud et al, "Recent advances and remaining challenges in thin-film silicon photovoltaic technology". *Materials Today*, 18(7), pp.378-384, 2015.
- [57] A. Banerjee et al., "High-Efficiency, Multijunction nc-Si:H-Based Solar Cells at High Deposition Rate," in *IEEE Journal of Photovoltaics*, vol. 2, no. 2, pp. 99-103, 2012.
- [58] M. Boccard, M. Despeisse, J. Escarre, X. Niquille, G. Bugnon, S. Hanni, M. Bonnet-Eymard, F. Meillaud, and C. Ballif, "High-Stable-Efficiency Tandem Thin-Film Silicon Solar Cell With Low-Refractive-Index Silicon-Oxide Interlayer," *IEEE Journal of Photovoltaics*, vol. 4, no. 6, pp. 1368–1373, 2014.

- [59] Tan, H., Moulin, E., Si, F., Schüttauf, J., Stuckelberger, M., Isabella, O., Haug, F., Ballif, C., Zeman, M. and Smets, A., "Highly transparent modulated surface textured front electrodes for high-efficiency multijunction thin-film silicon solar cells". *Progress in Photovoltaics: Research and Applications*, 23(8), pp.949-963, 2015.
- [60] M. Konagai, "Present Status and Future Prospects of Silicon Thin-Film Solar Cells". *Japanese Journal of Applied Physics*, 50(3R), 2011.
- [61] Y. Xu, Y., T. Gong, and J. Munday, "The generalized Shockley-Queisser limit for nanostructured solar cells". *Scientific Reports*, 5(1), 2015.
- [62] H. I. Ikeri, A. Onyia," Investigation Of Optical Characteristics Of Semiconductor Quantum Dots For Multi Junction Solar Cells Applications". *International Journal of Scientific and Technology Research*, 10(8):3532. 2019
- [63] P. Perez-Rodriguez et al, "Designing a hybrid thin-film/wafer silicon triple photovoltaic junction for solar water splitting". *Progress in Photovoltaics: Research and Applications*, 27(3), pp.245-254, 2018.
- [64] D. van Nijen, "Development of a c-Si/nc-Si:H/a-Si:H multi-junction device with a smooth c-Si surface texture," Delft University of MSc Thesis Report, 2020.
- [65] W. Cheng et al, "Monolithic Photoelectrochemical Device for Direct Water Splitting with 19% Efficiency". *ACS Energy Letters*, 3(8), pp.1795-1800, 2018.
- [66] S. Jaafar et al, "Natural dyes as TiO₂ sensitizers with membranes for photoelectrochemical water splitting: An overview". *Renewable and Sustainable Energy Reviews*, 78, pp.698-709, 2017.
- [67] C. Trompoukis et al, "Porous multi-junction thin-film silicon solar cells for scalable solar water splitting". *Solar Energy Materials and Solar Cells*, 182, pp.196-203, 2018.
- [68] T. Bosserez, "Minimization of Ionic Transport Resistance in Porous Monoliths for Application in Integrated Solar Water Splitting Devices". *The Journal of Physical Chemistry C*, 120(38), pp.21242-21247, 2016.
- [69] J. Jin et al, "An experimental and modeling/simulation-based evaluation of the efficiency and operational performance characteristics of an integrated, membrane-free, neutral pH solar-driven water-splitting system". *Energy Environ. Sci.*, 7(10), pp.3371-3380, 2014.
- [70] W. Vijeelaar et al, A Stand-Alone Si-Based Porous Photoelectrochemical Cell. *Advanced Energy Materials*, 9(19), p.1803548, 2019.
- [71] J. Yeom et al, "Maximum achievable aspect ratio in deep reactive ion etching of silicon due to aspect ratio dependent transport and the microloading effect". *Journal of Vacuum Science & Technology B: Microelectronics and Nanometer Structures*, 23(6), p.2319, 2015.
- [72] H. Jansen. "The black silicon method: a universal method for determining the parameter setting of a fluorine-based reactive ion etcher in deep silicon trench etching with profile control". *Journal of Micromechanics and Microengineering*, 5(2), pp.115-120, 1995.

- [73] P. Shankles et al, "Fabrication of nanoporous membranes for tuning microbial interactions and biochemical reactions". *Journal of Vacuum Science & Technology B, Nanotechnology and Microelectronics: Materials, Processing, Measurement, and Phenomena*, 33(6), 2015.
- [74] G. Daminelli et al, "Femtosecond laser interaction with silicon under water confinement. *Thin Solid Films*", 467(1-2), pp.334-341, 2004.
- [75] N. Bärsch, "Improving Laser Ablation of Zirconia by Liquid Films: Multiple Influence of Liquids on Surface Machining and Nanoparticle Generation". *Journal of Laser Micro/Nanoengineering*, 4(1), pp.66-70, 2009.
- [76] J. Kaakkunen et al, "Water-Assisted Femtosecond Laser Pulse Ablation of High Aspect Ratio Holes". *Physics Procedia*, 12, pp.89-93, 2011.
- [77] V. Manfrinato et al, "Resolution Limits of Electron-Beam Lithography toward the Atomic Scale". *Nano Letters*, 13(4), pp.1555-1558, 2013.
- [78] C. Vieu et al, "Resolution limits for electron-beam lithography". *Microelectronics Reliability*, 29(6), 2013.
- [79] D. Winston et al, "Scanning-helium-ion-beam lithography with hydrogen silsesquioxane resist". *Journal of Vacuum Science & Technology B: Microelectronics and Nanometer Structures*, 27(6), p.2702, 2009.
- [80] U. Tandon, "An overview of ion beam lithography for nanofabrication". *Vacuum*, 43(3), pp.241-251, 1992.
- [81] D. Reynaerts et al, "Microstructuring of silicon by electro-discharge machining (EDM) — part I: theory". *Sensors and Actuators A: Physical*, 60(1-3), pp.212-218, 1997.
- [82] F. Weng et al, "Fabrication of Micro Components to Silicon Wafer Using EDM Process". *Materials Science Forum*, 505-507, pp.217-222, 2006.
- [83] K. Furuya. "Nanometer-scale thickness control of amorphous silicon using isotropic wet-etching and low loss wire waveguide fabrication with the etched material". *Applied Physics Letters*, 100(25), 2012.
- [84] J. Albero et al, "Fabrication of spherical microlenses by a combination of isotropic wet etching of silicon and molding techniques". *Optics Express*, 17(8), 2009.
- [85] Xuan Ma, W., "Introduction To I-V Curves". 2020 [online] Cran.r-project.org. Available at: <https://cran.r-project.org/web/packages/ddiv/vignettes/IVcurve.html>
- [86] S. Matthias, S. and F. Müller, "Asymmetric pores in a silicon membrane acting as massively parallel brownian ratchets". *Nature*, 424(6944), pp.53-57, 2003.
- [87] Khan Academy. "Free Energy | Endergonic Vs Exergonic Reactions (Article)". | Khan Academy. 2020 [online] Available at: <https://www.khanacademy.org/science/biology/energy-and-enzymes/free-energy-tutorial/a/gibbs-free-energy>
- [88] Z. Chen, H. Dinh, and E. Miller, "Photoelectrochemical Water-Splitting". New York: Springer. 2020.

- [89] Chemed.chem.purdue.edu. "Gibbs Free Energy". 2020 [online] Available at: <https://chemed.chem.purdue.edu/genchem/topicreview/bp/ch21/gibbs.php>
- [90] H. Danneel and E. Merriam, "Electrochemistry". [Charlston, SC]: BiblioLife. 2010.
- [91] L. Wei and G. Xuefei. "Chapter 10 Recent Advances in Electrocatalytic Water Splitting". NanoScience: Nanomaterial Nanotechnology Applications. Publisher: Engineered Science Publisher, USA, 2019.
- [92] K. Scott, K., "2-Electrochemical principles and characterization of bioelectrochemical systems". Microbial Electrochemical and Fuel Cells Fundamentals and Applications, pp.29-60, 2016.
- [93] J. E. Dickinson, and G. Hinds, "The Butler-Volmer Equation for Polymer Electrolyte Membrane Fuel Cell (PEMFC) Electrode Kinetics: A Critical Discussion". Journal of The Electrochemical Society, 166(4), 2019.
- [94] C. van de Goor, "Electrocatalytic Behavior of Platinum Prepared in the Surfactant Medium for Hydrogen Evolution Reaction (HER)". ECS Meeting Abstracts (2011).
- [95] D. Bessarabov, and P. Millet, "Fundamentals of Water Electrolysis". PEM Water Electrolysis, 43-73, 2018.
- [96] Doc.comsol.com. 2020. [online] Available at: <https://doc.comsol.com/5.4/doc/com.comsol.help.echem/ElectrochemistryModuleUsersGuide.pdf>
- [97] R. Bosco et al, "Surface Engineering for Bone Implants: A Trend from Passive to Active Surfaces". Coatings, 2(3), pp.95-119, 2012.
- [98] K. Teo, "The influence of the push-pull effect and a π -conjugated system in conversion efficiency of bis-chalcone compounds in a dye sensitized solar cell". Journal of Molecular Structure, 1143, pp.42-48, 2017.
- [99] Terpconnect.umd.edu. 2020. Microengineering -- Lithography. [online] Available at: https://terpconnect.umd.edu/~sandborn/research/JPL_MEMS/microeng_lithogr.html
- [100] Ezajeba.changeip.com. 2020. Bosch Process Drie Recipe. [online] Available at: <http://ezajeba.changeip.com/Bosch-process-drie-recipe.html>
- [101] H. Gatzert et al, "Micro and nano fabrication: Tools and processes". Heidelberg, Germany: Springer, 2015.
- [102] TU Delft. 2020. Delft Sirius Laser Facility. [online] Available at: <https://www.tudelft.nl/lr/organisatie/afdelingen/aerospace-structures-and-materials/structural-integrity-and-composites/facilities/delft-sirius-laser-facility/>
- [103] Lindroos, V., 2010. Handbook Of Silicon Based MEMS Materials And Technologies. Amsterdam: William Andrew/Elsevier.

[104] T. Xu et al, "Effects of deep reactive ion etching parameters on etching rate and surface morphology in extremely deep silicon etch process with high aspect ratio". *Advances in Mechanical Engineering*, 9(12), 2017.

Appendix A: Processing Parameters

Table A 1: PECVD Parameters for SHJ Processing (from bottom to top side)

	Layer	Thickness (nm)	SiH ₄ (sccm)	H ₂ (sccm)	CO ₂ (sccm)	B ₂ H ₆ /H ₂ (sccm)	PH ₃ (sccm)	Pressure (mbar)	Power (W)
n-side	n-a-Si:H	10	40	0	0	0	11	0.6	9
	i-a-Si:H	10	40	0	0	0	0	0.7	2.8
n-type c-Si wafer									
p-side	i-a-Si:H	10	40	0	0	0	0	0.7	2.8
	i-nc-Si:H	-	1.2	120	0	0	0	4	13
	p-nc-SiOx:H	4	0.8	170	1.4	10	0	2.2	11
	p-nc-Si:H	15	0.8	170	0	10	0	2.2	13

An 80 second Hydrogen Plasma Treatment (HPT) is done at 200 sccm H₂ flow at a pressure of 2.2 mbar and power of 9 W after depositing the i-a-Si:H layers to passivate dangling bonds.

Table A 2: Magnetron sputtering parameters for ITO Processing

Layer	Thickness (nm)	Ar (sccm)	Substrate Temp (°C)	Heater Temp (°C)	Pre-Sputter Time (sec)	Processing Time (sec)	Pressure (mbar)	Power (W)
ITO Front Side	75	50	110	206	300	1513	0.02	145
ITO Back Side	150	50	110	206	300	3026	0.02	145

Table A 3: Deep Reactive Ion Etching (DRIE) Parameters

Parameters		During Etching		During Passivation	
ICP Source Power [W]	600	Etching Pressure [mTorr]	30	Passivation Pressure [mTorr]	19
Chamber Temperature [°C]	40	SF6 Flow [sccm]	130	SF6 Flow [sccm]	0
Chuck Temperature [°C]	25	O2 Flow [sccm]	13	O2 Flow [sccm]	0
Bias Power [W]	15	C4F8 Flow [sccm]	0	C4F8 Flow [sccm]	85
Number of cycles	500	Etching Period [sec]	8	Passivation Period [sec]	5

Appendix B: pH Gradient Simulations (with vs without PEM)

The Proton Exchange Membranes (PEM) were modelled as boundaries at the pore sidewalls. The membrane potential was set to be equal to the electrolyte potential, and the proton concentration was set to the initial concentration input in the model (0.124 M), based on a 0.1 M H₂SO₄ electrolyte solution. The pH gradient is reduced by 80% when a PEM is included and there is no pH gradient inside the pores.

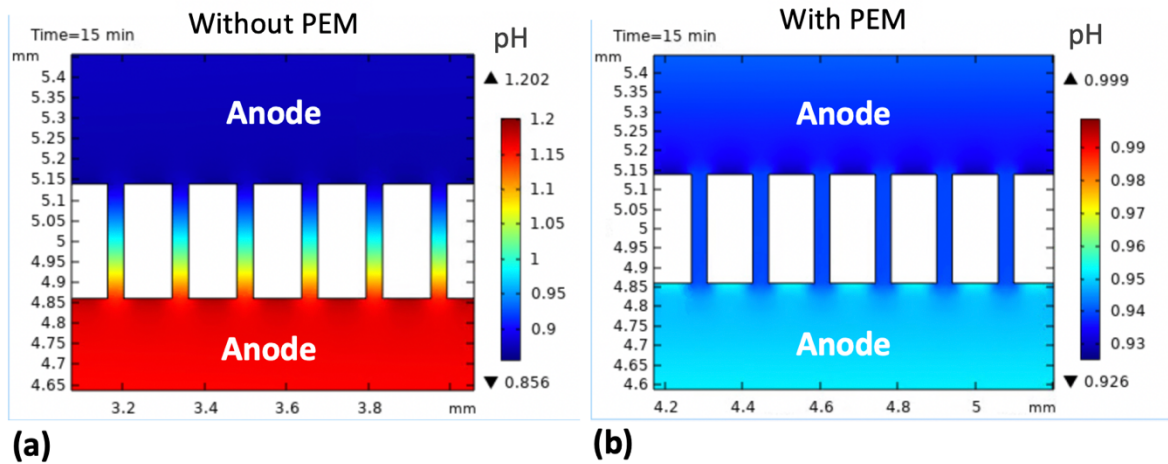


Figure B 1: pH gradient COMSOL simulation results for $D_p/P_p = 40\mu\text{m}/158\mu\text{m}$: (a) Without a PEM; (b) with PEM. The pH gradient is reduced by 80% when a Proton Exchange Membranes (PEM's) are included inside the pores . Also, there is no pH gradient inside the pores with PEM.

Appendix C: J-V and EQE Plots of Silicon Hetero-Junctions

The averaged J-V and EQE plots of the Silicon Hetero-Junctions used in this study are shown in Figure C1. The J-V and EQE plots for each pattern was averaged based on measurements of 6 cells. Considering that less porous patterns should result in more back contact coverage and thus, fewer resistive losses, it would be expected that the SHJ with the lowest coverage would yield the lowest performance. However, the results from the J-V and EQE plots do not appear to correlate with the patterning. The pattern having the least contact coverage ($D_p/P_p = 80\mu\text{m}/187\mu\text{m}$) actually yields an average J-V performance, whereas the pattern with the highest back contact coverage ($D_p/P_p = 20\mu\text{m}/80\mu\text{m}$), actually has the lowest J-V performance. Moreover, the difference in performance falls within the tolerance range for each batch of samples.

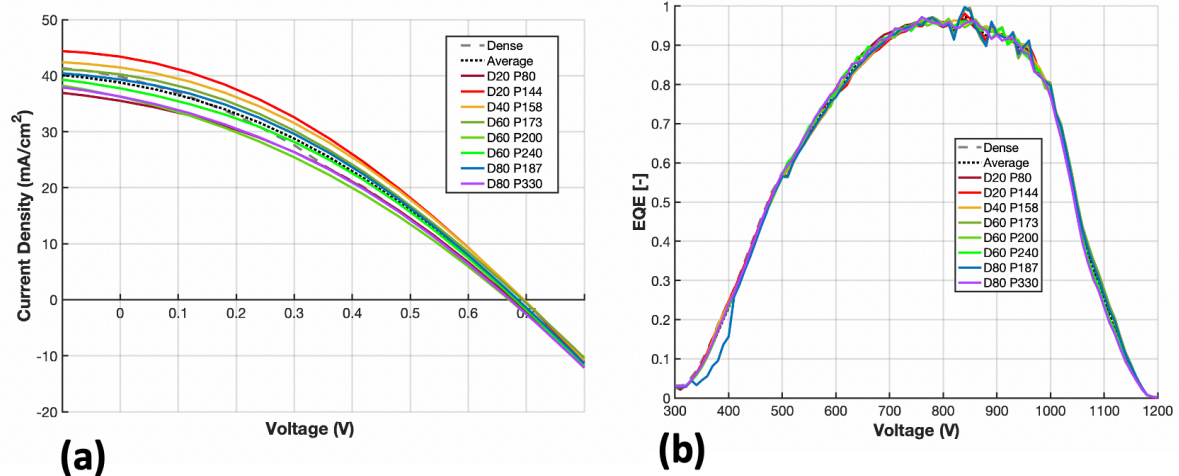


Figure C 1: J-V and EQE plots for all SHJ's that were meant to constitute the experimental dataset. The SHJ's were processed with ITO, an Al front grid, and a Pt back contact, which is patterned according to the corresponding pore size and distribution. The SHJ's do not include pores or microdots.

